

MASTER

Rainfall interception by buildings for urban hydrology modeling

van der Linden, W.

Award date:
2010

[Link to publication](#)

Disclaimer

This document contains a student thesis (bachelor's or master's), as authored by a student at Eindhoven University of Technology. Student theses are made available in the TU/e repository upon obtaining the required degree. The grade received is not published on the document as presented in the repository. The required complexity or quality of research of student theses may vary by program, and the required minimum study period may vary in duration.

General rights

Copyright and moral rights for the publications made accessible in the public portal are retained by the authors and/or other copyright owners and it is a condition of accessing publications that users recognise and abide by the legal requirements associated with these rights.

- Users may download and print one copy of any publication from the public portal for the purpose of private study or research.
- You may not further distribute the material or use it for any profit-making activity or commercial gain

ARR
2010
BWK

4551



Technische Universiteit
Eindhoven
University of Technology

Department of Architecture Building and Planning /
Unit Building Physics and Systems

Rainfall interception by buildings for urban hydrology modeling

Willemijne van der Linden



Rainfall interception by buildings for urban hydrology modeling

Willemijne van der Linden

June 2010

Committee:

Dr. Ir. Bert Blocken (chairman)

Ing. Jan Diepens

Prof. Dr. Ir. Martin de Wit

Eindhoven University of Technology

Dr. Ir.-Arch. Roel Hendrickx

Prof. Dr. Ir.-Arch. Staf Roels

Catholic University of Leuven, Flanders, Belgium

TU/e Technische Universiteit
Eindhoven
University of Technology

Department of Architecture Building and Planning/Unit Building Physics and Systems

Abstract

One of the results of climate change is an increased amount of precipitation and a rise in rainfall intensity. This can lead to an overload on the sewer system or to the ground water level if no sewer system is present, and even to flooding.

During rain events part of the rainwater can be intercepted by building surfaces (rainfall interception). This amount of water is temporarily stored on these surfaces and eventually evaporates into the atmosphere. Since this intercepted water does not reach the ground, it also does not contribute to the load on the sewer system. Especially porous materials on building roofs but also in facades can intercept large quantities of water. Rainfall interception by buildings therefore becomes more and more important in hydrological modeling, particularly in urban areas.

In this research rainfall interception by building facades is studied. In order to do this measurements as well as simulations are performed. Full-scale measurements are executed on a test facade at Eindhoven University of Technology, the Netherlands. The moisture response (mass change) to wind-driven rain of four material samples is registered. Furthermore micro-meteorological data are gathered. The difference in rainfall interception by two porous building materials is demonstrated. For the brick with high porosity the rainfall interception yields 100%, while the low porous brick accommodates for a minimum of 76.6% during the measurement period. Due to local saturation at the exterior boundary runoff occurred for the latter type of brick. Besides the full-scale experiments an extensive set of laboratory measurements is performed. Various moisture-related material properties are determined for the two porous building materials.

For the numerical part of this study the finite element code HAMFEM is used. To gain insight into the moisture response of porous building materials to wind-driven rain, one-dimensional heat and moisture transfer simulations are performed using differential balance equations for mass and energy. The micro-meteorological data gathered at the test facade are used as atmospheric boundary conditions and the results of the laboratory experiments are used to specify the material properties. The simulation results give the mass change of the materials in time and this is compared to the mass change obtained from the full-scale measurements to verify the correct implementation of the model and the capability to reproduce the measurement results. It is shown that for the brick with high porosity the model accurately predicts the rainfall interception during one rain event. Rainfall interception for another rain event is described less precisely however. For the other type of brick the model fails to predict runoff because in the simulations the exterior boundary does not reach the capillary moisture content, while in reality local saturation does occur because the wind-driven rain intensity on the facade exceeds the absorption rate of the brick. The largest deviations between experimental and numerical results are found in the evaporation process, where the model overestimates the mass decrease due to evaporation. This is to a large extent due to the uncertainty of the heat and moisture transfer coefficients.

As a next step meteorological data of several climate groups according to the Köppen climate classification are used to specify the boundary conditions. With this

the influence of different climates on rainfall interception is studied. It is shown that for four of the six climate groups used for the analysis no runoff occurred for the brick with high porosity for the period considered. This means that this type of brick accommodates for 100% rainfall interception in these climates. For the remaining two climate groups the brick with high porosity yields a minimum RI of only 1.9% and 6% in periods of severe rain, increasing to 100% for moderate rain events. Comparison of the rainfall interception by the two bricks results in a rainfall interception of at least 40% by the brick with low porosity based on the rainfall interception by the other type of brick. It is demonstrated however that the model not always succeeds in accurately predicting the runoff. Therefore no hard conclusions can be drawn on the performance regarding rainfall interception by the two porous building materials in other climates.

Acknowledgements

The topic of rainfall interception really appealed to me. It was very interesting working on this graduation project, however, it was very challenging as well. First of all I want to thank the members of my committee and especially Bert Blocken, for their guidance along the way.

The experimental part of this research could not have been realized without the help of the staff of the laboratory of Building Physics. I want to thank Geertjan Maas in particular for all his help and effort. The assistance of the people in Leuven is very much appreciated as well, in which my special thanks goes to Roel Hendrickx, who is also a member of my committee. I am also grateful to Wienerberger and Saint Gobain for the disposal of material samples for this study.

Furthermore I am grateful to Daniel Costola, who introduced me to HAMFEM and helped me get to know this program. Hans Janssen is thanked for his clarifications on HAMFEM as well. The numerical part of this study on climate dependent parameters was made possible by the Australian National Climate Center, Bureau of Meteorology which is gratefully acknowledged.

And last but certainly not least I want to thank my fellow students and my friends and family for their support and understanding. And of course Peter, who is always there for me and never stopped believing in me. I could not have done this without you.

Contents

Nomenclature	xi
1 Introduction	1
1.1 Background	1
1.2 Preceding work	2
1.3 Objectives	2
1.4 Methodology	3
2 Measurements	4
2.1 Theory	4
2.2 Full-scale measurements	6
2.2.1 Site description	6
2.2.2 Measurement setup	7
2.2.3 Parameters	10
2.2.4 Data processing	17
2.2.5 Results	17
2.3 Laboratory experiments	23
2.3.1 Determination of the water absorption coefficient and capillary moisture content	24
2.3.2 Determination of the open porosity, density and vacuum saturation content	29
2.3.3 Determination of the moisture retention curve	33
2.3.4 Determination of the liquid water diffusivity and liquid permeability	42
2.3.5 Determination of the water storage on three types of glass	49
2.4 Conclusion	51
3 Numerical simulations	53
3.1 Model	53
3.1.1 Physical background	53
3.1.2 Numerical implementation	54
3.2 Model validation	59
3.2.1 Test case	59
3.2.2 Comparison experimental and numerical results	60
3.3 Climate parameter analysis	68
3.3.1 Köppen climate classification	68
3.3.2 Numerical results	69
3.4 Conclusion	72
4 Conclusions and recommendations	73

Appendix A	Specifications brick	75
Appendix B	Specifications glue.....	77
Appendix C	Specifications used equipment	79
Appendix D	Results water absorption experiment.....	81
Appendix E	Simulation settings.....	87
Appendix F	Simulation results climate groups	89
References		92

Nomenclature

Letters

A	area	m^2
A_w	water absorption coefficient	$kg/m^2s^{1/2}$
C	moisture capacity	$kg/m^3 Pa$
c	specific heat capacity	$J/kg K$
c_i	model parameter	-
D	diffusivity	m^2/s
d	thickness	m
F	view factor	-
g	moisture flow	$kg/m^2 s$
h	heat transfer coefficient	$W/m^2 K$
I	X-ray intensity	keV
K	liquid permeability	s
L_v	enthalpy of evaporation	J/kg
l_i	weight factor	$0 < l_i \leq 1, \sum l_i = 1$
m	mass	kg
n_i	model parameter	-
p	pressure	Pa
q	heat flux	W/m^2
R	rainfall intensity	mm/h
RH	relative humidity	$\%$
RI	rainfall interception	kg/m^3
S	storage	kg/m^2
	radiative heat exchange	W/m^2
S_n	number of subsystems	-
T	temperature	K
t	time	s
V	volume	m^3
V_{loc}	local wind speed	m/s
w	moisture content	kg/m^3
x	distance	m

Greek letters

β	moisture transfer coefficient	s/m
Δ	difference	-
ϵ	long-wave emissivity	-
η	catch ratio	-
θ	contact angle	$^\circ$
κ	solar absorption coefficient	-
λ	Boltzmann variable	$m/s^{1/2}$
μ	attenuation coefficient	$1/m$

ρ	density	kg/m ³
σ	surface tension	N/m
	Stefan-Boltzmann constant	W/m ² K ⁴
ψ_o	open porosity	-

Subscripts

0	incident solid
a	air
c	capillary
	convective
cap	capillary
$cond$	conduction
$conv$	convection
e	exterior
eq	equilibrium
g	gas
	ground
h	horizontal
i	initial interior
l	liquid
mat	matrix
s	surface
sat	saturation
t	time
v	vapor
w	water
WDR	wind-driven rain

Acronyms

BHP	Brick High Porosity
BLP	Brick Low Porosity
HAM	Heat Air Moisture
HAMFEM	Heat Air Moisture Finite Element Method
RI	Rainfall interception
WDR	Wind-driven rain

Chapter 1

Introduction

In this chapter an introduction to rainfall interception by buildings is presented. Some background information is given and the preceding work performed on this topic is discussed. Furthermore the objectives of this study are described and the research method is outlined.

1.1 Background

The climate on earth is changing. One of the results of this climate change is an increased amount of precipitation. This means not only more precipitation, but a rise in heavy rain events as well (IPCC, 2007).

During rainfall, part of the water can be intercepted by buildings and trees. This intercepted water (rainfall interception) is temporarily stored and eventually evaporates back into the atmosphere. This amount of water does not reach the ground and therefore does not contribute to the load on the sewer system or the ground water level if no sewer system is present.

Certain amount of research has already been done on rainfall interception by trees. However, rainfall interception by buildings has received less attention, while it is expected that building surfaces can intercept a significant amount of water. Particularly buildings made of porous building materials are expected to procure significant quantities of rainfall interception. Four contributions of porous building materials to rainfall interception can be distinguished:

- Rainfall interception by building roofs
- Rainfall interception by building facades
- Rainfall runoff from building roofs
- Rainfall runoff from building facades

Rainfall runoff from building roofs is expected to have the largest potential since these building surfaces receive the largest amount of rain. This amount of rain can

be collected before reaching the ground, which is done in a recent project in the Netherlands (waterkaderhaaglanden.nl), and therefore does not contribute to the load on the sewer system. The amount of rainfall interception by building roofs strongly depends on the finishing layer of the roof tiles, since many types of tiles are glazed and therefore less capable of absorbing water. Rainfall interception by building facades is dependent on the amount of wind-driven rain. It is expected though that a large percentage of this wind-driven rain can be intercepted by porous building facades and therefore this is investigated in this research.

The use of porous building materials can play an important role in relieving the sewer system and the prevention of flooding. Especially in urban areas, rainfall interception can become an important design parameter.

1.2 Preceding work

Over the past decade several studies regarding rainfall interception by buildings were published. In Ragab et al. (2003) the effect of slope and aspect on water runoff from roofs in a residential area was experimentally quantified. In a study of Nakayoshi et al. (2009) an urban scale model was made to perform research on rainfall interception in an urban area. Van Mook (2002) studied wind-driven rain (WDR) on building facades and in Blocken et al. (2002) WDR research on a low-rise building is presented. In 2004 Blocken et al. presented a review on WDR research. A study of Briggen et al. (2009) included WDR research as well to investigate the cause of moisture problems on the facades of a monumental tower. In Blocken et al. (2009) an overview of research on water runoff from building facades is given.

Besides this more detailed research on different aspects of rainfall interception was performed. In Blocken et al. (2006) an elaborate study on the errors associated with WDR gauges is presented.

Furthermore studies regarding numerical modeling of rainfall interception and the involved processes were carried out. An approach which combines Computational Fluid Dynamics with Heat Air and Moisture for modeling WDR on building facades was presented by Blocken et al. (2007), in which a five-step simulation methodology is proposed. In Janssen et al. (2007a) an elaborate explanation of the finite element code HAMFEM and the associated boundary conditions for WDR modeling are given. In Abaku et al. (2009) some errors related to HAM modeling of the moisture response of building facades are discussed.

1.3 Objectives

The recent generation of urban hydrological models often does not take into account rainfall interception by buildings, while it can be of great importance. Especially porous building surfaces are expected to intercept large quantities of rainwater. The aim of this research is to gain quantitative knowledge on rainfall interception by buildings and study the influence of climate on rainfall interception. In order to achieve this objective, several sub-objectives are defined:

- Gather full-scale measurement data regarding rainfall interception.
- Gain insight into the difference in rainfall interception by porous and non-porous building materials.
- Gain insight into the hygrothermal processes in porous building materials.
- Relate the amount of wind-driven rain to the moisture response of the building facade.
- Use a finite element code for HAM modeling to numerically predict rainfall interception by buildings.
- Validate the numerical model by means of full-scale measurement data.

1.4 Methodology

This study consists of experimental and numerical research. In the experimental part both full-scale and laboratory experiments are considered. For the full-scale experiments measurements on a test facade are executed. The moisture response of different building materials to rainfall is determined in terms of mass change and therefore the amount of rainfall interception by these materials is obtained. Furthermore parameters such as wind speed, wind direction, temperature, relative humidity and solar radiation are registered. Besides this a set of laboratory experiments is performed in which several material properties are determined.

The numerical part consists of two types of simulation. First the numerical model is validated by means of the experimental results. The parameters obtained from the laboratory experiments combined with the micro-meteorological data gathered at the test facade are used as input and boundary conditions for the model. The results of the simulation are then compared to the values obtained from the full-scale experiments. Once the model is validated the second type of simulations is carried out. Some adaptations are made with which meteorological data from several climate groups are used as boundary condition. With this the influence of different climates on rainfall interception is studied.

Chapter 2

Measurements

This chapter presents the experimental part of this study. Until now several studies on rainfall interception by buildings have been reported. However, complete sets of full-scale measurement data are lacking. For this research full-scale measurements are executed in order to collect measurement data regarding rainfall interception by buildings. The results of the full-scale measurements are used for the validation of the numerical model. Furthermore an extensive set of laboratory experiments is performed. In these experiments several moisture-related material properties are obtained. These material properties are used as input for the simulations.

2.1 Theory

This paragraph presents an overview of important terms and principles regarding the experimental part of this study. The theory is used in the following paragraphs.

Horizontal rainfall intensity

Horizontal rainfall intensity is defined as the amount of rainfall falling through a horizontal plane in the free field (Blocken et al., 2007).

Wind-driven rain (WDR)

Wind-driven rain (WDR) is rain that has not only a vertical but also a horizontal velocity component due to wind (Van Mook, 2002, Abuku et al., 2009). The rain is carried by wind and driven onto the building facade. WDR is one of the most important moisture sources on building facades (Blocken et al., 2006, Blocken et al., 2007, Janssen et al., 2007a,b, Abuku et al., 2009).

Rainfall interception

Rainfall interception is *the amount of rain that is captured by and temporarily stored on obstacles on earth and that eventually evaporates into the atmosphere.*

2. Experimental research

In the context of this study, which is focused on buildings, rainfall interception is defined as *the amount of rain that is captured by and temporarily stored on building surfaces and that eventually evaporates into the atmosphere.*

Figure 2.1 presents a flowchart of precipitation in the building environment.

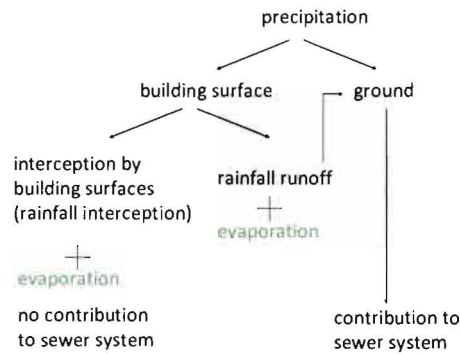


Figure 2.1: Flowchart of precipitation in the building environment.

As shown in figure 2.1, evaporation can occur in different ways. Firstly evaporation of intercepted water; during rainfall part of the intercepted water can immediately evaporate. Besides this, intercepted water can evaporate after the rain event. Evaporation during the rain event is expected to be very low because of the high relative humidity of the surrounding air. Secondly evaporation can take place during rainfall runoff.

As the figure illustrates as well, the amount of intercepted water does not reach the ground and therefore does not contribute to the load on the sewer system or to the groundwater level if no sewer system is present.

In figure 2.2 the different mass flows from and to the building surface are schematically depicted.

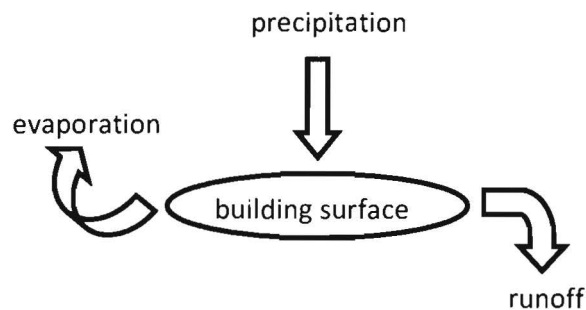


Figure 2.2: Mass flows from and to the building surface.

Tipping-bucket mechanism

In this study the tipping-bucket mechanism is used to measure the amount of precipitation. A tipping-bucket mechanism consists of two buckets. The main principle is that rain is collected in one of the two buckets. When the bucket is full it

2. Experimental research

becomes overbalanced and tilts over. This way the full bucket is emptied and the other bucket is put into position to collect the next amount of rainfall. Every time a bucket is full a pulse is released. The pulses are registered with a data logger. Each pulse represents a certain amount of water and therefore the amount of precipitation is determined. Figure 2.3 schematically depicts this principle.

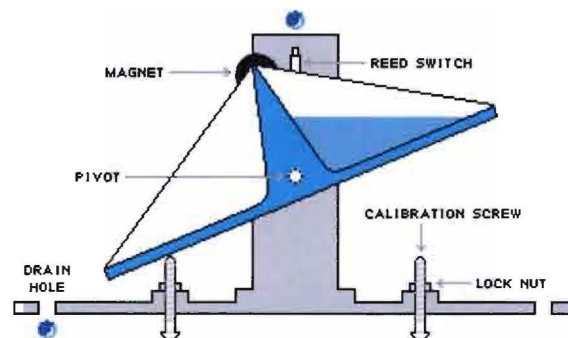


Figure 2.3: Schematic representation of a tipping-bucket mechanism (Weathershack.com).

2.2 Full-scale measurements

In this paragraph the full-scale measurements are discussed. For different material samples the rainfall interception in time is determined. Besides this, environmental parameters are measured in order to collect meteorological data.

2.2.1 Site description

For the full-scale measurements the test facade and the roof of the Vertigo building on the campus of the Eindhoven University of Technology are used. Furthermore the roof of the Auditorium is used to collect horizontal rainfall data. Figure 2.4 presents the location of the two buildings. Figure 2.5 shows the two buildings.

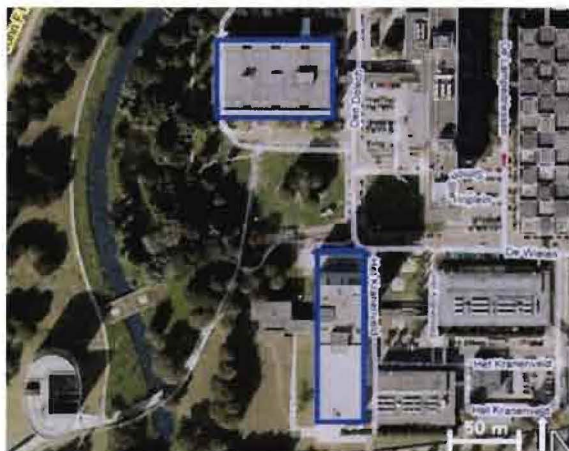


Figure 2.4: Aerial photograph with the location of the Auditorium (above) and Vertigo (below) highlighted in blue (Google maps).

2. Experimental research



Figure 2.5: Photograph of (a) the Auditorium and (b) the Vertigo building (Tue.nl).

2.2.2 Measurement setup

The test facade of Vertigo is used for the full-scale experiments. Figure 2.6 and 2.7 present the whole facade of the building and figure 2.8 and 2.9 show the test facade.

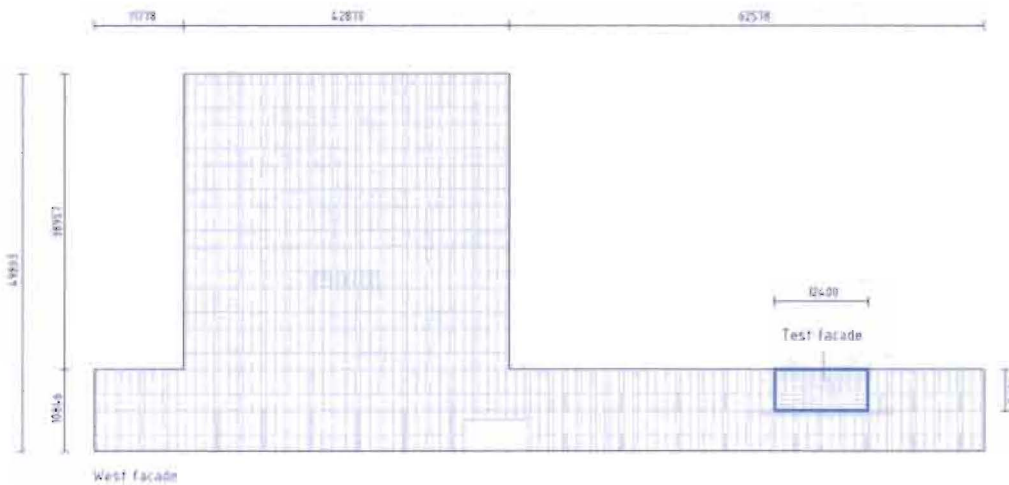


Figure 2.6: West facade of Vertigo with the test facade indicated in blue. Dimensions are in mm.



Figure 2.7: Photograph of the west facade of Vertigo.

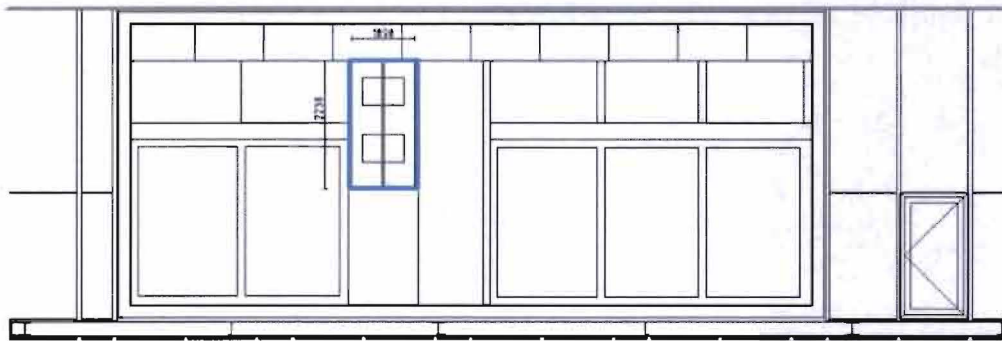


Figure 2.8: Test facade of Vertigo. The part highlighted in blue is used for this study. Dimensions are in mm.



Figure 2.9: Photograph of the test facade of Vertigo.

The test facade is positioned at the lower west facade of the building. On the test facade the mass change of four material samples is monitored. From this the rainfall interception by the material samples is determined. Furthermore micro-meteorological data are collected.

Materials

The part of the test facade that is used for this study is indicated in blue in figure 2.8. Within this part four removable samples, with dimensions of 0.34 x 0.49 m, are positioned, as indicated in figure 2.10. The samples consist of the following materials:

- A Material with water-repellent characteristics (Teflon)
- B Normal glass (Float glass)
- C Brick with low porosity (RBB®)
- D Brick with high porosity (Dommelrood®)

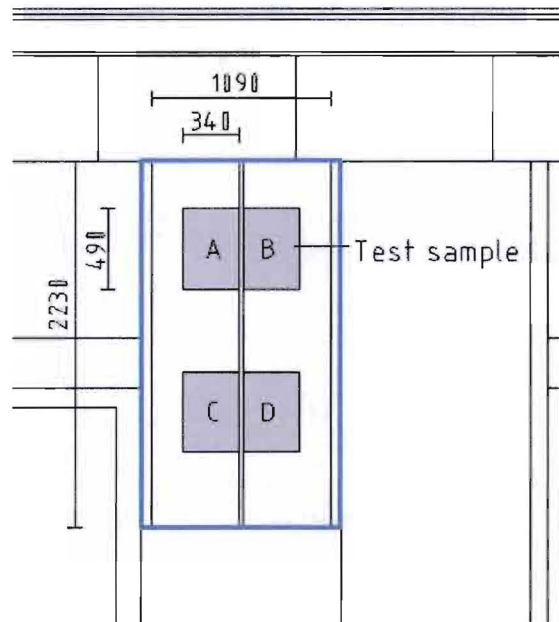


Figure 2.10: The part of the test facade used for this study, with four removable test samples (A-D). Dimensions are in mm.

The Teflon can be representative for actual building materials, for example glass with water-repellent characteristics. The reason that glass is included in this study is to gain insight into the rainfall interception potential of non-porous building materials. The main characteristics of the two types of brick are presented in table 2.1. The determination method of the density and open porosity is explained in section 2.3.2. Further specifications provided by the manufacturer are found in Appendix A.

Table 2.1: Main characteristics of the two types of brick.

	Brick with high porosity	Brick with low porosity
Dimensions [mm]	209 x 100 x 50	210 x 100 x 50
Density [kg/m ³]	1866	2057
Open porosity [-]	0.30	0.21

The bricks are glued together to eliminate the influence of the joints as much as possible and obtain one-dimensional moisture transport. Besides this the sides of the brick test samples are sealed as well. The effective brick area of the samples is 0.30 x 0.45 m. Specifications of the glue are included in Appendix B.

Method

The removable parts of the test facade are referred to as ‘test samples’. The test samples are part of a weighing setup. In figure 2.11 a three-dimensional drawing of the weighing setup is presented. Figure 2.12 depicts a schematic overview of the setup.

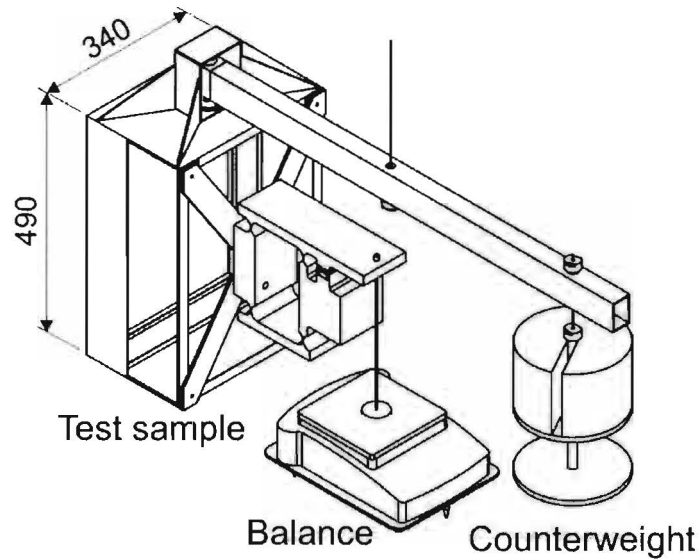


Figure 2.11: Three-dimensional drawing of the weighing setup. Dimensions are in mm.

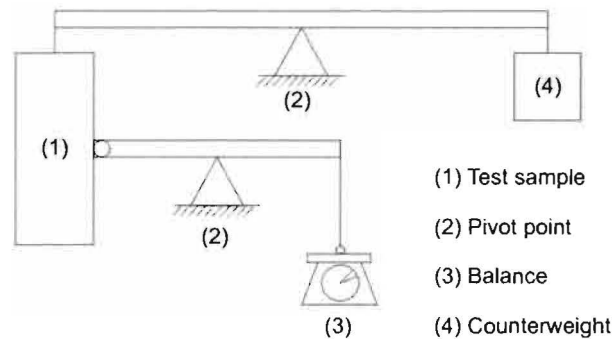


Figure 2.12: Schematic overview the weighing setup.

The main working principle of this setup is as follows.

The test sample is fixed to the one end of a lever mechanism. On the other end a counterweight is attached. The test sample is connected to a balance through another lever mechanism that only allows for vertical displacement. Because of the lever mechanism a mass increase of the test samples leads to a mass decrease measured by the balance.

2.2.3 Parameters

Several parameters regarding rainfall interception are determined for this study. Parameters such as rainfall intensity, wind speed and wind direction are obtained to collect micro-meteorological data which are used for the simulations. Furthermore the rainfall interception is measured and used for the validation study of the numerical model.

Micro-meteorological parameters

Horizontal rainfall intensity

As a first parameter the horizontal rainfall intensity is determined. For this purpose horizontal rain gauges are installed. Two rain gauges are positioned on the roof of Vertigo and one on the roof of the Auditorium. Figure 2.13 and 2.14 show the measurement positions.

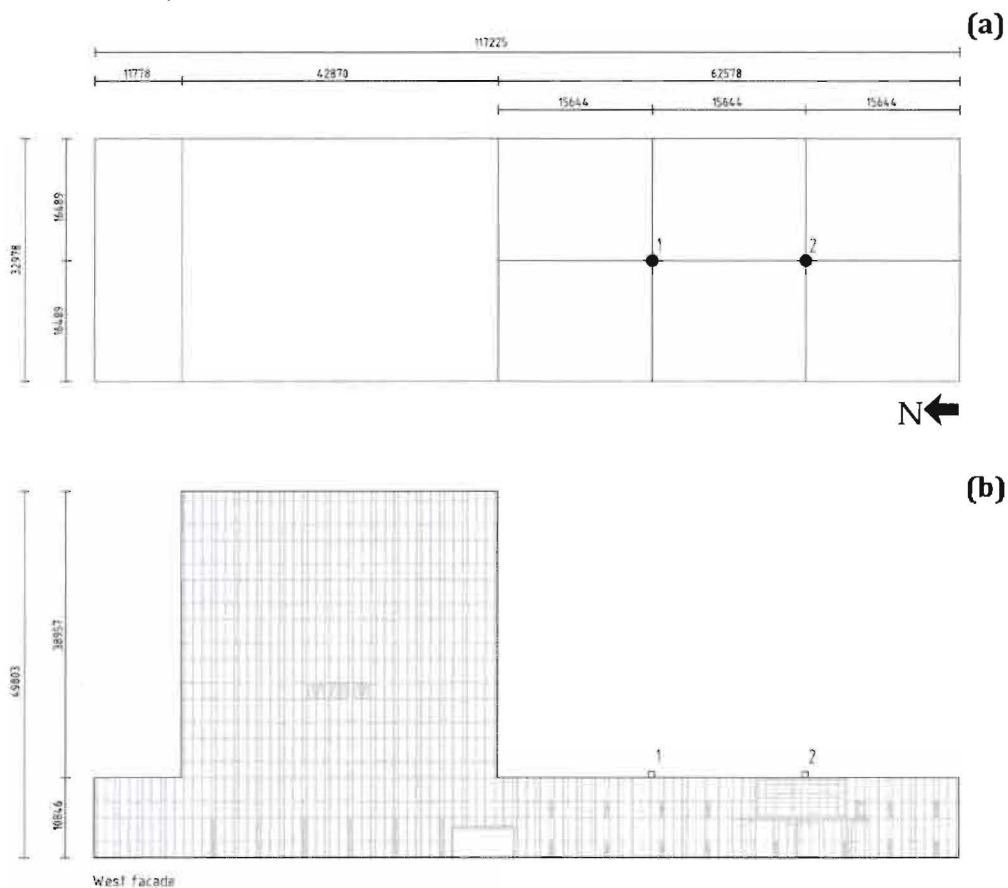


Figure 2.13: Measurement positions of the horizontal rain gauges indicated with number 1 and 2 on (a) the roof and (b) the facade of Vertigo. Dimensions are in mm.

On Vertigo the rain gauges are kept clear from the edges in order to reduce the influence of the edges. It is possible however that the high-rise part of Vertigo influences the wind pattern around the rain gauges. On the Auditorium the rain gauge is placed 6 meters clear from the mast to prevent the mast from being an obstruction for the gauge. Furthermore the top of the collection area of the gauges is kept as low as possible to reduce wind errors (Blocken et al., 2006).

2. Experimental research

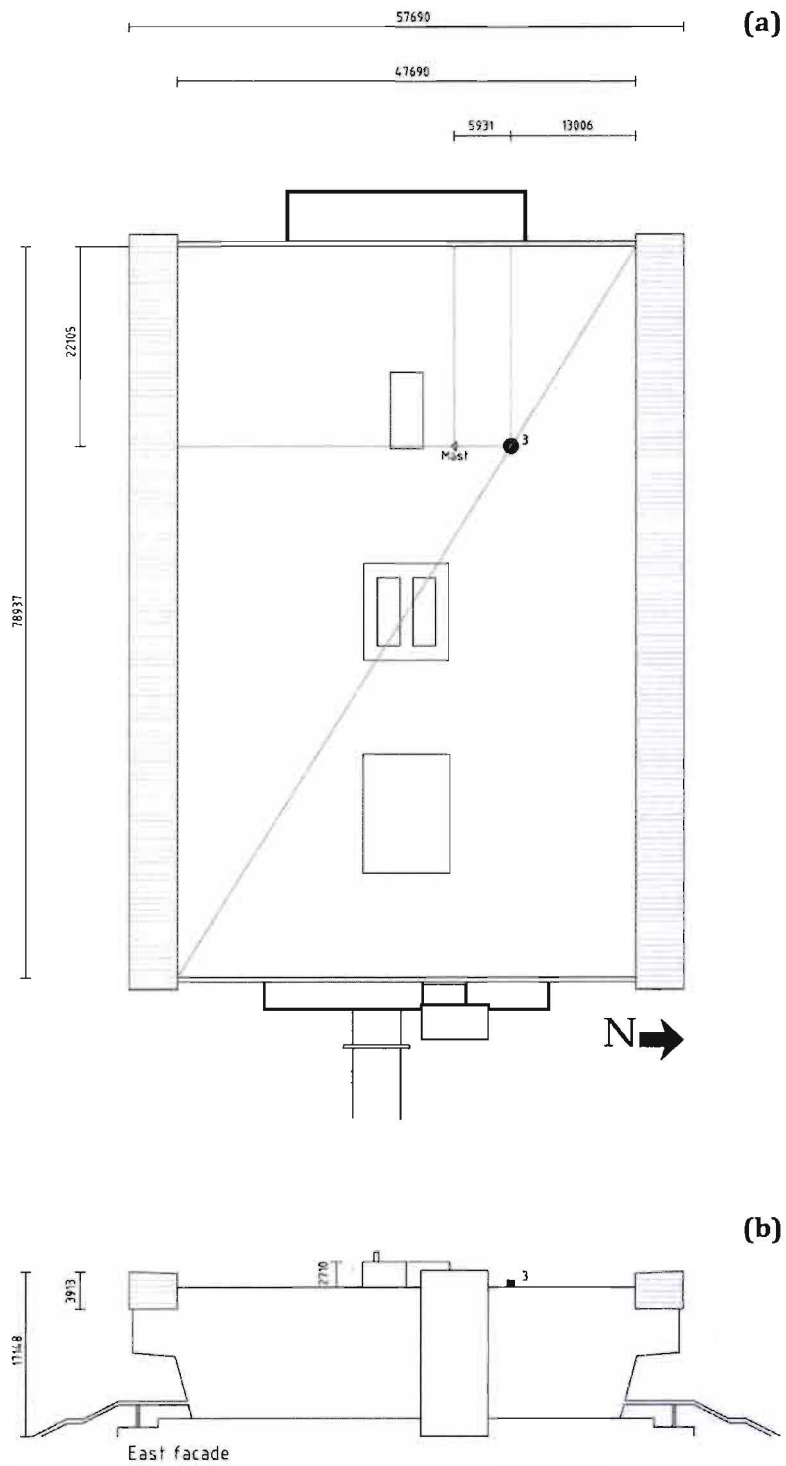


Figure 2.14: Measurement position of the horizontal rain gauge indicated with number 3 on (a) the roof and (b) the facade of the Auditorium. Dimensions are in mm.

2. Experimental research

Other micro-meteorological parameters

Besides the horizontal rainfall intensity another set of environmental parameters is determined. The wind speed and wind direction are measured by means of an anemometer. Besides this, a pyranometer is placed to determine the solar radiation. Figure 2.15a shows the measurement positions of the latter two parameters. Initially the anemometer was placed at position 2a. It was assumed however that the wind pattern could be disturbed by the runoff reservoirs, which are discussed later on in this paragraph and therefore the anemometer was repositioned to position 2b. The anemometer is kept clear three centimeters from the facade, since the wind speed at the surface is equal to zero. This is shown in figure 2.15b. Furthermore the air temperature and relative humidity are measured.

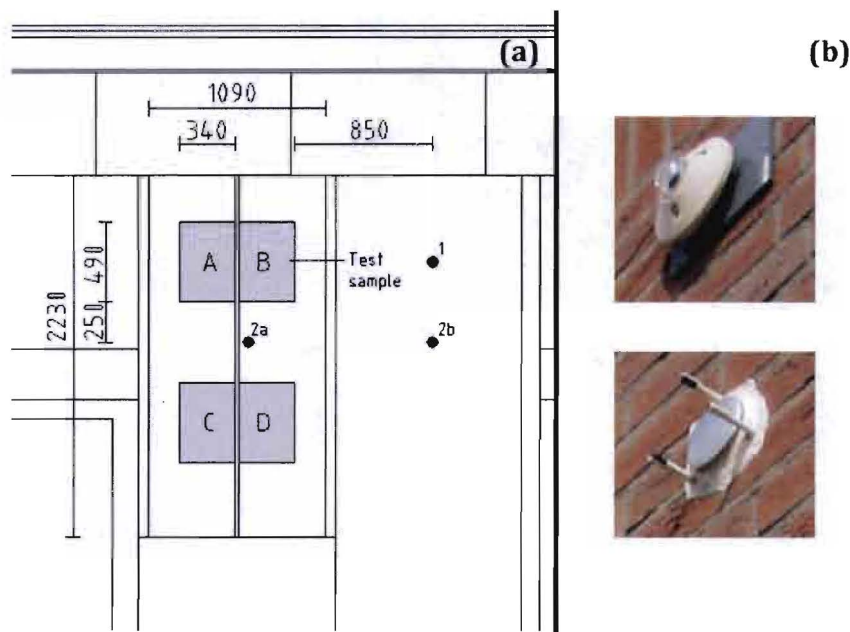


Figure 2.15: Test facade with (a) the measurement position of the pyranometer and anemometer indicated with number 1 and 2a and 2b respectively and (b) photograph of the pyranometer (above) and anemometer (below) in position. Dimensions are in mm.

Rainfall interception

From the mass change measured by means of the weighing setup, the amount of rainfall interception (RI) by the different materials is determined. Note that the immediate evaporation during rainfall is not included here and the amount of RI may be slightly underestimated. To understand what percentage of the rain falling onto the facade is actually intercepted, two other parameters regarding rain are determined: wind-driven rain and rainfall runoff.

Wind-driven rain (WDR)

WDR is the amount of water falling onto the facade. WDR is measured by means of wind-driven rain gauges. Not all rain falling onto the facade is measured by the gauge however, due to splashing and bouncing of droplets off the facade (Abuku et al., 2009). The selected type of WDR gauge was designed and manufactured by P.

2. Experimental research

Briggen and the laboratory of Building Physics and Systems of the Eindhoven University of Technology. Figure 2.16 presents this rain gauge.

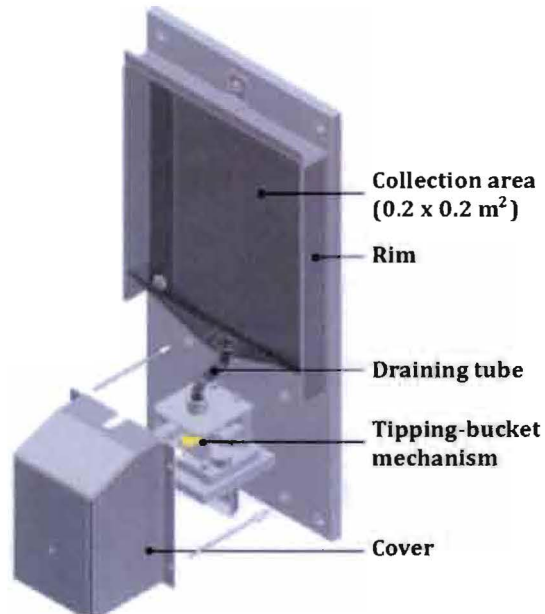


Figure 2.16: Selected wind-driven rain gauge (Briggen et al., 2009).

Four wind-driven rain gauges are placed on the test facade. Figure 2.17 shows the measurement positions of the rain gauges. To gain good insight into the wind-driven rain distribution on the test facade, the rain gauges are placed around the test samples. There were some limitations to the positions of the gauges however. The gauges are kept clear from the test samples to prevent them from covering the test samples. Besides this the positions were limited because of the presence of glass surfaces at the left side of the test samples and the need to preserve symmetry. Furthermore the gauges are placed somewhat close to each other because of the involvement of a study on WDR gauges (Bouten, 2010).

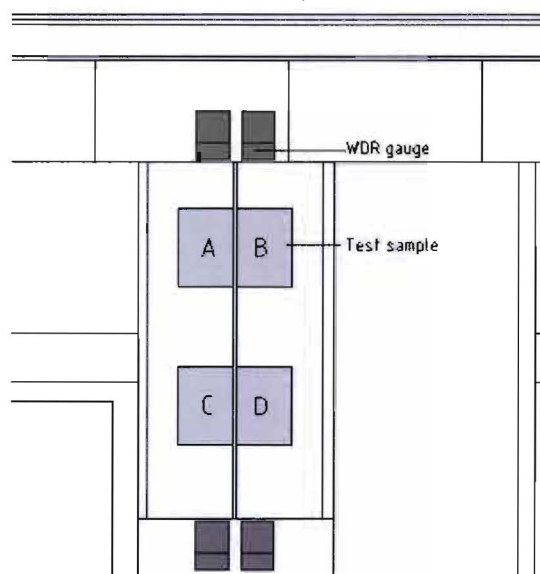


Figure 2.17: Position of WDR gauges on the test facade.

2. Experimental research

Runoff

When the bricks are fully saturated or when the rainfall intensity on the facade is higher than the maximum absorption rate of the bricks (i.e. surface saturation), runoff can occur. The amount of runoff is measured by means of so-called runoff reservoirs, specially designed and manufactured for this study. The runoff reservoir is connected to a tipping-bucket to measure the amount of water. Figure 2.18 shows the reservoir.

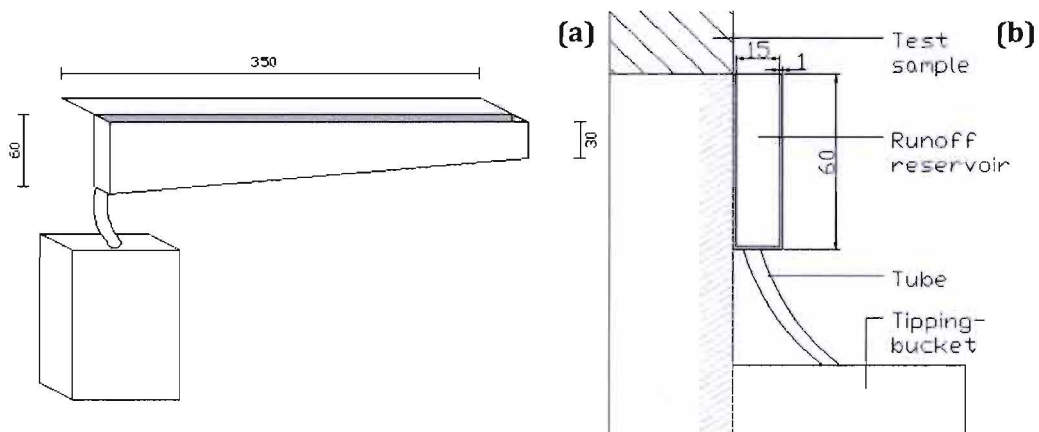


Figure 2.18: (a) Three-dimensional image and (b) detail of the runoff reservoir. Dimensions are in mm.

Furthermore drains are placed above each test sample to prevent runoff water of higher situated bricks from flowing into the test samples. In figure 2.19 the drain is depicted. Figure 2.20 shows the runoff reservoirs and drains on the test facade.

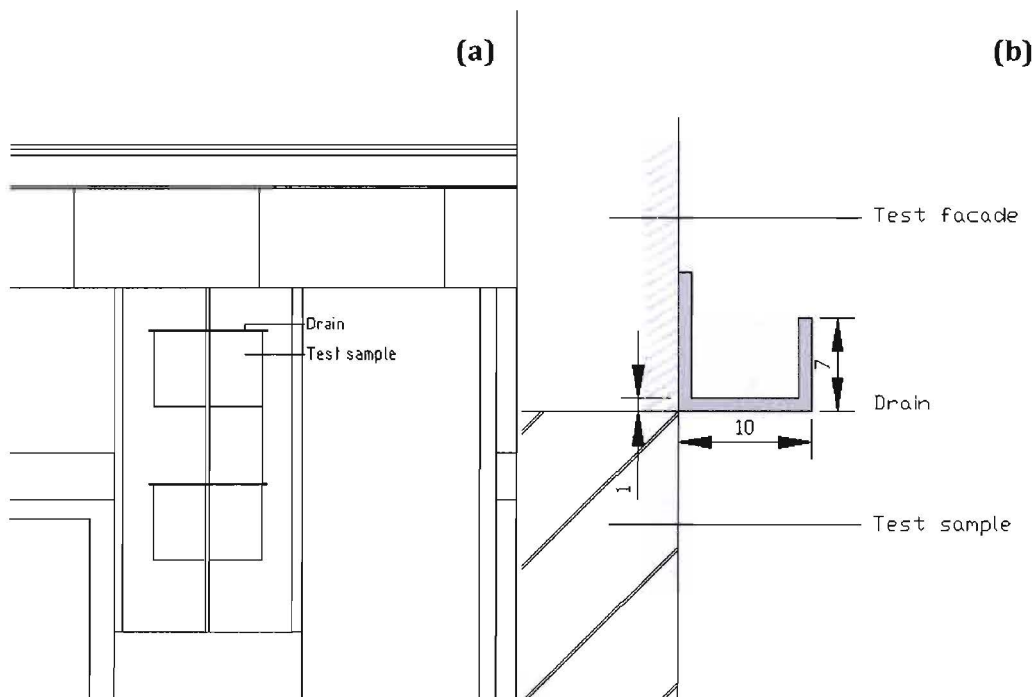


Figure 2.19: (a) Position of the drain indicated on the test facade and (b) detail of the drain. Dimensions are in mm.

2. Experimental research

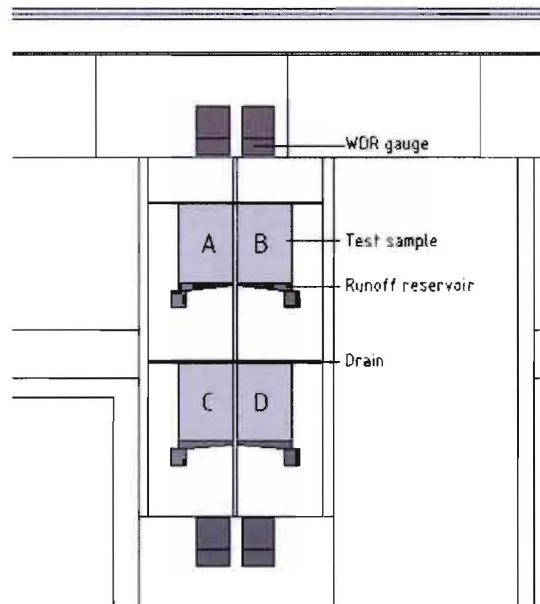


Figure 2.20: Position of the runoff reservoirs and drains on the test facade.

In figure 2.21 a final image of the test facade is presented in which all components discussed above are included.



Figure 2.21: Final image of the test facade.

2.2.4 Data processing

The horizontal rainfall intensity as well as the wind-driven rain intensity on the test facade are measured. The moisture response of the test facade to this rain is determined by means of the weighing setup. With this setup the mass change in time of the material samples is registered. Since this mass change is due to rainfall, the rainfall interception (RI) of the porous material samples is given by:

$$RI = \frac{\Delta m}{V} \quad (2.1)$$

where:

RI	= rainfall interception	[kg/m ³]
Δm	= mass change	[kg]
V	= volume of the test sample	[m ³]

Note that the immediate evaporation during rainfall is not included this way and therefore RI can be slightly underestimated. Determining RI per unit of volume can be a subject of discussion. In the field of hydrology RI is usually expressed in kg/m². In the field of building physics expressing RI in kg/m³ is more meaningful. Porous building materials can intercept significant quantities of water due to their ability to absorb water and therefore it is logical to take the thickness into account as well. Equation 2.1 does not apply for the non-porous building materials, since the rainwater is not absorbed by the material, but stored on its surface. For the comparison between the results of the porous and non-porous building materials, the mass change per unit of area is considered.

2.2.5 Results

Figure 2.22 presents the mass change of all material samples. The wind-driven rain is depicted as well. In figure 2.23 a detail of the mass change in time is presented.

2. Experimental research

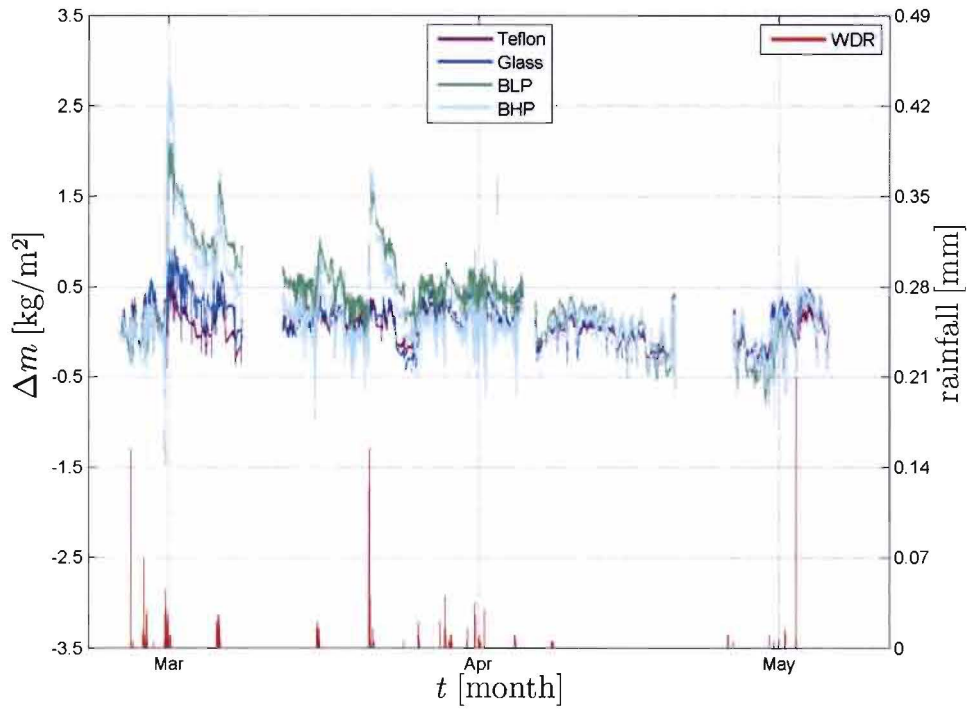


Figure 2.22: Mass change in time of the four material samples during the measurement period and WDR amount during the same period.

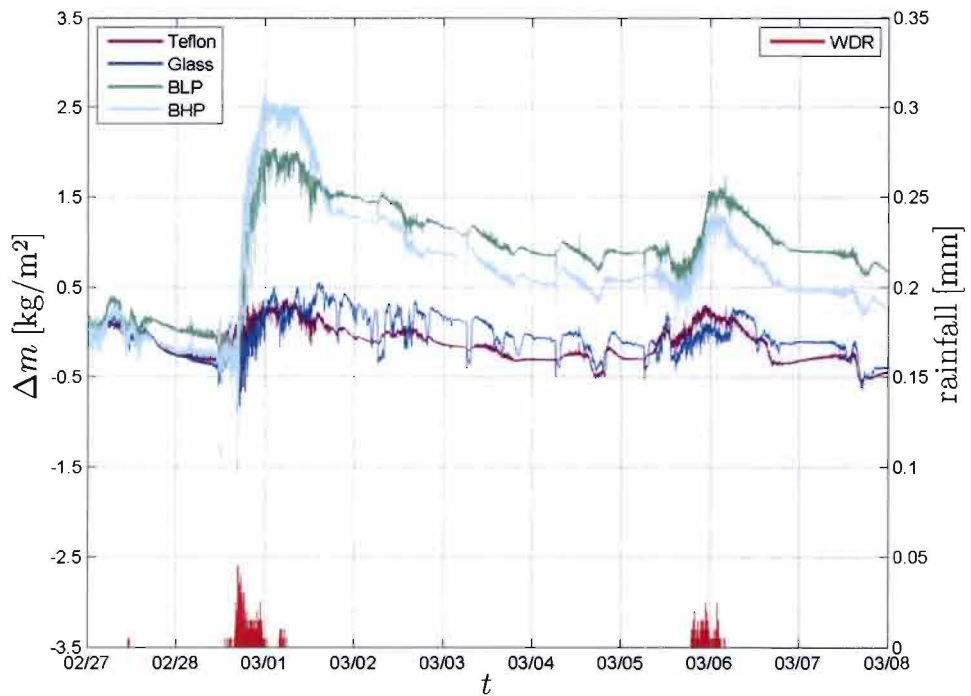


Figure 2.23: Detail of mass change in time of the four material samples and WDR amount during the same period.

2. Experimental research

From these figures can be seen that the porous building materials accommodate for a larger mass change due to rainfall than the non-porous building materials, as expected. It is shown that all material samples do follow the same trend, only for the porous building materials a substantial mass change is observed during rain events, due to their ability to absorb water and not only hold water on their surface.

For the two non-porous building materials the maximum value for Δm is observed for teflon and glass in turn. From the laboratory experiment (section 2.3.5) is expected that teflon holds a larger amount of water. Differences are very small however and can also be attributed to wind influences on the test samples.

In figures 2.24, 2.25 and 2.26 the results of the two types of brick are compared.

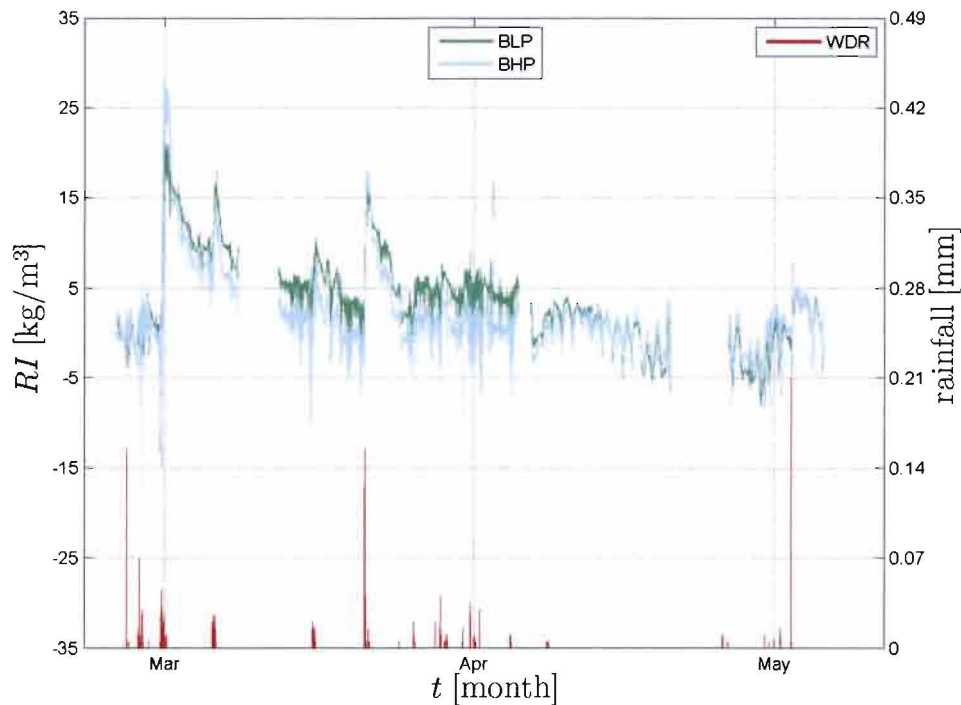


Figure 2.24: Mass change in time of the two porous building materials during the measurement period and WDR intensity during the same period.

2. Experimental research

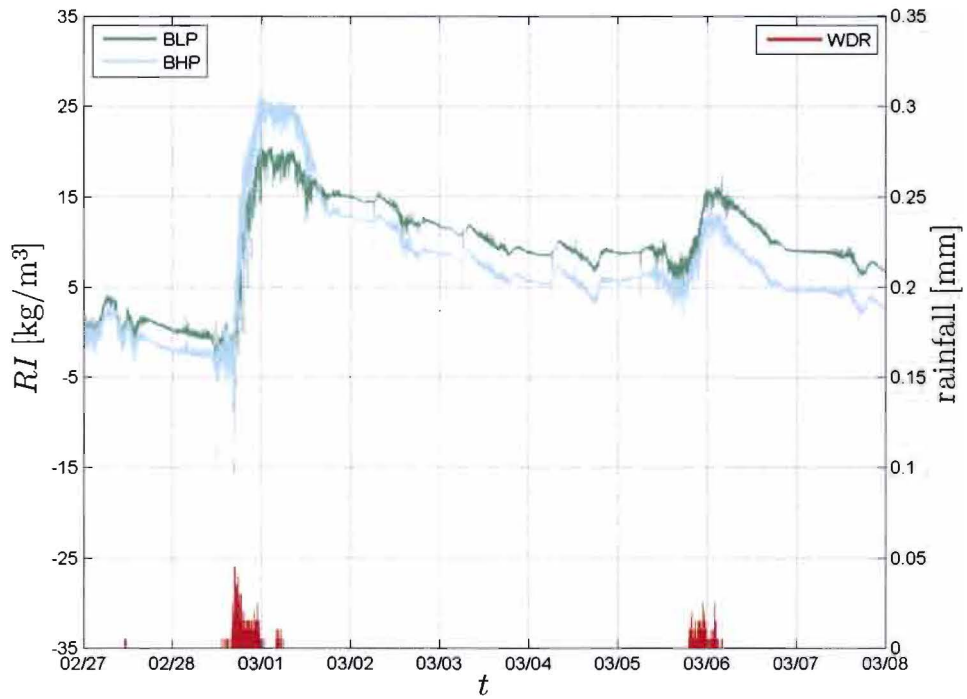


Figure 2.25: Detail of mass change in time of the four material samples and WDR amount during the same period.

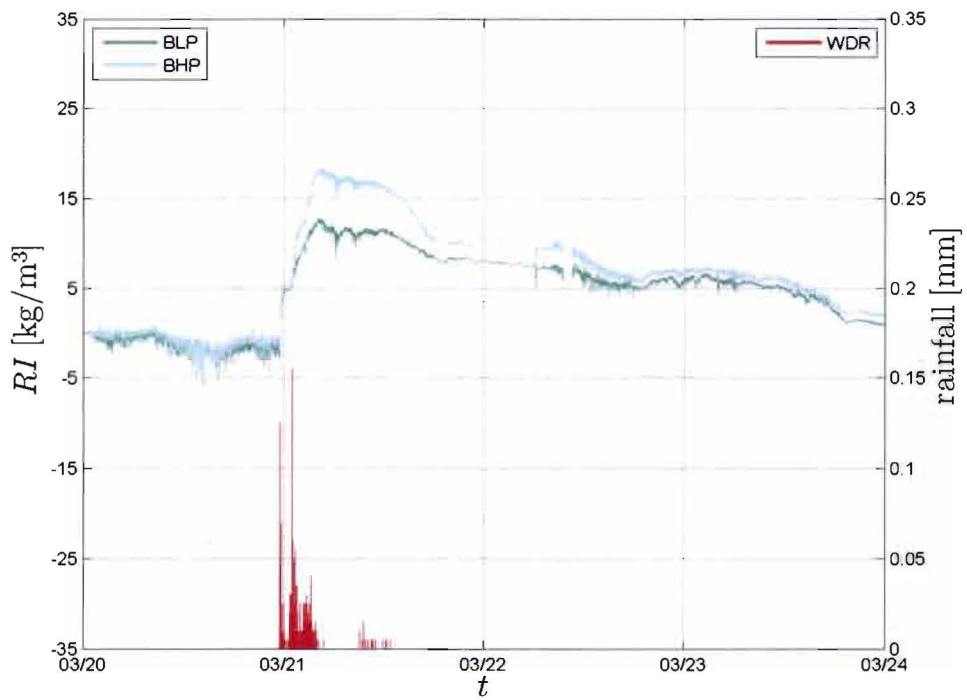


Figure 2.26: Detail of mass change in time of the four material samples and WDR amount during the same period.

2. Experimental research

In principle the maximum amounts of RI are observed for the brick with high porosity (BHP) due to its higher hygric sorptivity and moisture capacity. For this reason as well the brick with low porosity (BLP) shows a slower drying process than the other type of brick. Due to this slower drying process of BLP the moisture content in the material at the beginning of a next rain event is higher than for BHP. If this concerns a moderate rain event a higher value of Δm is therefore obtained, as can be observed for the second rain event in figure 2.25. Furthermore it is noticeable that for some rain events, like the rain event depicted in figure 2.26, the difference in mass change between the value at the beginning of the rain event and the maximum value during that rain event is higher for BHP, even though the same amount of WDR is received. This implies that for BLP runoff occurred and this was indeed measured by the runoff reservoir. For the BHP test sample no runoff occurred during the measurement period. The amount of rainfall interception plus the amount of runoff in a certain period must be equal to the available amount of WDR in that period. This is verified for the major rain event at the 28th of February. The results are presented in table 2.2.

Table 2.2: WDR on a test sample, mass change and runoff of the test sample for the rain event of February 28th.

WDR [kg]	Δm_{BHP} [kg]	Δm_{BLP} [kg]	runoff _{BLP} [kg]
0.466	0.430	0.330	0.112

Since no runoff occurred for BHP and therefore all available water is absorbed, the weight change of the BHP test sample during the rain event is a measure for the amount of available WDR during this rain event. The value of WDR obtained by the WDR gauge slightly differs from the total mass change of the BHP sample however. This may be attributed to the fact that not all raindrops falling onto the facade are available for absorption, due to splashing and bouncing of droplets (Blocken et al., 2006, Abuku et al., 2009). This effect can be underestimated by the WDR gauge because of its lower surface roughness than the bricks and the presence of a rim which can still collect droplets that splash or bounce off (Abuku et al., 2009). Furthermore due to immediate evaporation during the rain event, RI and therefore Δm_{BHP} as well can be slightly underestimated. Taking Δm_{BHP} as a measure for the amount of available WDR it is verified that RI (mass change) of BLP plus its amount of runoff is approximately equal to the amount of available WDR.

As mentioned above, no runoff occurred for BHP. This means that all available WDR is intercepted by the material, so RI by BHP is 100%. The value for BLP is based on the mass change of BHP yielding a value of RI by BLP of at least 76.6%. This is the minimum value of RI for this type of brick, obtained during the major rain event of February 28th. Figure 2.27 presents the cumulative amounts of horizontal rainfall and WDR.

2. Experimental research

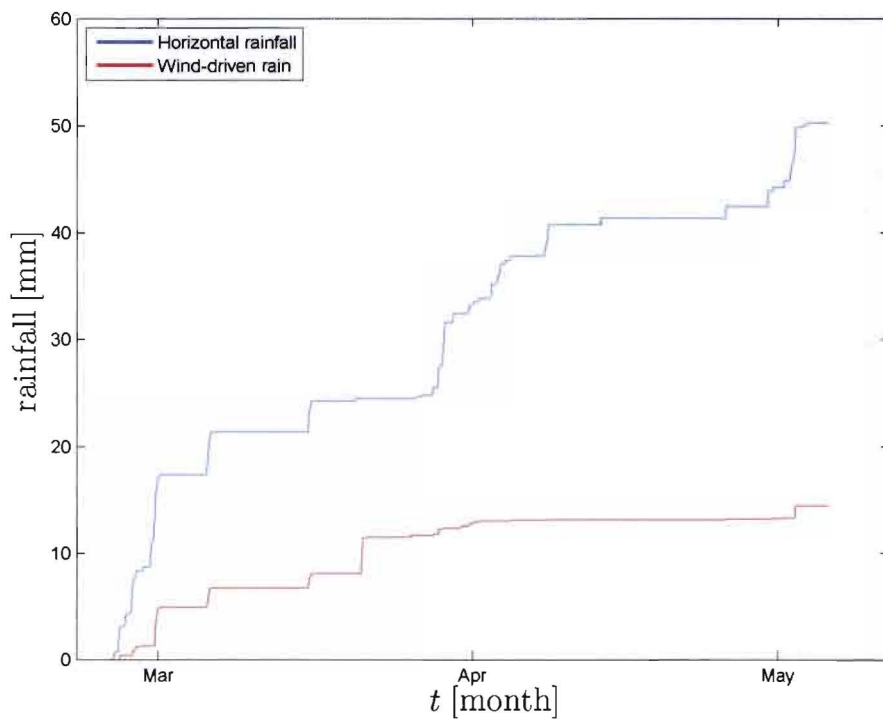


Figure 2.27: Cumulative amounts of horizontal rainfall and WDR during the measurement period.

An overall catch ratio of 0.24 is obtained, which means that 24% of the horizontal rainfall intensity is falling onto the test facade as WDR. RI as a percentage of WDR is a measure of the performance of the material regarding RI. By expressing RI as a percentage of the total horizontal rainfall other influences like the orientation of the facade and the wind direction are taken into account as well. When the amount of RI is low, in this case it is not necessarily due to a bad performance regarding RI by the material. It is also possible that almost no moisture supply was present because only a small percentage of the horizontal rainfall was received by the facade as WDR. This is shown in figure 2.27, where for example at the end of March and the end of April large quantities of horizontal rainfall are measured but almost no WDR is observed. Therefore RI is expressed as a percentage of WDR which means that $RI_{BHP}=100\%$ and $RI_{BLP}>76.7\%$ for the considered measurement period.

2.3 Laboratory experiments

The second part of the experimental research considers laboratory experiments. Laboratory experiments are executed in order to determine the various moisture-related material properties of two different types of brick. These material properties are used as input for the numerical model.

The water absorption coefficient and capillary moisture content are determined at the laboratory of Building Physics and Systems at the Eindhoven University of Technology, the Netherlands. Experiments regarding porosity, density, wetting and drying, diffusivity and permeability are executed at the laboratory of Building Physics at the Catholic University in Leuven, Flanders, Belgium.

Two types of brick are tested

- | | | |
|----|------------------|-----------------------------------|
| 1. | Product name: | Handvorm Dommelrood WF |
| | Factory: | Wienerberger |
| | Manufacturer: | Wienerberger BV |
| | Product number: | 18400 |
| | Product code: | 18400A-1125 |
| | Type of product: | Brick |
| | Density : | 1800 kg/m ³ |
| 2. | Product name: | RBB-WF voll |
| | Factory: | Wienerberger |
| | Manufacturer: | Wienerberger Ziegelindustrie GmbH |
| | Product number: | 34477230 |
| | Product code: | 34477230-1344 |
| | Type of product: | Brick |
| | Density: | 1950 kg/m ³ |

The density given above is the value provided by the manufacturer of the bricks. In this study the density is experimentally determined as well. These results are given in section 2.3.2

Henceforth, the Handvorm Dommelrood WF brick will be referred to as 'BHP' (Brick with High Porosity) and the RBB-WF voll brick will be referred to as 'BLP' (Brick with Low Porosity).

Furthermore the water storage of different glass samples is measured aiming to determine the order of magnitude of rainfall interception by non-porous building materials. Therefore the difference in storage of three types of glass is evaluated. The experiment is performed at the laboratory of Building Physics at the Eindhoven University of Technology, the Netherlands.

2.3.1 Determination of the water absorption coefficient and capillary moisture content

The water absorption coefficient and capillary moisture content of the two types of brick are obtained from a one-dimensional free water uptake experiment. This experiment is executed according to the standard NEN-EN-ISO 15148 (2002).

Apparatus

For the experiment the following equipment is used:

- A water tank that is capable to keep the water level constant at 5 ± 2 mm above the base of the specimen. The water tank is connected to a faucet for a constant water supply and an overflow is made to drain away the excess water. Metal pipes are used to keep the specimen at least 5 mm clear of the base of the water tank. Figure 2.28 shows this principle.

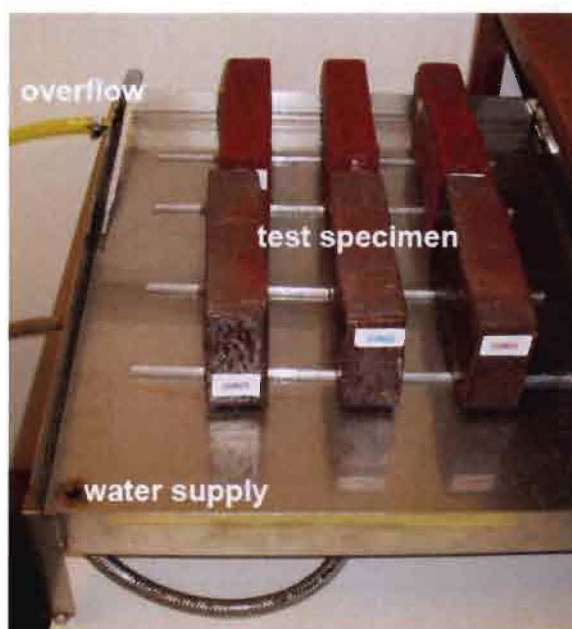


Figure 2.28: Water tank with water supply, overflow and supported bricks.

- Balance, capable of weighing a test specimen to an accuracy of $\pm 0,1\%$ of the mass of the specimen.
 - Timer.
 - Sponge or cloth to remove the not absorbed water before weighing.
 - Escort for monitoring the room temperature and relative humidity.
 - Escort reader and software to read the information on the escort.
 - Mercury thermometer for monitoring the water temperature.
- Specifications of the used equipment can be found in Appendix C.

Test procedure

Date and duration of the test:

BHP

Start: 12-11-2009 ; 09.30 h

End: 13-11-2009 ; 09.30 h

BLP

Start: 13-11-2009 ; 08.00 h

End: 16-11-2009 ; 09.00 h

Six bricks of each type are tested. Before testing, the bricks are dried for 48 hours in an oven at a temperature of 105 °C.

The part of the brick that is immersed is that part that comes in contact with water during actual use of the brick. The other sides of the bricks are sealed with a water and vapor tight sealant to obtain one-dimensional moisture transport. Figure 2.29 shows which sides of the stone are sealed. Paraffin wax is used as sealant.

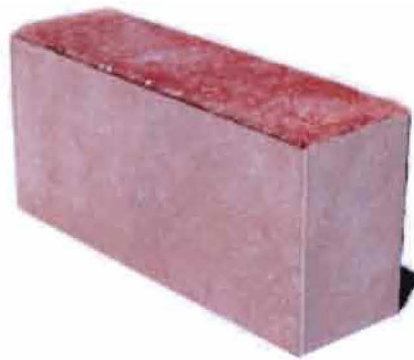


Figure 2.29: The sides of the bricks that are sealed.

Subsequently, the dimensions of the bricks and the initial weight are determined. Then, the bricks are immersed in the water tank. The water absorption is determined by measuring the change in mass of the test specimen at various points in time, over a period of at least 24 hours. The water adhering to the surface and not absorbed by the product is removed by blotting with a cloth before weighing the specimen.

Data processing

First the area A [m²] of the base is calculated. Subsequently, the difference between the mass at each weighing and the initial mass per area is calculated:

$$\Delta m_t = \frac{(m_t - m_i)}{A} \quad (2.2)$$

where:

Δm_t	= mass gain per face area after time t	[kg/m ²]
m_t	= mass at each weighing	[kg]
m_i	= initial mass	[kg]
A	= area of the base	[m ²]

Δm_t is then plotted against the square root of the weighing time, \sqrt{t} . After a short period of stabilization, a straight line can be drawn through the values of Δm_t against \sqrt{t} . When this line is extended back to zero time, where it cuts the vertical axis, Δm_0

2. Experimental research

is obtained. This linear function of the form $y = ax + b$ is determined by means of the least squares method, to obtain the best fit for the data. The water absorption coefficient A_w is calculated from:

$$A_w = \frac{\Delta m'_{t_f} - \Delta m'_0}{\sqrt{t_f}} \quad (2.3)$$

where:

A_w	= water absorption coefficient	$[\text{kg}/\text{m}^2\text{s}^{1/2}]$
$\Delta m'_{t_f}$	= value of Δm on the straight line at time t_f	$[\text{kg}/\text{m}^2]$
t_f	= duration of the first absorption phase	$[\text{s}]$

The value of A_w corresponds to the slope a of the curve $y = ax + b$

At a certain moment in time the sorption curve reaches a transition point. The measuring points after this transition point are again described by a straight line. This is a linear function of the form $y = cx + d$ and is determined by means of the least squares method as well.

The capillary moisture content is obtained by calculating the y-value of the intersection of the two straight lines and dividing this value by the third dimension, which is the height, of the specimen.

Results

Table 2.3 and 2.4 show the test conditions during the experiments.

Table 2.3: Test conditions for BHP.

$T_{a,\min}$ [°C]	$T_{a,\max}$ [°C]	$T_{w,\min}$ [°C]	$T_{w,\max}$ [°C]	RH_{\min} [%]	RH_{\max} [%]
21,1	21,7	18,5	20	33	48,5

Table 2.4: Test conditions for BLP.

$T_{a,\min}$ [°C]	$T_{a,\max}$ [°C]	$T_{w,\min}$ [°C]	$T_{w,\max}$ [°C]	RH_{\min} [%]	RH_{\max} [%]
21,1	21,7	18	19	43,5	48,5

Figure 2.30 presents a typical result of the water absorption in time. The blue lines represent the linear functions $y = ax + b$ and $y = cx + d$. In figure 2.31 the water absorption in time for all test bricks of BHP is shown. Figure 2.32 depicts the water absorption in time of the BLP bricks. The figures of the water absorption in time of all test samples are included in Appendix D.

2. Experimental research

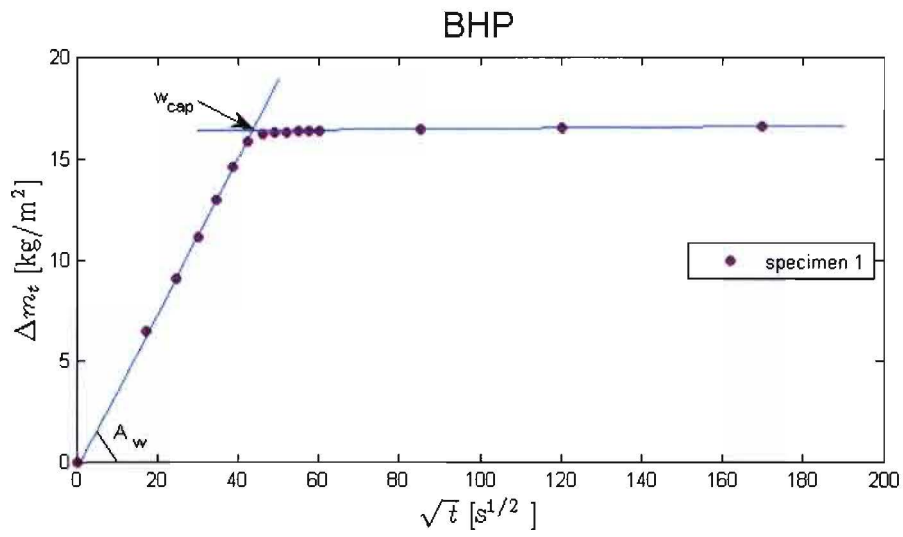


Figure 2.30: Typical result of the water absorption in time.

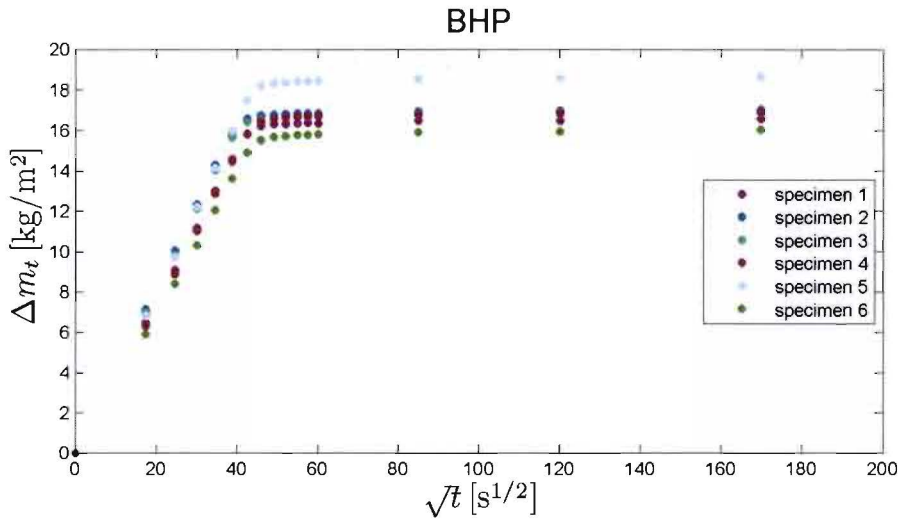


Figure 2.31: Water absorption in time for bricks 1 to 6 of BHP.

2. Experimental research

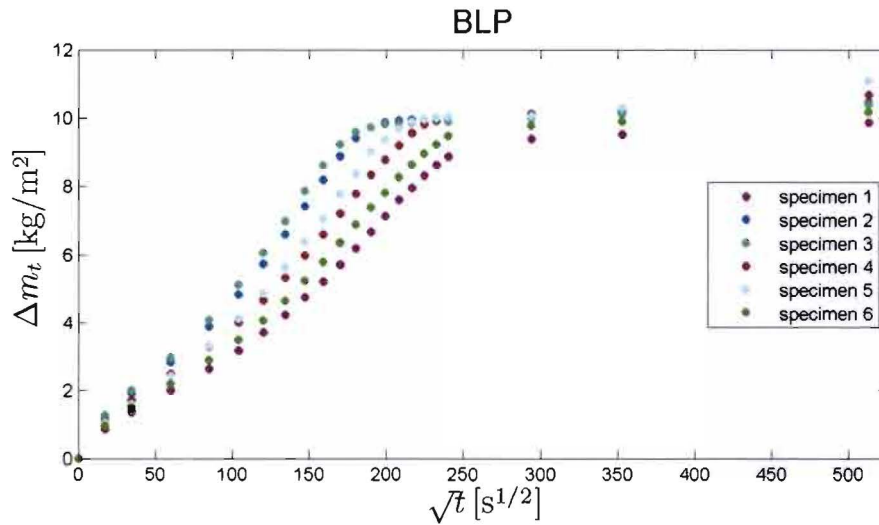


Figure 2.32: Water absorption in time for bricks 1 to 6 of BLP.

In table 2.5 and 2.6 the values for the water absorption coefficient and capillary moisture content of the two types of brick are given.

Table 2.5: Water absorption coefficient and capillary moisture content for the bricks of BHP.

BHP

brick	A_w [kg/(m ² s ^{1/2})]	w_{cap} [kg/m ³]
1	0,39	167,13
2	0,42	170,21
3	0,42	168,69
4	0,39	170,46
5	0,44	184,47
6	0,36	162,99
mean	0,40	170,66

Table 2.6: Water absorption coefficient and capillary moisture content for the bricks of BLP.

BLP

brick	A_w [kg/(m ² s ^{1/2})]	w_{cap} [kg/m ³]
1	0,04	92,53
2	0,05	99,26
3	0,05	98,03
4	0,04	99,19
5	0,05	97,35
6	0,04	96,19
mean	0,04	97,09

From the above mentioned figures and tables is seen that the water absorption coefficient and capillary moisture content of BHP are much higher than the water absorption coefficient and capillary moisture content of BLP. This is expected, since the BHP brick is characterized as a higher porous material than the BLP brick.

2.3.2 Determination of the open porosity, density and vacuum saturation moisture content

The open porosity, bulk density and matrix density and vacuum saturation moisture content of two types of brick are obtained from a vacuum saturation experiment. The bulk density is given by the ratio of the dry mass of a specimen to its volume, while the matrix density is defined as the ratio of the dry mass of a specimen to the volume of the solid matrix, including closed pores.

In Roels et al. (2003) standard methodologies for the determination of material properties regarding moisture are given. Most of the following information is based on this work.

Apparatus

The following apparatus is used for this experiment:

- Airtight container connected to a vacuum pump and a water supply as shown in figure 2.30.
- Balance, capable of weighing a test specimen to an accuracy of $\pm 0,1\%$ of the mass of the specimen.
- Sponge or cloth to remove the not absorbed water before weighing.
- Test setup to measure the weight of the displaced volume of water.

Test procedure

Date and duration of the test:

BHP

Start: 18-01-2010 ; 13.00 h

End: 19-01-2010 ; 17.00 h

BLP

Start: 18-01-2010 ; 13.00 h

End: 19-01-2010 ; 17.00 h

For each type four test specimens are tested.

Before testing, the specimens are dried for about 48 hours in an oven at a temperature of 105 °C. Thereafter, the initial weight is determined.

The test specimens are placed in the airtight container and the air in the container is evacuated with a vacuum pump for several hours. This setup is shown in figure 2.33. Subsequently, water is supplied to the container at a low inflow rate. Once the specimens are immersed, the water supply is cut and for the next 24 hours the specimens remain under water.

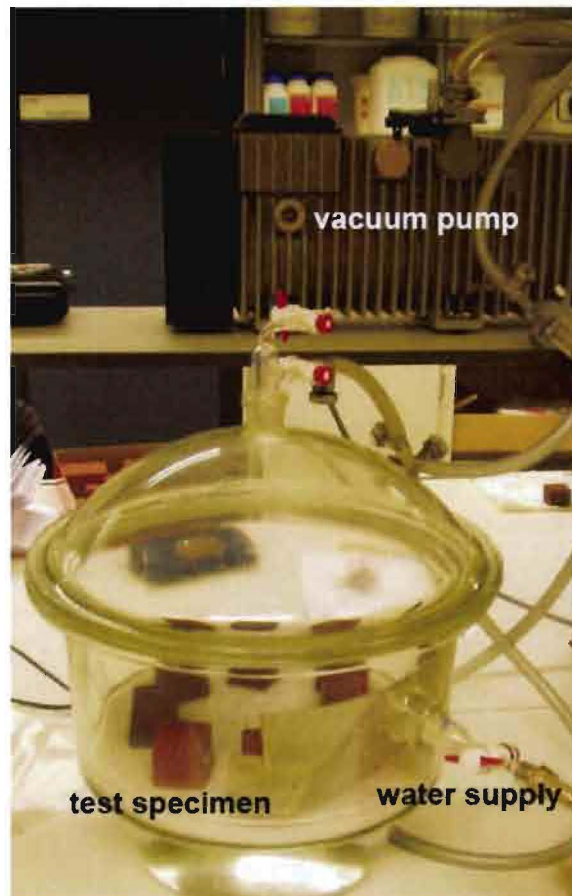


Figure 2.33: Airtight container with test specimens.

After 24 hours the specimens are removed from the container and excess water is removed before weighing. Next the weight of the displaced volume of water is determined. This corresponds to the volume of the specimen. Figure 2.34 shows the setup.

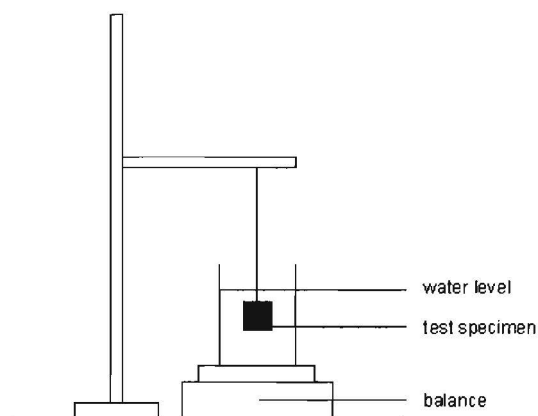


Figure 2.34: Schematic overview of the test setup for the determination of the weight of the displaced volume of water.

2. Experimental research

Data processing

The initial mass of the dry specimens m_i is determined before testing. m_{sat} represents the mass of the water-saturated specimens. The difference in mass between a tank filled with water with and without the saturated specimen is called m_{diff} . This is the weight of the displaced volume of water. The values are depicted in table 2.7 and 2.8.

Table 2.7: Initial weight, saturated weight and weight of the displaced liquid of the specimens of BHP.

BHP			
specimen	m_i [kg]	m_{sat} [kg]	m_{diff} [kg]
1	0,1163	0,1345	0,0617
2	0,1154	0,1337	0,0620
3	0,1138	0,1319	0,0612
4	0,1152	0,1336	0,0619
mean	0,1152	0,1334	0,0617

Table 2.8: Initial weight, saturated weight and weight of the displaced liquid of the specimens of BLP.

BLP			
specimen	m_i [kg]	m_{sat} [kg]	m_{diff} [kg]
1	0,1267	0,1396	0,0616
2	0,1233	0,1366	0,0604
3	0,1264	0,1394	0,0615
4	0,1232	0,1357	0,0594
mean	0,1249	0,1378	0,0607

From the results in table 2.7 and 2.8 the volume V of the samples is determined:

$$V = \frac{m_{diff}}{\rho_w} \quad (2.4)$$

where:

$$\begin{aligned} V &= \text{volume of the sample} && [\text{m}^3] \\ m_{diff} &= \text{weight of displaced liquid} && [\text{kg}] \\ \rho_w &= \text{density of liquid water} && [1000 \text{ kg/m}^3] \end{aligned}$$

The open porosity, bulk density and matrix density and the saturation moisture content are then calculated from:

$$\psi_o = \frac{V_w}{V} = \frac{(m_{sat} - m_i) / \rho_w}{V} \quad (2.5)$$

2. Experimental research

$$\rho = \frac{m_i}{V} \quad (2.6)$$

$$\rho_{mat} = \frac{m_i}{V(1 - \psi_o)} \quad (2.7)$$

$$w_{sat} = \psi_o \rho_w = \frac{m_{sat} - m_i}{V} \quad (2.8)$$

where:

ψ_o	= open porosity of sample	[-]
V_w	= maximum volume of water in sample	[m ³]
V	= volume of sample	[m ³]
m_{sat}	= saturated weight of sample	[kg]
m_i	= initial weight of sample	[kg]
ρ_w	= density of liquid water	[1000 kg/m ³]
ρ	= bulk density of sample	[kg/m ³]
ρ_{mat}	= matrix density of sample	[1000 kg/m ³]
w_{sat}	= saturation moisture content	[kg/m ³]
m_{sat}	= saturated weight of sample	[kg]

Results

Table 2.9 and 2.10 depict the results for BHP and BLP respectively. The volume, open porosity, bulk density, matrix density and saturation moisture content are shown.

Table 2.9: Volume, open porosity, bulk density, matrix density and saturation moisture content of BHP.

BHP

specimen	V [m ³]	ψ_o [-]	ρ [kg/m ³]	ρ_{mat} [kg/m ³]	w_{sat} [kg/m ³]
1	0,000062	0,29	1884,56	2670,72	294,36
2	0,000062	0,30	1859,56	2641,73	296,08
3	0,000061	0,30	1858,09	2641,84	296,67
4	0,000062	0,30	1861,81	2647,39	296,74
mean	0,000062	0,30	1866,01	2650,42	295,96

2. Experimental research

Table 2.10: Volume, open porosity, bulk density, matrix density and saturation moisture content of BLP.

BLP

specimen	V [m ³]	Ψ _o [-]	ρ [kg/m ³]	ρ _{mat} [kg/m ³]	w _{sat} [kg/m ³]
1	0,000062	0,21	2056,23	2598,80	208,78
2	0,000060	0,22	2040,30	2615,51	219,92
3	0,000061	0,21	2057,07	2609,07	211,57
4	0,000059	0,21	2074,41	2630,85	211,50
mean	0,000061	0,21	2057,00	2613,56	212,94

The open porosity of BLP is lower than the open porosity of BHP. This is expected however, since BLP is characterized as a less absorbent brick than BHP by the manufacturer. For this reason the density of BLP is higher. The value of the experimentally determined density differs (4-5%) from the value provided by the manufacturer. It is assumed that the experimentally determined value is more accurate. The fact that BHP has a higher porosity than BLP results in a higher value of the saturated moisture content as well.

2.3.3 Determination of the moisture retention curve

Different experiments are carried out to determine the moisture retention curve of the two types of brick. The first part consists of a mercury intrusion porosimetry experiment. Besides this, the hygroscopic curve or isothermal adsorption curve is determined. Furthermore a pressure plate experiment is executed to obtain the wetting curve in the over hygroscopic region.

In Roels et al. (2003) a brief description of the mercury intrusion porosimetry technique is presented. The pressure plate technique is explained as well. Most of the following information is based on this work.

Part 1 Mercury intrusion porosimetry

Apparatus

For this experiment a Micromeritics AutoPore IV mercury porosimeter is used.

Test procedure

Date and duration of the test:

BHP

BLP

Start: 19-01-2010 ; 13.00 h

Start: 19-01-2010 ; 13.00 h

End: 20-01-2010 ; 17.00 h

End: 20-01-2010 ; 17.00 h

For each type of brick two specimens are tested.

2. Experimental research

The moisture retention curve is determined by means of a mercury intrusion porosimetry (MIP) experiment. During such an experiment an external pressure is applied to intrude the mercury into the test specimen. For different pressures the mercury intrusion volume is determined.

Data processing

The result of the MIP experiment is a set of mercury intrusion volumes for different mercury pressure values. To convert this so-called mercury retention curve into the moisture retention curve the contact angle and surface tension of both mercury and water are of importance. The capillary pressure can be calculated using the Young-Laplace equation:

$$p_c = \frac{2\sigma}{r} \cos(\theta) \quad (2.9)$$

where:

p_c	= capillary pressure	[Pa]
σ	= surface tension	[N/m]
θ	= contact angle	[°]

and:

$\sigma_{mercury}$	[485 10 ⁻³ N/m]
σ_{water}	[72,6 10 ⁻³ N/m]
$\theta_{mercury}$	[130 °]
θ_{water}	[0 °]

Equation (2.9) can be written for both mercury and water and therefore r can be eliminated.

In order to obtain a mathematical function of the moisture retention curve, a bimodal fit is applied to the measurement data (van Genuchten, 1980).

$$w(p_c) = w_{sat} \sum_{s_i=1}^{s_n} l_i \left(1 + (c_i p_c)^{n_i} \right)^{\left(\frac{1-n_i}{n_i} \right)} \quad (2.10)$$

where:

w	= moisture content	[kg/m ³]
w_{sat}	= saturation moisture content	[kg/m ³]
s_n	= number of subsystems	[-]
l_i	= weight factors	[0 < l_i ≤ 1, $\sum l_i = 1$]
c_i	= model parameter	[-]
n_i	= model parameter	[-]

Results

In figure 2.35 the results of the MIP experiment of the specimens of BHP are depicted. The red line represents the bimodal fit. Figure 2.36 shows the results for BLP.

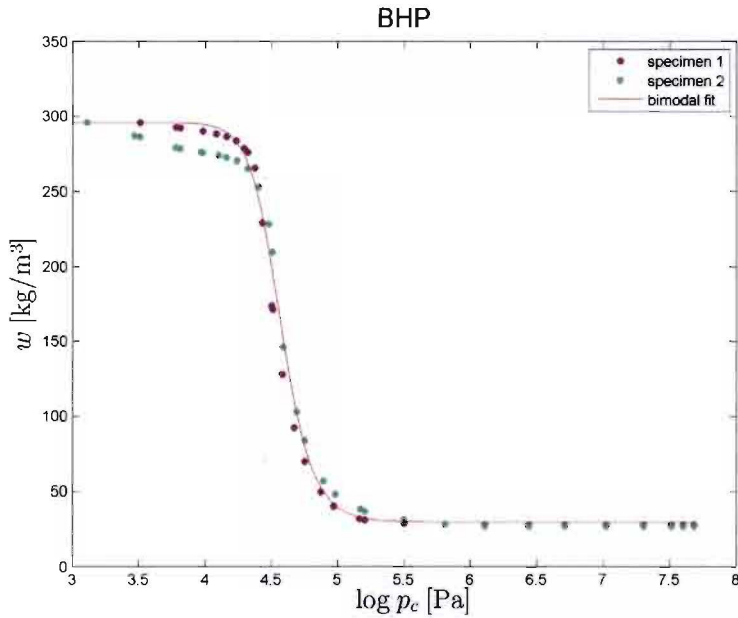


Figure 2.35: Results of the MIP experiment of the specimens of BHP.

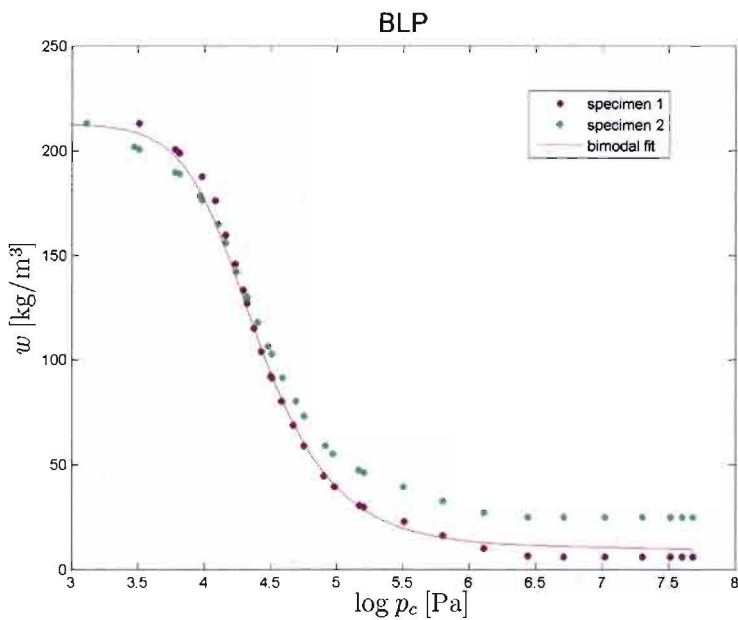


Figure 2.36: Results of the MIP experiment of the specimens of BLP.

The curves for both specimens of BHP show a good overall agreement. For the specimens of BLP however, there is a small difference, especially at higher pressures.

Part 2 Hygroscopic curve

Apparatus

In order to perform this experiment, the following material is needed:

- Two climatic chambers and two climatic boxes
- Four desiccators with different salt in water solutions

Test procedure

Date and duration of the test:

BHP

BLP

Start: 18-01-2010 ; 15.00 h

Start: 18-01-2010 ; 15.00 h

End:

End:

The aim of this experiment is to obtain the hygroscopic curve of the two types of brick. In order to do this, the specimens are conditioned at different relative humidity. A specific relative humidity is obtained using desiccators with salt in water solutions. Each salt solution has its own equilibrium relative humidity. The desiccators are placed in climatic chambers and climatic boxes in order to preserve a constant temperature.

After a certain period of time static sorption equilibrium between the relative humidity of the environment and the moisture content of the specimen is attained.

Equilibrium is reached when repeated weightings at intervals of at least one week, show a maximum mass change of 0,1% (Roels et al., 2003).

Data processing

The initial mass of the dry specimens, m_i , is determined beforehand. The dimensions of the specimens are defined as well. When static equilibrium is reached for a specific relative humidity, the specimens are weighed again. The moisture content for this relative humidity can be defined from:

$$w(RH) = \frac{(m_{eq} - m_i)}{V} \quad (2.11)$$

where:

w	= moisture content	[kg/m ³]
m_{eq}	= mass of specimen at equilibrium	[kg]
m_i	= dry mass of specimen	[kg]
V	= volume of specimen	[m ³]

The temperature of each climatic box and climatic chamber is 23°C. The examined values of relative humidity and corresponding salt solutions are presented in table 2.11.

2. Experimental research

Table 2.11: Relative humidity and corresponding salt solution.

RH [%]	Salt solution
53	Mg(NO ₃) ₂
75	NaCl
86	KCL
94	KNO ₃

Results

For each relative humidity the specimens are weighed at static equilibrium. The increase in mass however is very low, even at high relative humidity. The average mass increase for BHP is 0,024% and for BLP 0,015%. Furthermore no clear correlation between the mass increase and relative humidity is observed.

From these results is concluded that both types of brick are hardly hygroscopic. Therefore these results are not taken into account for the determination of the moisture retention curve.

Part 3 Pressure plate technique

Apparatus

For this experiment the following equipment is used:

- 15 bar pressure plate extractor
- Gas pressure source with pressure regulation (compressor)
- Kaolin paste, to obtain optimal contact between the specimen and the pressure plate
- Cloth to prevent the specimens from sticking to the kaolin paste

Test procedure

Date and duration of the test:

BHP

Start: 18-01-2010 ; 14.00 h

End: 20-01-2010 ; 15.00 h

BLP

Start: 18-01-2010 ; 14.00 h

End: 20-01-2010 ; 15.00 h

For both types of brick 3 specimens are tested.

Figure 2.37 shows the pressure plate extractor and the steps that are taken before starting the experiment. First the pressure plate is placed and connected. Then kaolin paste is applied to the plate. Before placing the specimens on the plate, cloth is put on the kaolin paste. Finally the lid is secured and the extractor is connected to the pressure source.

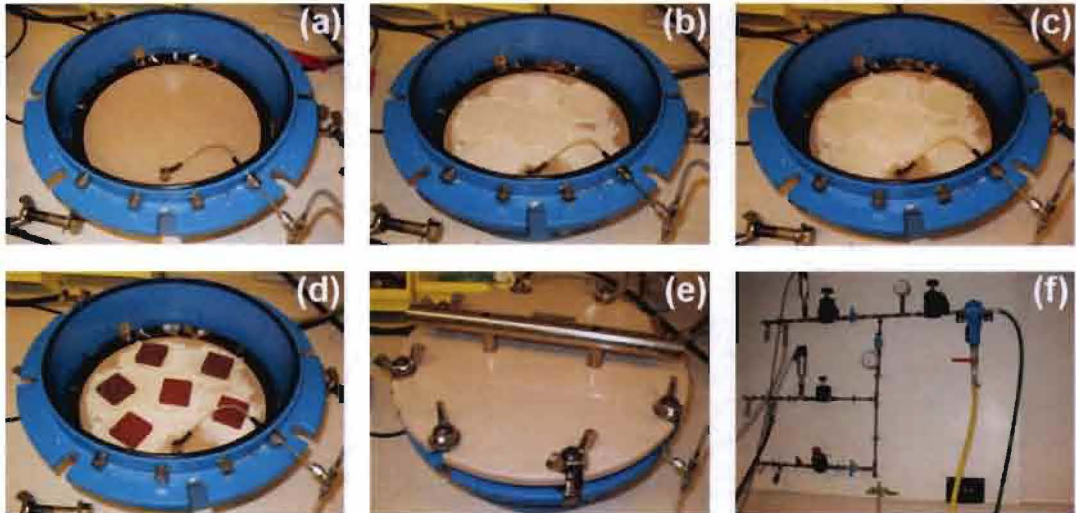


Figure 2.37: Pressure plate extractor, with placement of (a) the pressure plate, (b) the kaolin paste, (c) the cloth, (d) the test specimens and (e) the lid of the extractor. In (f) the pressure source is shown.

The test specimens are capillary saturated and weighed before placing them on the pressure plate. The pressure source is adjusted to different gas pressure values. Gas pressures of 0,102 bar, 0,449 bar, 0,889 bar, and 7,012 bar are considered. These gas pressures (p_g) are applied to one side of the plate while a constant liquid pressure (p_l) is applied to the other side of the brick. In this case the liquid pressure is equal to atmospheric pressure since the tube of water is in contact with the air in the laboratory.

During the experiment, the moisture content of the specimens decreases and for every gas pressure, equilibrium is reached after a certain period of time. At that point the specimens are removed from the plate and weighed again. Subsequently the experiment is continued at a higher pressure level. In figure 2.38 a schematic overview of the test setup is given.

2. Experimental research

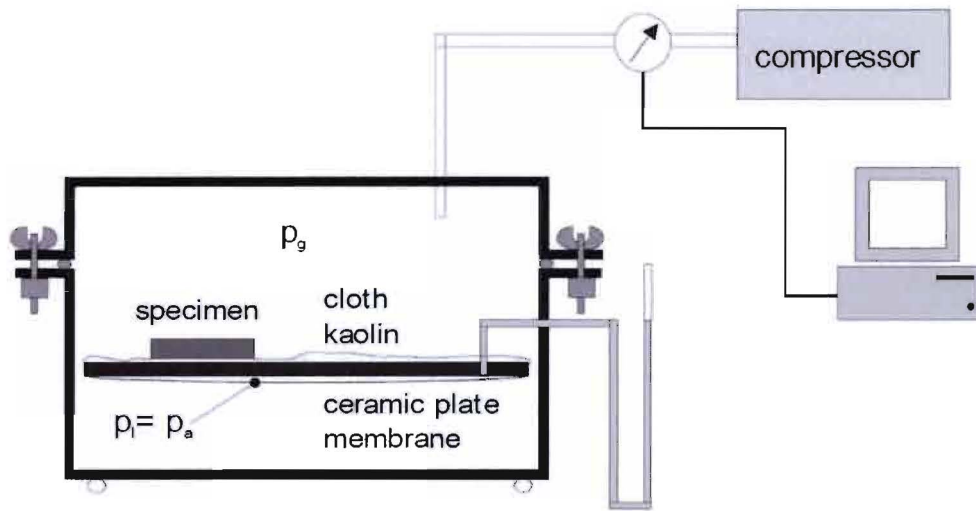


Figure 2.38: Schematic overview of the test setup (Roels et al., 2003).

Data processing

The weight of the dry specimens is determined beforehand. Then the test specimens are capillary saturated and weighed again. With this the moisture content at the beginning of the experiment is obtained. The capillary pressure can be calculated from:

$$p_c = (p_g \cdot 10^5) - p_a \quad (2.12)$$

where:

p_c	= capillary pressure	[Pa]
p_g	= gas pressure	[bar]
p_a	= atmospheric pressure	[10^5 Pa]

For each pressure at equilibrium the specimens are weighed and therefore the moisture content can be determined. The moisture content is plotted against the capillary pressure.

Results

Figure 2.39 describes the moisture content against the capillary pressure for BHP.

2. Experimental research

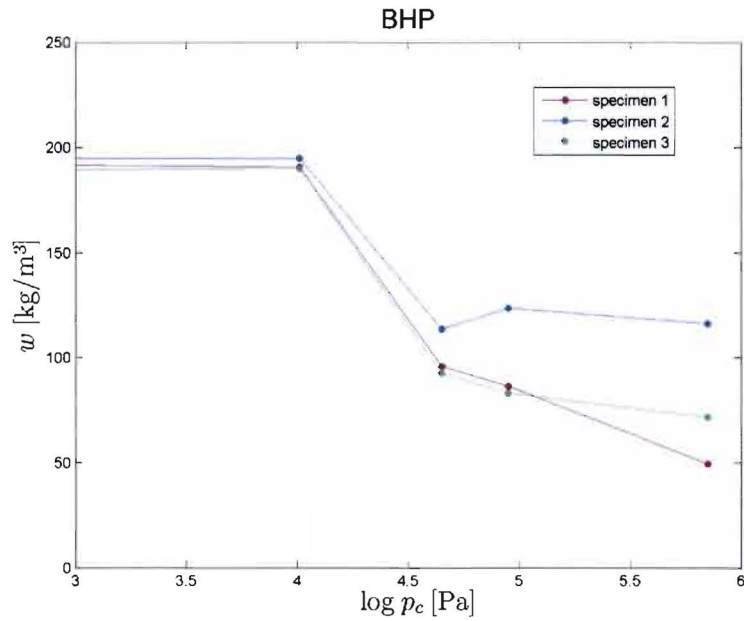


Figure 2.39: Moisture content against capillary pressure of the specimens of BHP.

Figure 2.39 shows for specimen 2 an increase in moisture content while it is expected that the moisture content always decreases with increasing capillary pressure. It is unclear what the reason is for this rise. However, the curve of this specimen seems to differ from the other two curves anyhow. In figure 2.40 the moisture content against the capillary pressure of BLP is shown.

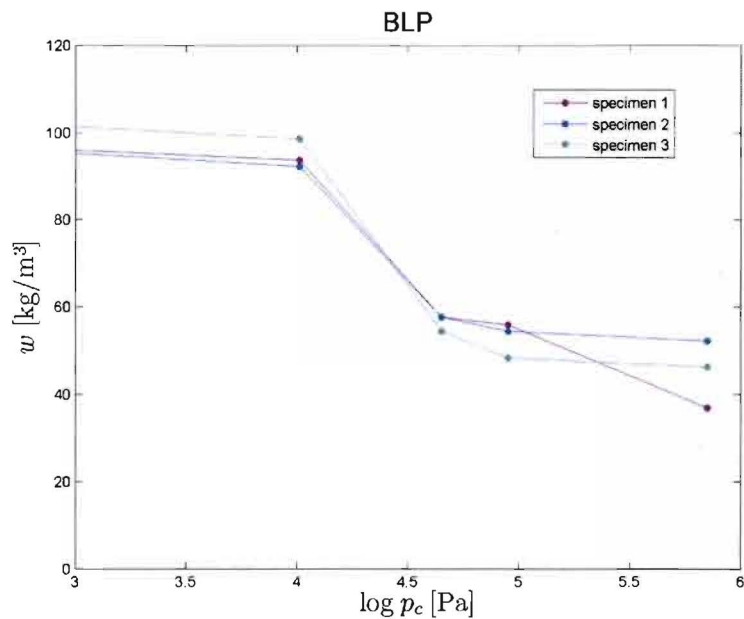


Figure 2.40: Moisture content against capillary pressure of the specimens of BLP.

The three curves in figure 2.40 show a good overall agreement. However, the higher the pressure, the larger divergence is observed.

2. Experimental research

The results of the MIP experiments describe the moisture retention curve starting at saturation moisture content w_{sat} . However, the moisture retention curve starting at capillary moisture content is desired as well. The results of the pressure plate technique are used to obtain this curve. The results are shown in figure 2.41 and 2.42.

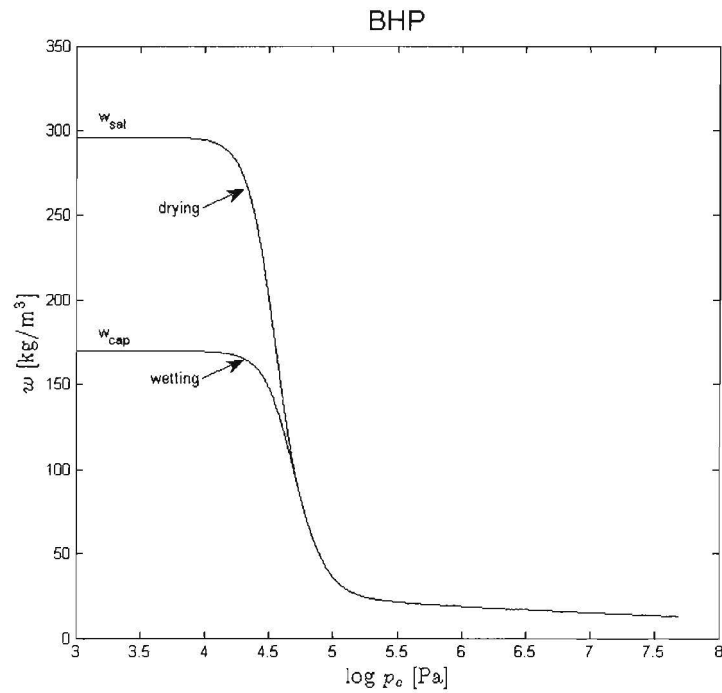


Figure 2.41: Wetting and drying curve for BHP.

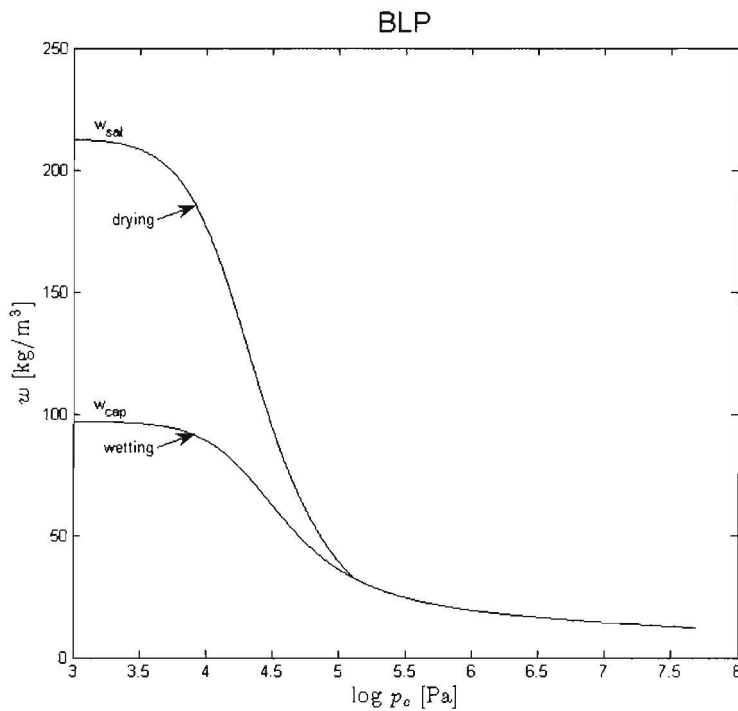


Figure 2.42: Wetting and drying curve for BLP.

The wetting curve is described by means of the mathematical function mentioned in section 2.3.3, part 1 (equation (2.10)). In table 2.12 the values of the weight factors and model parameters of this function are noted. The values are manually adjusted to obtain a good fit through the measurement data. This is done based on trial and error. Therefore these are not necessarily the optimal values, but they provide a possible solution for the bimodal fit. The curve is composed of two separate functions. This means that s_n has a value of 2.

Table 2.12: values of the weight factors and model parameters of the bimodal fit.

BHP	l_i	c_i	n_i	BLP	l_i	c_i	n_i
s1	0.150	2.00E-04	1.000	s1	0.250	2.00E-05	1.100
s2	0.850	2.20E-05	4.000	s2	0.750	5.00E-05	2.000

2.3.4 Determination of the liquid water diffusivity and liquid permeability

In order to determine the liquid water diffusivity and liquid permeability, moisture content profiles are obtained. This is done using X-ray radiography.

In Roels et al. (2006) the use of X-ray radiography for the analysis of moisture flow in porous materials is accurately described. Furthermore, in Carmeliet et al. (2004) a methodology for the determination of the liquid water diffusivity and liquid permeability is given. These works are used as a guideline for the execution and report of the X-ray experiments.

Apparatus

The following apparatus is used for this experiment:

- AEA microfocus X-ray apparatus
- CCD 12-bit camera
- Computer

Test procedure

Date and duration of the test:

BHP

Start: 19-01-2010 ; 10.00 h

End: 20-01-2010 ; 16.00 h

BLP

Start: 19-01-2010 ; 10.00 h

End: 20-01-2010 ; 16.00 h

The test specimen are oven dried beforehand. Next the lateral sides are taped in order to obtain one-dimensional moisture transport. Figure 2.43 gives a schematic overview of the test setup.

2. Experimental research

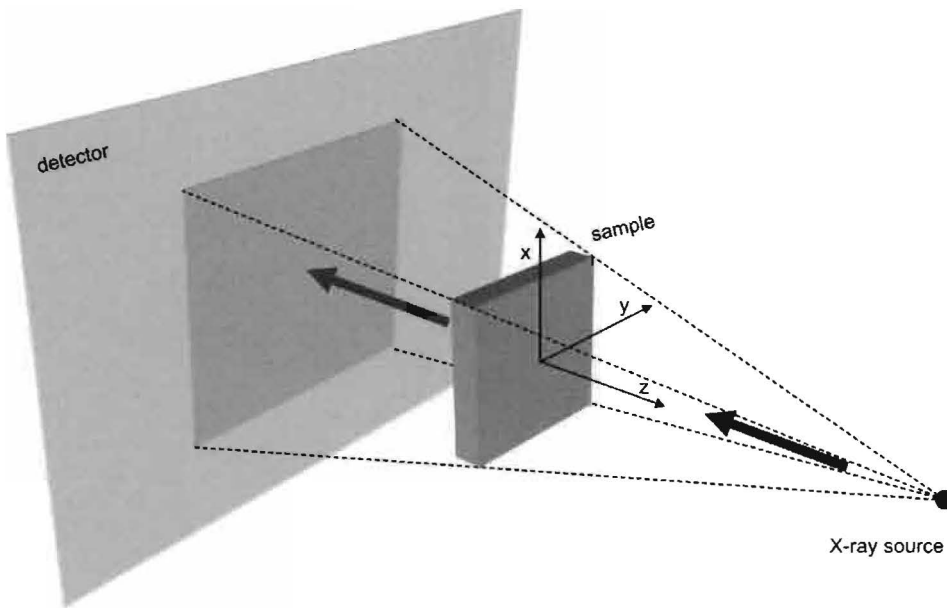


Figure 2.43: Schematic overview of the test setup of the X-ray experiment (Roels et al., 2006).

The dry specimen is placed in an empty water tank, approximately 5 mm clear from the bottom of the tank. An image is taken of the dry specimen. This is the reference image. The camera visualizes intensity levels as grayscales. The size of the image is 1024 x 1024 pixels. Next, water is added to the tank until the water level reaches the bottom of the specimen. At regular time steps an image is taken.

When a material is irradiated with X-rays, the X-rays attenuate because of the interaction with the material. For the determination of the attenuation coefficient of water, a transparent water tank with various widths is used. Figure 2.44 gives a schematic overview of this tank.

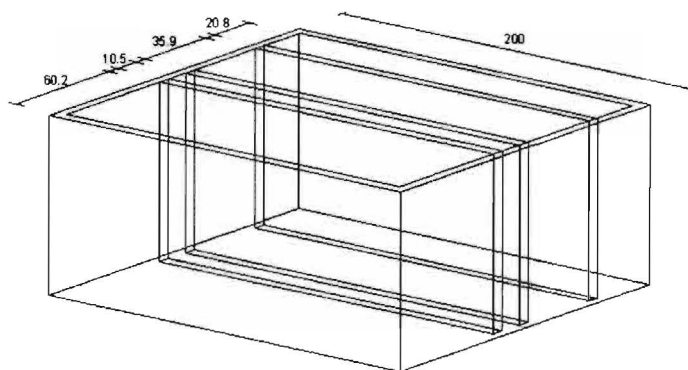


Figure 2.44: Schematic overview of the transparent water tank.

First an image of the empty tank is taken. This is the reference image. Then the parts with the various widths are successively filled with water and for every width an image is taken.

Data processing

For monochromatic X-rays, the relationship between the incident and attenuated X-rays is expressed by Beer's Law (Knoll, 1989):

$$\frac{I}{I_0} = e^{(-\mu d)} \quad (2.13)$$

where:

I	= attenuated X-ray intensity	[keV]
I_0	= incident X-ray intensity	[keV]
μ	= attenuation coefficient	[1/m]
d	= thickness of the specimen	[m]

The incident X-ray intensity is actually the attenuated X-ray intensity for the empty water tank. The attenuation coefficient of water can be determined by first logarithmically subtracting the reference image from the image of a certain width and then plotting this against the corresponding widths. The slope of the curve represents the attenuation coefficient.

Next the moisture content profiles are obtained. The moisture content is determined from:

$$w = -\frac{\rho_w}{\mu_w d} \ln \left(\frac{I_{wet}}{I_{dry}} \right) \quad (2.14)$$

where:

w	= moisture content	[kg/m ³]
ρ_w	= density of water	[1000 kg/m ³]
μ_w	= attenuation coefficient of water	[1/m]
d	= thickness of the specimen	[m]
I_{wet}	= attenuated intensity of the wet specimen	[keV]
I_{dry}	= attenuated intensity of the dry specimen	[keV]

This means that the moisture content at each time step is determined by logarithmically subtracting the reference image from the image of the wet specimen at that time. The moisture content profiles are obtained by plotting the moisture content against the distance for each time step.

Subsequently the liquid water diffusivity is determined from the moisture content profiles. This is done using the Boltzmann transformation method (Carmeliet et al., 2004, Crank, 1989). As a first step the Boltzmann variable λ is introduced.

$$\lambda = \frac{x}{\sqrt{t}} \quad (2.15)$$

where:

λ	= Boltzmann variable	[m/s ^{1/2}]
x	= distance	[m]
t	= time	[s]

2. Experimental research

By means of the Boltzmann transformation a new curve is obtained. The moisture content is now plotted against λ . The separate curves coincide and form one single curve. This is called the w - λ profile. Boltzmann showed that the liquid water diffusivity is expressed by:

$$D_l(w) = -\frac{1}{2} \frac{\int_{w_0}^w \lambda du}{\partial w / \partial \lambda} \quad (2.16)$$

where:

$$D(w) = \text{diffusivity} \quad [\text{m}^2/\text{s}]$$

The liquid permeability is then given by:

$$K(p_c) = D(w)C \quad (2.17)$$

where:

$$K(p_c) = \text{liquid permeability} \quad [\text{s}]$$

and:

$$C = \left| \frac{\partial w}{\partial p_c} \right| \quad (2.18)$$

where:

$$C = \text{derivative of moisture retention curve} \quad [\text{kg}/\text{m}^3 \text{ Pa}]$$

$D(w)$ is converted to $D(p_c)$ by means of the moisture retention curve, since the moisture retention curve presents w as function of p_c .

Results

In figure 2.45 the attenuation is plotted against the thickness of the water layer. A linear fit is plotted as well. The slope of the linear fit represents the attenuation coefficient of water.

2. Experimental research

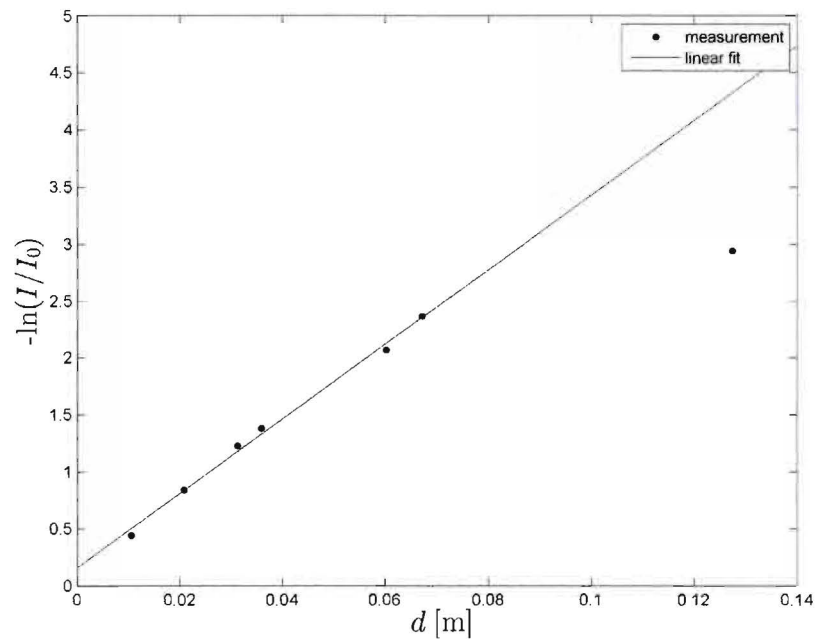


Figure 2.45: Attenuation of water against the thickness of the water layer.

As can be seen from figure 2.45, the measurement data show a linear trend except for the last measurement point. This deviation is probably due to measurement error.

Figure 2.46 shows images of the test specimen during the experiment taken at different time steps. The moisture front migrates towards the top of the specimen as time increases.

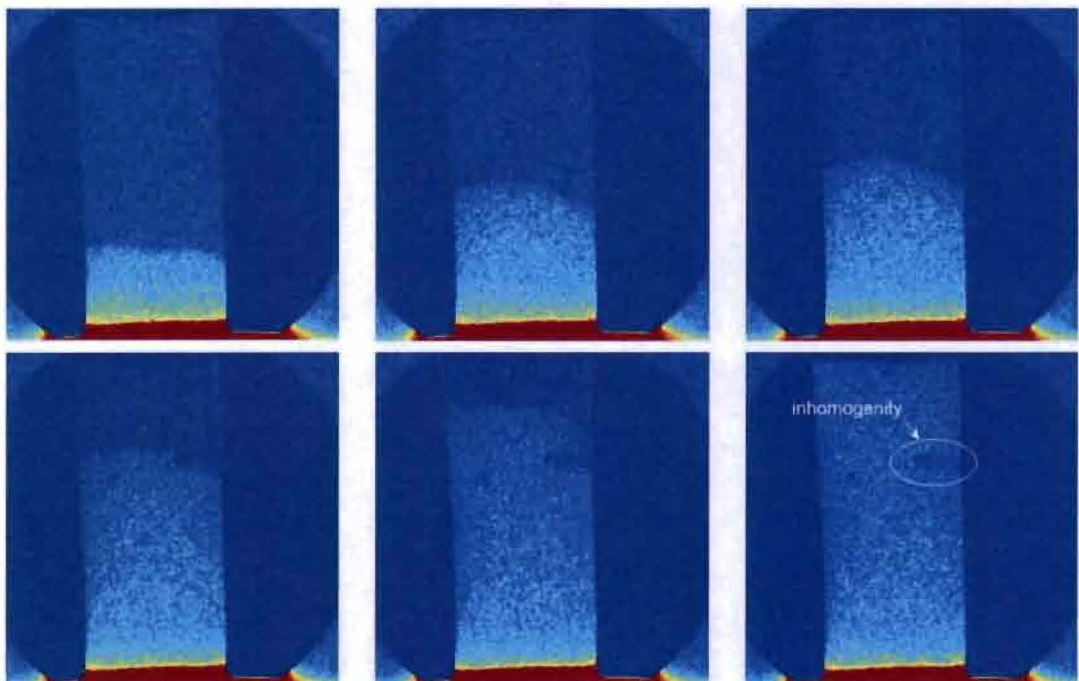


Figure 2.46: Migrating moisture front in time for BHP. The images are taken at $t=2$, $t=6$, $t=8$, $t=14$, $t=20$ and $t=30$ min respectively.

2. Experimental research

In figure 2.47 the moisture content profiles of both types of brick are presented. This figures show the moving moisture front in time as well.

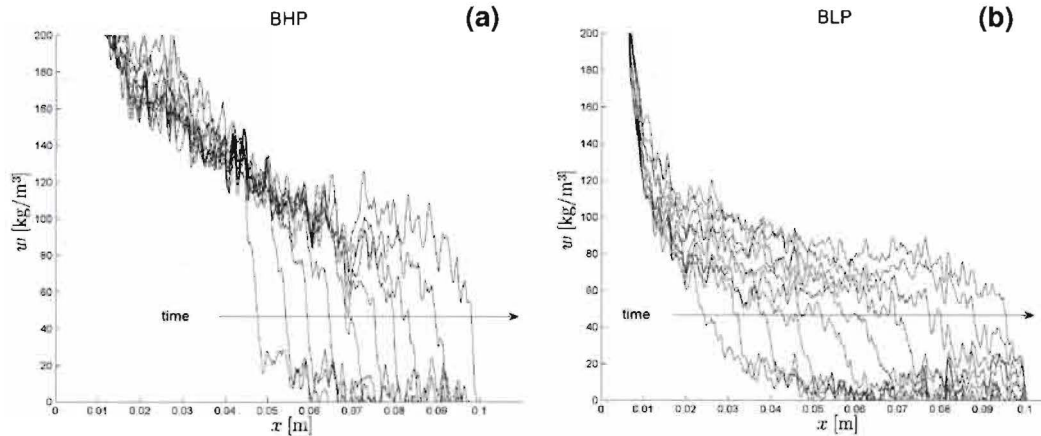


Figure 2.47: Moisture content profiles of (a) BHP and (b) BLP.

Figure 2.48 shows the Boltzmann transformed data. The moisture content is now plotted against the Boltzmann variable λ . As depicted in the figure, the separate curves presented in figure 2.47 coincide to one single curve. However, there is a wide range of scatter. This is partly due to the small scale heterogeneity of the bricks, as indicated in figure 2.46, which means that the material locally and to some extent shows structural variations. The red line represents a function fit through the measurement data.

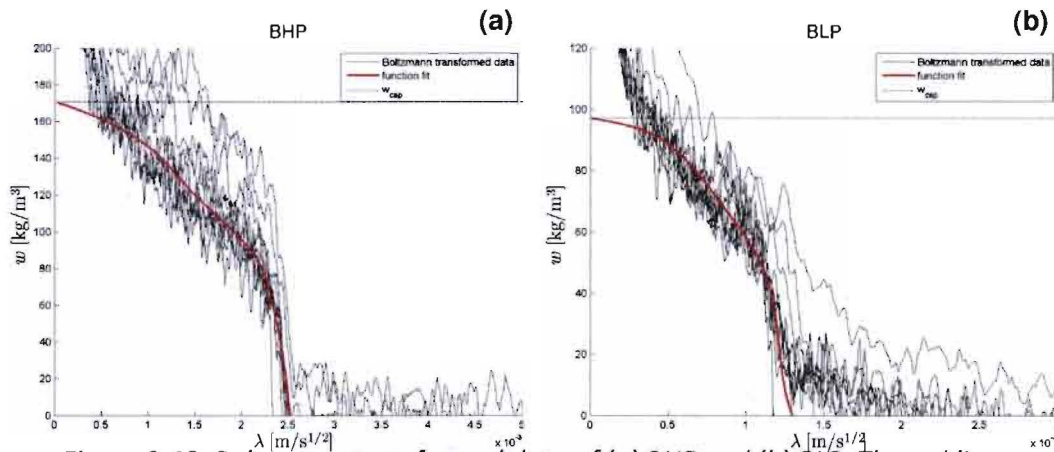


Figure 2.48: Boltzmann transformed data of (a) BHP and (b) BLP. The red line represents a function fit of the data.

It should be remarked that a different attenuation coefficient is used for the BLP brick. This is done in order to obtain curves that agree with physics (i.e. the bend where the moisture content rises to exceedingly high values should be at capillary moisture content). This is assumed to be plausible because the possibility exists that the properties of water present in the brick deviate from the properties of pure water. Molecules can dissolve which could lead to additional X-ray scattering. This is

2. Experimental research

a limitation of the X-ray method and a possible calibration method is to determine the final weight of the test samples.

In figure 2.49 the diffusivity as a function of the moisture content is given.

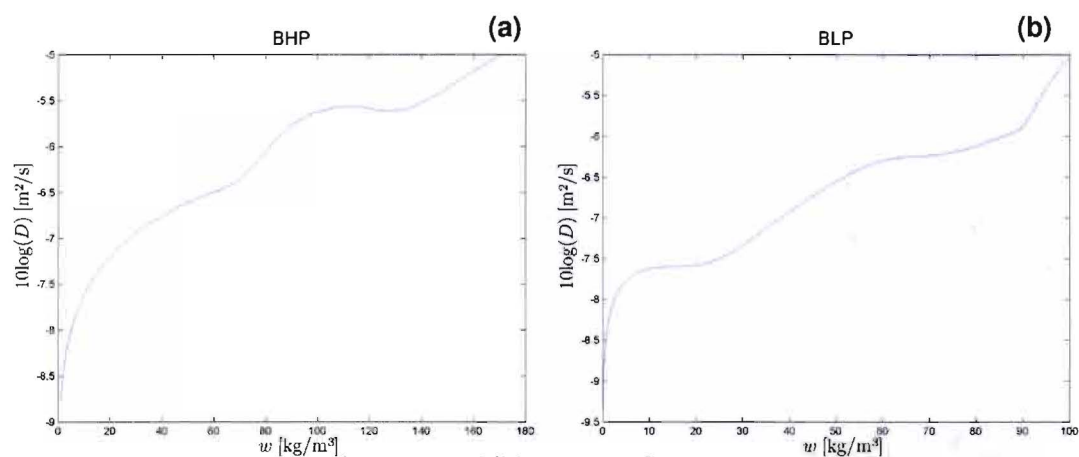


Figure 2.49: Diffusivity of (a) BHP and (b) BLP as a function of the moisture content.

After passing through all intermediate stages, eventually the liquid permeability is obtained. Figure 2.50 and 2.51 present the permeability as a function of the capillary pressure. The liquid permeability is used for the simulations.

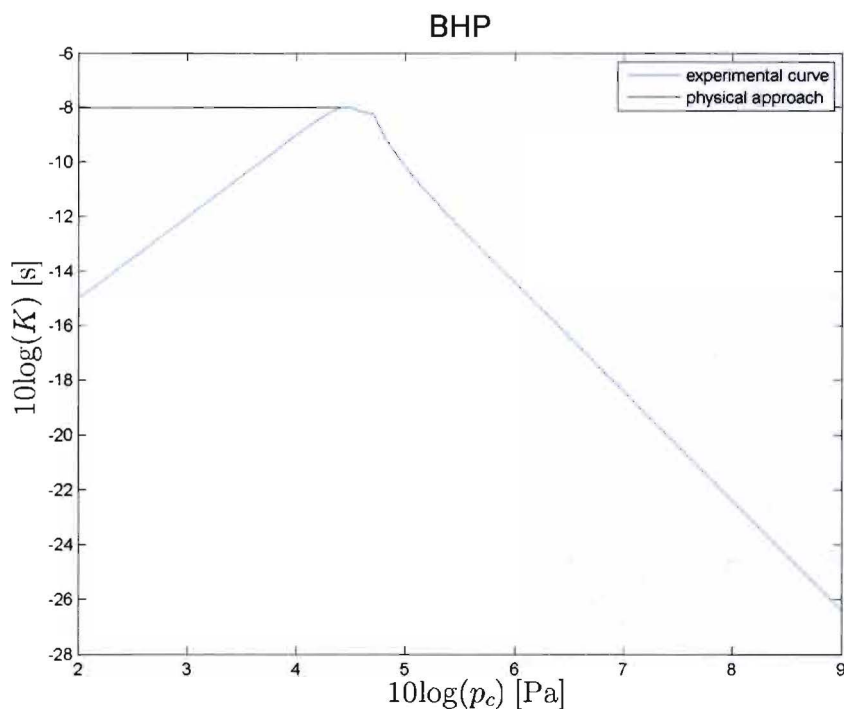


Figure 2.50: Permeability of BHP as a function of the capillary pressure.

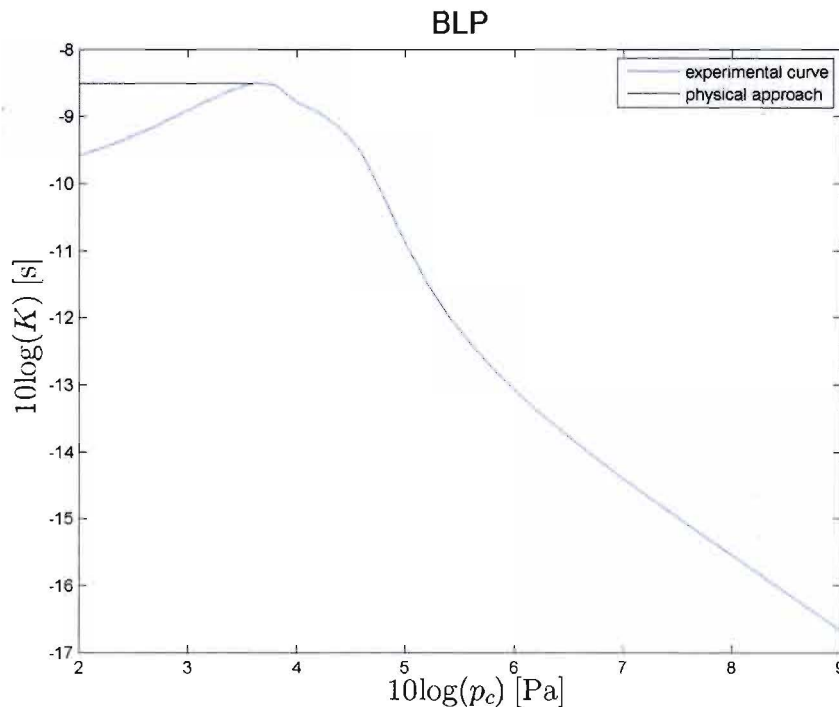


Figure 2.51: Permeability of BLP as a function of the capillary pressure.

Note that for the experimental curve in figures 2.50 and 2.51 the permeability decreases at lower capillary pressure. This decrease is physically impossible however and is related to the uncertainty of the moisture retention curve at low capillary pressure (Carmeliet et al., 2004). Therefore the permeability is corrected by extending the maximum permeability for lower capillary pressure (Carmeliet et al., 2004).

2.3.5 Determination of the water storage on three types of glass

With this experiment the order of magnitude of rainfall interception of non-porous building materials is obtained. In order to determine the difference in rainfall interception between several non-porous building materials, three material samples are used:

- Normal float glass
- Teflon, which can be representative for glass with a hydrophobic coating
- Glass with hydrophilic coating (Bioclean®)

Apparatus

The following equipment is used for this experiment:

- Balance, capable of weighing a test specimen to an accuracy of $\pm 0,1\%$ of the mass of the specimen.
- Timer.

2. Experimental research

- Test setup with a suction cup and counterweight in order to keep the test panel in place. The setup is schematically depicted in figure 2.52.
- Water spraying device.
- Acetone (CH_3COCH_3) and Ethanol ($\text{CH}_3\text{CH}_2\text{OH}$) for cleaning the test panel.
- Clean room tissue to dry the test panel.

Test procedure

Date and duration of the test:

Start: 07-05-2010 ; 15.00 h

End: 07-05-2010 ; 21.00 h

A test setup was designed to directly obtain the mass increase of the test panels due to water spraying. Figure 2.52 schematically shows this setup. The test setup is designed in such way that only water falling onto the test panel is weighed. The surrounding construction, installed to collect droplets that are not sprayed onto the test panel, is detached from the balance.

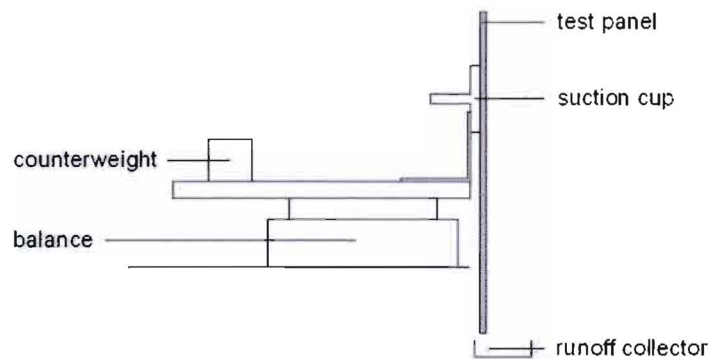


Figure 2.52: Test setup of the experiment.

Before starting the experiment the test panels are carefully cleaned with Acetone and Ethanol and subsequently rinsed with demi-water. Between spraying cycles the test panels are dried with clean room tissue.

Each test panel is subjected to five spraying cycles. In each cycle demi-water is sprayed for 30 seconds, so that a certain amount of runoff occurred. This way the impinging raindrop diameter is eliminated as a parameter of influence (Blocken et al., 2006). 30 seconds after stopping the water supply the mass increase of the test panels is noted.

Data processing

For each test panel the mass change due to water spraying is obtained. From this the water storage of each material can be calculated from:

$$S = \frac{\Delta m}{A} \quad (2.19)$$

where:

2. Experimental research

S	= storage	[kg/m ²]
Δm	= mass change of the test panel	[kg]
A	= area of the test panel	[m ²]

Results

Table 2.13 presents the result of the experiments.

Table 2.13: mass change, area and storage of the material samples.

	Float glass	Hydrophobic glass	Hydrophilic glass
Average mass change [kg]	0.00485	0.006556	0.005508
Area [m²]	0.16005	0.0799455	0.16005
Storage [kg/m²]	3.03E-02	8.20E-02	3.44E-02

The storage is almost the same for float glass and hydrophilic glass. Possibly somewhat unexpected, though already shown by Blocken et al. (2006), the hydrophobic glass holds the largest amount of water despite its water repellent characteristics. This is most likely due to the fact that the surface tension for water droplets on the test panel is higher because of the hydrophobic character of the material (Tanford., 1979). Therefore single droplets arise instead of a water film. The contact angle of single droplets with the material is higher than for droplets that are spread out, as shown in figure 2.53. A high contact angle therefore means a low contact area and for this reason the hydrophobic glass is capable of holding more water than normal glass.



Figure 2.53: Contact angle of different shaped droplets (Ramehart.com).

Note that the determined value is not the maximum storage, since the maximum mass change is obtained directly after stopping the water supply. However, the results of the water storage for the three material samples can be fairly compared this way and the order of magnitude of rainfall interception by non-porous building materials is indeed determined.

2.4 Conclusion

In this chapter both full-scale measurements as well as laboratory experiments have been reported. Several material samples were considered in order to gain insight into the difference in rainfall interception between a brick with high porosity and a brick with low porosity. BHP showed a RI of 100% for the considered measurement

2. Experimental research

period. BLP yielded a minimum RI of 76.6% for the considered measurement period. Furthermore the difference in rainfall interception between porous and non-porous building materials has been demonstrated. The results of the full-scale measurements will be used for the validation of the numerical model. During the laboratory experiments several material properties regarding moisture of the two types of brick have been determined. These material properties gain insight into the moisture behavior of the materials and will be used as input parameters for the simulations. An elaborate description of the numerical part of this study is given in chapter 3.

Chapter 3

Numerical simulations

From the previously discussed measurements a certain level of knowledge is gained about rainfall interception by porous and non-porous building materials. In this chapter the numerical part of the study is presented. First the mathematical model and its physical background are explained. The model aims to adequately predict the amount of rainfall interception by two types of brick. The experimental results are used for validation of the model. Subsequently the boundary conditions of the model are adapted and an analysis of climate dependent parameters such as rainfall, temperature and relative humidity is performed in which the influence of climate on rainfall interception is studied.

3.1 Model

In this paragraph the mathematical model is discussed. First the essential physical background is given. Subsequently the numerical implementation of the model is considered.

3.1.1 Physical background

In the numerical part of this research simulations are carried out for the two types of brick. For modeling of transport phenomena in porous media the continuum approach is commonly used (Bear et al., 1990).

In this research the response of the facade to wind-driven rain (WDR) is studied. To gain insight into this response, one-dimensional heat and moisture transfer simulations are performed. The numerical model consists of balance equations for mass and energy in differential form. Since this study is focused on rainfall interception, air transfer is neglected. The equations are given by (Janssen et al., 2007a):

$$\frac{\partial(w_l + w_v)}{\partial t} = -\nabla(g_l + g_v) \quad (3.1)$$

$$\underbrace{(c_0\rho_0 + c_l w_l + c_v w_v)}_1 \frac{\partial T}{\partial t} + \underbrace{(c_l T)}_2 \frac{\partial w_l}{\partial t} + \underbrace{(c_v T + L_v)}_3 \frac{\partial w_v}{\partial t} = -\nabla(\underbrace{q_{cond} + q_{conv}}_4) \quad (3.2)$$

where:

w	= moisture content	[kg/m ³]
t	= time coordinate	[s]
∇	= divergence operator	[-]
g	= moisture flow	[kg/m ² s]
c	= specific heat capacity	[J/kg K]
ρ_0	= dry density of the material	[kg/m ³]
T	= temperature	[K]
L_v	= enthalpy of evaporation	[J/kg]
q_{cond}	= heat flow rate by conduction	[W/m ²]
q_{conv}	= heat flow rate by convection	[W/m ²]

and where the subscripts l , v and 0 refer to *liquid*, *vapor* and *solid* respectively.

Equation (3.1) represents the conservation of mass. In words this conservation law is described as follows. The change of the amount of moisture in the material in time, on the left hand side, is caused by inflow or outflow of moisture, on the right hand side. Moisture can be present in both liquid and gas phase.

Equation (3.2) describes the conservation of energy in which part 1 represents the change in time of the amount of energy stored as sensible heat in the different components (solid, liquid and vapor). In part 2 and 3 the energy change in time due to a change of the amount of moisture is described. This can either be caused by condensation or evaporation. This part of the energy balance describes the energy interaction due to these phase changing processes, in which part 2 represents the liquid contribution and part 3 represents the vapor contribution. The latent heat associated with a phase change is governed by L_v . Part 4 of the equation gives the energy change due to heat flow by conduction and convection.

To solve the mass and energy balance equations a number of boundary conditions and initial values need to be specified. The boundary conditions describe the situation at the surfaces of the material. They can be specified either as a fixed value or a flux and can change over time. The initial values give the starting conditions of all variables in the materials.

3.1.2 Numerical implementation

After the description of the physical model in the previous paragraph, the next step is the numerical implementation of the model. The physical model has been implemented by Janssen et al. (2007a) in HAMFEM, which is an abbreviation for *Heat Air Moisture Finite Element Method*.

General parameters

At first some general parameters are specified. The orientation of the building and the position on the building facade are given. This is taken into account for the calculation of the wind-driven rain, the heat and moisture transfer coefficients and the solar radiation, which will be further discussed in the description of the boundary conditions. Furthermore the start time, end time and time step of the simulation are specified. Next the number of dimensions of the simulation is defined. In this study one-dimensional simulations are performed. Finally the mesh is specified, in which the thickness of the wall and the division into discrete nodes is given.

Material properties

In HAMFEM various materials are predefined. However, new material data can be added. In order to do this the following material properties regarding both heat and moisture need to be specified in the material library:

- Density
- Thermal capacity
- Thermal conductivity
- Capillary moisture content
- Moisture retention curve
- Vapor diffusion coefficient
- Liquid permeability

For most properties analytical functions have to be provided. For the purpose of this study the experimentally determined material properties for BHP and BLP (density, capillary moisture content, moisture retention curve and liquid permeability, as described in section 2.3) are added.

Boundary conditions

In this part the atmospheric boundary conditions need to be specified. For this purpose a climate file is used in which the following parameters are listed:

- Temperature
- Relative humidity
- Rainfall intensity
- Direct and diffuse solar radiation
- Wind speed
- Wind direction

The indoor temperature and relative humidity are specified as well.

The parameters listed in the climate file are the boundary conditions or are used to determine the boundary conditions. The boundary conditions are briefly described below.

Wind-driven rain

The amount of rain arriving on the building facade is determined by means of the catch ratio, which is defined as (Blocken et al., 2007):

$$\eta = \frac{R_{WDR}}{R_h} \quad (3.3)$$

where:

η	= catch ratio	[-]
R_{WDR}	= WDR intensity on the building	[mm/h]
R_h	= horizontal rainfall intensity	[mm/h]

Catch ratio charts were constructed by Blocken et al. (2007) in which the catch ratio is given as a function of the reference wind speed and horizontal rainfall intensity. Moreover each chart represents a certain position on the building facade and a certain wind direction. With these catch ratio charts meteorological data of reference wind speed, horizontal rainfall intensity and wind direction is easily converted into the corresponding WDR distribution on the building facade (Blocken et al., 2007).

Convective heat exchange

For the determination of the convective heat exchange of a material, the convective heat transfer coefficient is needed. The convective heat transfer coefficient is derived from the Sharples equation. Sharples (1984) experimentally obtained relationships between the convective heat transfer coefficient and wind speed for 4 positions on an 18 storey building in the U.K. The equation found for the 18th floor at the edge is implemented in HAMFEM, in which the heat transfer coefficient is given by:

$$h_c = 1.7V_{loc} + 5.1 \quad (3.4)$$

where:

h_c	= convective heat transfer coefficient	[W/m ² K]
V_{loc}	= local wind speed at the facade	[m/s]

Vapor exchange

Similarly to the heat exchange, vapor exchange is described by means of the moisture transfer coefficient. The moisture transfer coefficient is derived from the Sharples equation as well. For this the Lewis analogy is used, in which the assumption is made that similarity exists between the thermal and hygric boundary layer near the surface (Janssen et al., 2007b). The moisture transfer coefficient is then described by (Janssen et al., 2007b):

$$\beta = 7.7 \cdot 10^{-9} h_c \quad (3.5)$$

where:

β	= moisture transfer coefficient	[s/m]
h_c	= convective heat transfer coefficient	[W/m ² K]

3. Numerical research

Since accurate and reliable data are lacking, above-mentioned empirical relations and analogies are used to determine the heat transfer coefficient and moisture transfer coefficient respectively (Janssen et al., 2007a). There is a large uncertainty in these values however and further research is needed (Janssen et al., 2007a,b).

Long wave radiation

This describes the long wave radiative exchange between the surface and its surroundings, based on the emissivity and temperature differences (Janssen et al., 2007a).

Short wave radiation

The amount of solar radiation that falls onto the facade is derived from the direct and diffuse solar radiation, specified in the climate file (Janssen et al., 2007a).

Latent and sensible heat transfer by vapor exchange

Due to in and outflow of vapor the amount of energy stored in the material changes (Janssen et al., 2007a).

Sensible heat transfer by rain

When rain falls onto the facade heat exchange takes place between the rain and the facade (Janssen et al., 2007a).

The calculation of the above-mentioned boundary conditions is described by Janssen et al. (2007a). The boundary conditions result in the following equations. The heat fluxes at the exterior and interior surfaces of the facade are given by (Blocken et al., 2007):

$$q_e = h(T_e - T_s) + g_v L_v + S + g_l c T_{WDR} \quad (3.6)$$

$$q_i = h(T_i - T_s) + g_v L_v \quad (3.7)$$

with the radiative heat exchange described by (Janssen et al., 2007a):

$$S = \kappa(S_{dir} + S_{dif}) + \sigma E \left(F_g (T_g^4 - T_s^4) + F_{sky} (T_{sky}^4 - T_s^4) \right) \quad (3.8)$$

where:

q	= heat flux at exterior boundary	[W/m ²]
h	= heat transfer coefficient	[W/m ² K]
T	= temperature	[K]
S	= radiative heat exchange	[W/m ²]
g_v	= vapor flow	[kg/m ² s]
L_v	= enthalpy of evaporation	[J/kg]
c	= specific heat capacity	[J/kg K]
κ	= solar absorption coefficient	[-]
S_{dir}	= direct solar radiation	[W/m ²]
S_{dif}	= diffuse solar radiation	[W/m ²]

3. Numerical research

σ	= Stefan- Boltzmann constant	[W/m ² K ⁴]
ε	= long-wave emissivity of surface	[-]
F	= view factor	[-]

and with subscripts:

i	= interior
e	= exterior
s	= surface
g	= ground
WDR	= wind-driven rain

The first term of equations (3.6) and (3.7) covers for the convective heat exchange. In the second term the latent heat transfer is accounted for. The third term in equation (3.7) describes both short and long-wave radiation. The last term in equation (3.7) contains the sensible heat transfer by rain (Blocken et al., 2007). The moisture fluxes for both liquid as vapor at the exterior boundary are given by (Blocken et al., 2007):

$$g_v = \beta(p_o - p_s) \quad (3.9)$$

$$g_l = \max\left(R_{WDR}, K \frac{\partial p_c}{\partial n}\right) \quad (3.10)$$

where:

g_v	= vapor flow	[kg/m ² s]
β	= vapor transfer coefficient	[s/m]
p_o	= vapor pressure in the air	[Pa]
p_s	= vapor pressure at the surface	[Pa]
g_l	= liquid flow	[kg/m ² s]
R_{WDR}	= wind-driven rain intensity	[mm/h]
K	= moisture permeability	[s]

and where:

$\frac{\partial p_c}{\partial n}$ represents the derivative of the capillary pressure in the orthogonal direction of the surface. In HAMFEM the moisture content in the material is limited to the capillary moisture content. This means that the liquid flux due to WDR is equal to the WDR intensity until the capillary moisture content is reached at the exterior surface.

Then the liquid inflow reduces to $K \left(\frac{\partial p_c}{\partial n} \right)$ and runoff can occur (Blocken et al.,

2007).

The non-linear transfer equations given in section 3.1.1 together with the imposed boundary conditions are solved for discrete positions in the material. The result is the moisture content in the material per time span which is converted to the mass change of the material in time.

3.2 Model validation

In this paragraph the validation of the model is discussed. For this purpose the experimental results are used.

3.2.1 Test case

The experimental results are used to set up a test case for validation of the numerical model. A period of 12 days, from February 24 until March 8 2010, is selected for the test case. In this period two major rain events occurred. The first rain event took place on February 28. It was raining all day, with the highest peak in rainfall intensity in the late afternoon. This day even flooding occurred in Southern Europe (knmi.nl). The second rain event was on March 5. Especially in the evening and at night higher rainfall intensities were observed. Both rain events stemmed from stratiform clouds (knmi.nl). Stratiform clouds arise in a stable atmosphere due to extensive cooling and slow but persistent condensation processes (Blocken et al., 2007). Figure 3.1 depicts the measured WDR intensity during this test period.

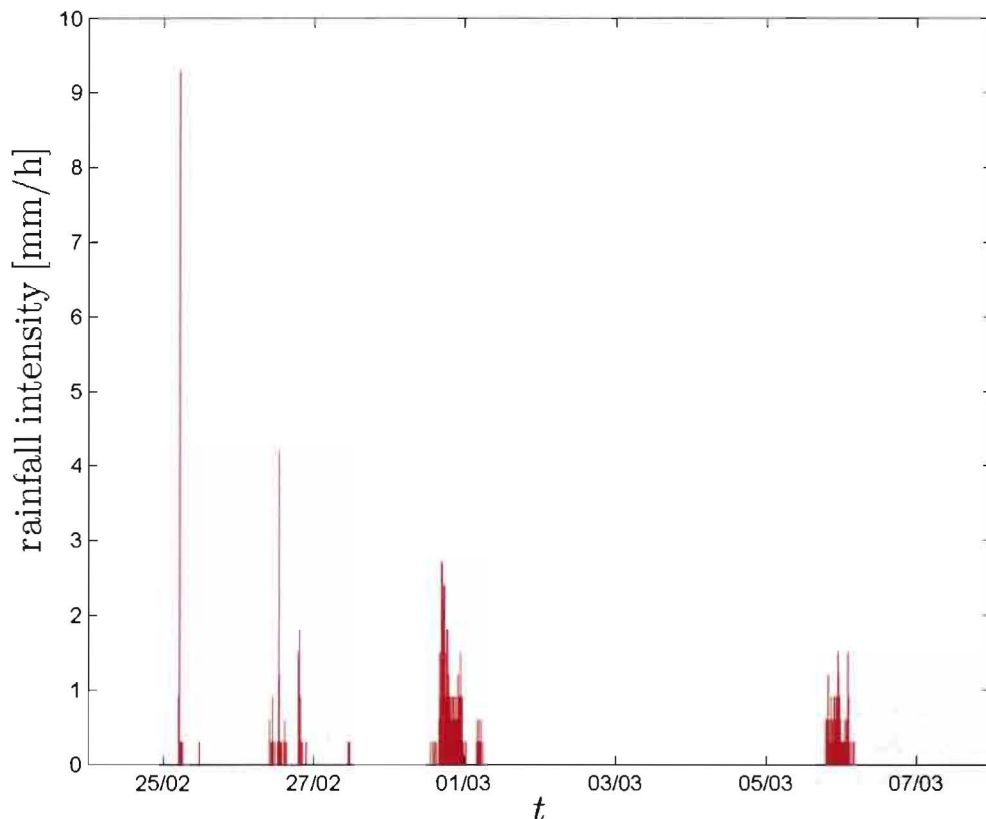


Figure 3.1: WDR intensity during the considered test period.

3. Numerical research

From this period the micro-meteorological data gathered during the full-scale measurements is used to construct a climate file. The temporal resolution of the climate file is 10 minutes, which is an averaged value of the higher resolution measurement data.

Some adjustments are made to the boundary conditions. In this case the WDR is directly obtained from measurements, which means that the catch ratio charts are not used. Besides this, the total amount of solar radiation on the facade is directly measured instead of obtained from the direct and diffuse solar radiation. Furthermore the local wind speed on the facade is measured instead of derived from the reference wind speed at 10 meters height.

The material properties determined with the laboratory experiments (section 2.3) are implemented in HAMFEM, yielding two new materials in the material library. Material properties that are not experimentally determined (thermal capacity, thermal conductivity and vapor diffusion coefficient) are found in literature (Hens, 2003) or adopted from the ceramic brick already present in the material library.

The boundary conditions are similar for both types of brick. Only the material properties differ, since different materials are used. Main settings for the simulations are found in table 3.1. Further settings are included in Appendix E.

Table 3.1: Main settings for the simulations.

		Brick with high porosity	Brick with low porosity
Initial values	T	274.7 K	274.7 K
	Pc	$3.16 \cdot 10^5$ Pa	$3.16 \cdot 10^6$ Pa
Boundary conditions	h	$1.7V_{loc}+5.1$	$1.7V_{loc}+5.1$
		Vloc specified in climate file	Vloc specified in climate file
	β	$7.7 \cdot 10^9$ h	$7.7 \cdot 10^9$ h

Subsequently the simulations are performed and a comparison is made between the mass change in time of the test samples obtained from the full-scale measurements and the mass change obtained from the simulations to validate the correct implementation of the model.

3.2.2 Comparison experimental and numerical results

In this paragraph the numerical results are compared to the experimental results in order to assess the validity of the model in modeling the experimental conditions and predicting the amount of rainfall interception. Figure 3.2 and 3.3 present the results for the brick with high porosity (BHP) and the brick with low porosity (BLP) respectively. In Figure 3.4 the results for both types of brick are shown together.

Since the mass change of the test samples is due to rainfall, this value is equal to the amount of rainfall interception (RI) by that material. Immediate evaporation during rainfall is not included however, and therefore RI may be slightly underestimated. Negative values for RI are a result of evaporation of moisture already present in the material at the beginning of the test period.

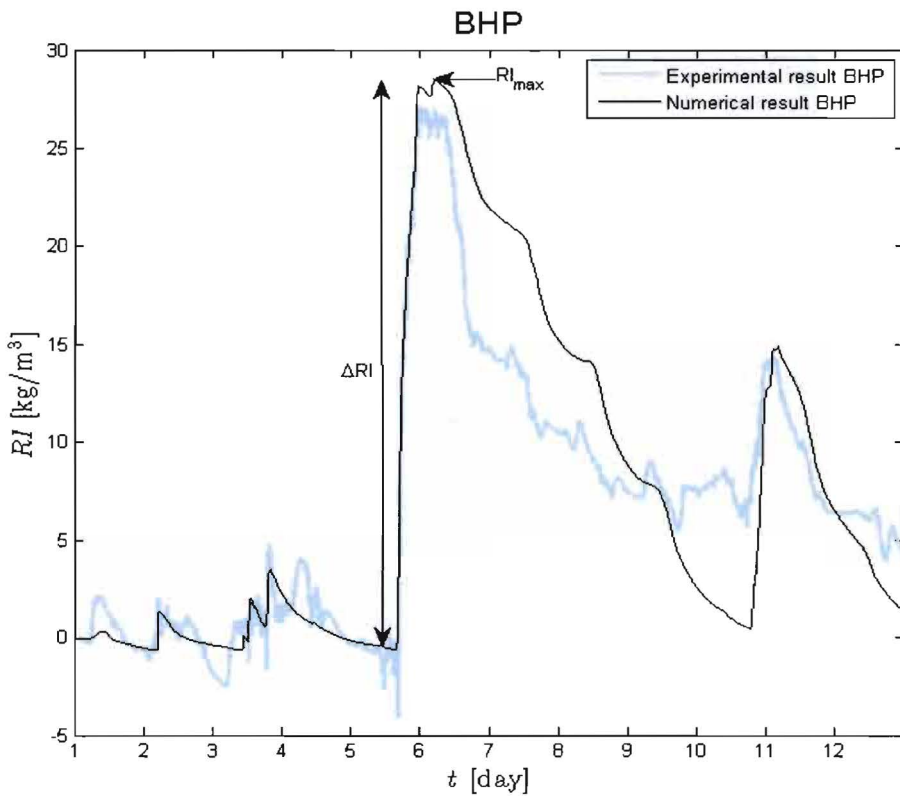


Figure 3.2: Comparison of the experimental and numerical results for BHP.

Figure 3.2 shows that the experimental and numerical results for BHP show the same trend. However, there are two main points in which the results deviate.

Firstly the maximum value of rainfall interception of the first rain event is overestimated by the numerical model. The difference in RI between the value at the beginning of the rain event and the maximum value for RI during this rain event (ΔRI) shows fairly good agreement for both curves. For the second rain event ΔRI by the measurements is much lower than ΔRI given by the simulations. There are several errors associated with WDR measurement (Blocken et al., 2006). Most of them, like the evaporation of adhesion water, contain an underestimation of the actual WDR however. Furthermore not all raindrops falling onto a facade are actually absorbed by the facade. It is also possible that drops splash or bounce off the facade (Blocken et al., 2006, Abuku et al., 2009). This effect is underestimated by the WDR gauges and therefore the amount of WDR available for absorption is overestimated (Abuku et al., 2009). Besides this in HAM modeling discrete and random impingement of raindrops is spatially and temporally averaged into an average WDR flux, while in reality individual drops fall onto the facade (Abuku et al., 2009). This is also a possible explanation for the overestimation of RI. These effects concern both rain events however, so this is not the cause of the differences only observed during the second rain event. It is not totally clear what the reason is for this deviation between the experimental and numerical results.

The second observation is that the curve of the measurement results first drops rapidly after a rain event and then gradually further decreases while the numerical results show a gradually decline from the beginning. Furthermore the slope of this

3. Numerical research

part of the curve is steeper for the numerical results, which means that the model predicts a higher evaporation rate than the measurements. This results in a lower value of RI at the beginning of the next rain event.

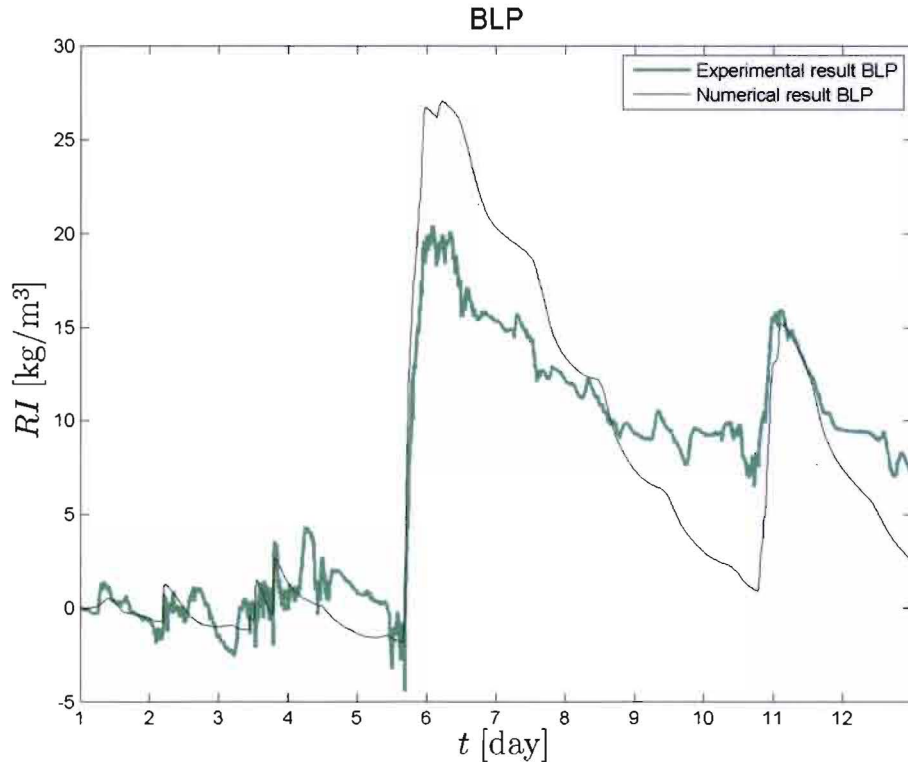


Figure 3.3: Comparison of the experimental and numerical results for BLP.

In figure 3.3 the same trend as described above is shown. However, in this case the maximum rainfall interception is even more overestimated by the numerical model. The reason for this is that in the simulation, in contrary to the measurements, no runoff occurs and therefore the maximum RI for the numerical results is much higher than the maximum RI for the experimental results for this type of brick.

When the brick is capillary saturated or when the rainfall intensity exceeds the maximum absorption rate of the brick, runoff can occur. As shown in figure 3.3 the capillary moisture content of the brick (97 kg/m^3) is not reached, so the brick is not capillary saturated. This means that the absorption rate of the brick was lower than the rainfall intensity on the facade at that time. This implies that the exterior surface is locally saturated and therefore runoff occurs. The model fails to predict this effect however. This is possibly due to incorrect values of material parameters. The liquid permeability is a measure for the ease with which the material transports fluid. For the determination of this parameter the moisture retention curve is used as well. The determination processes of both parameters contain many steps with which some errors may be associated because manually function fitting is included (section 2.3.3 and 2.3.4). The results however show a good agreement with solutions found in literature though (Roels et al., 2006, Carmeliet et al., 2004). It is therefore not totally clear why the numerical model fails to predict runoff in this case.

3. Numerical research

Table 3.2 presents some values of the deviation between the experimental and numerical results. First the difference between both curves is determined for every time step and integrated for the whole test period. This is divided by the integrated value of the measurement curve and gives the mean deviation of the numerical results from the experimental results (dev_{mean}).

Furthermore the maximum deviation between the numerical and experimental results is determined (dev_{max}). The difference in maximum RI for both rain events (dev_{event}) is considered as well. Note that the measurement curves start lower at the beginning of the first rain event and therefore have a lower peak value than the simulation curves. ΔRI is therefore predicted more accurately for the first event, however, for the second event the deviation is even larger. This deviation is given by $dev_{\Delta RI_event}$. For all calculations the measurement results are taken as being true and thus set to 100%.

Table 3.2: Deviation between the numerical and experimental results for both types of brick.

	BHP	BLP
dev_{mean}	35%	37%
dev_{max}	59%	66%
dev_{event1}	4%	22%
dev_{event2}	3%	5%
$dev_{\Delta RI_event1}$	7%	13%
$dev_{\Delta RI_event2}$	68%	54%

Figure 3.4 shows that both curves of the numerical results show little difference even though different types of brick, with different material properties are considered. Because the model fails to predict runoff, both bricks absorb more or less the same amount of water and little difference is shown in ΔRI for both rain events. For the evaporation process the numerical results show the same trend as the experimental results: the curve for BHP decreases slightly faster than the curve for BLP.

3. Numerical research

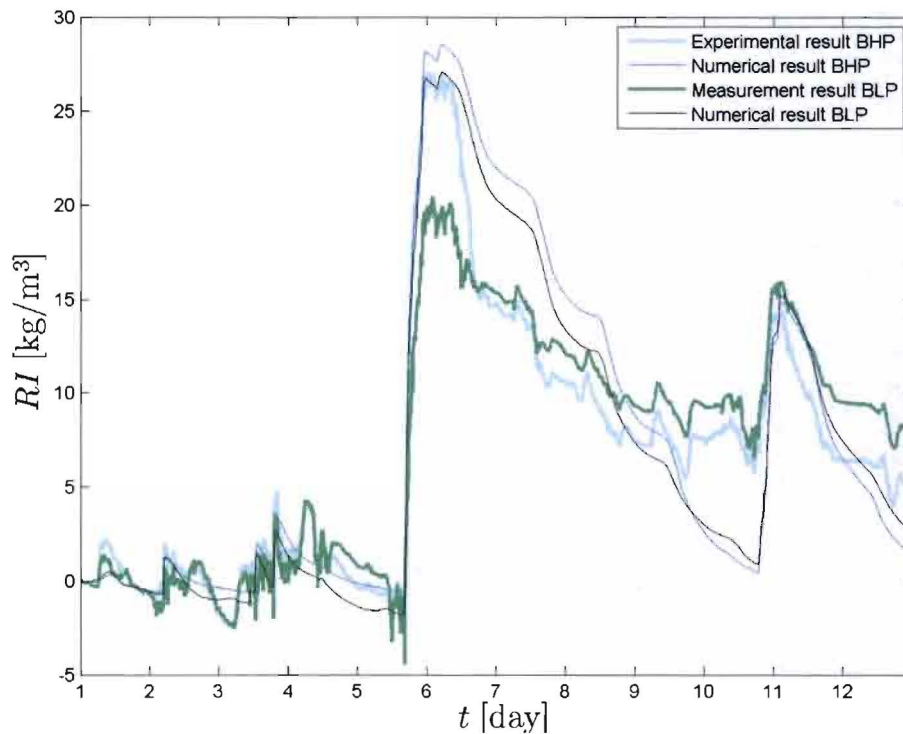


Figure 3.4: Comparison of the experimental and numerical results for both types of brick.

Overall the numerical results show a faster evaporation than the experimental results. There are several possible reasons for this.

First of all the measurement data for solar radiation during the test period were lacking to a large extent due to measurement equipment malfunction. The available data are used and repeated for the rest of the test period. With this an error is made which can be of influence on the numerical results. The numerical model shows not to be very sensitive for solar radiation however.

Secondly the anemometer was still situated on its old position (section 2.2.3) during the test period. It was repositioned because it was assumed that the wind pattern around the anemometer could be disturbed by the runoff reservoirs. For the test period this means that possibly the measured wind speeds are higher than the actual wind speeds. This results in a higher convective heat exchange and coherent a faster drying process.

Related to this another possible reason for the faster drying process shown by the simulations is the value of the convective heat transfer coefficient. The heat transfer coefficient is derived from the Sharples equation (equation (3.4)). As shown in figure 3.5 the numerical results are very sensitive to the value of the heat transfer coefficient. Similar results are found for the other type of brick.

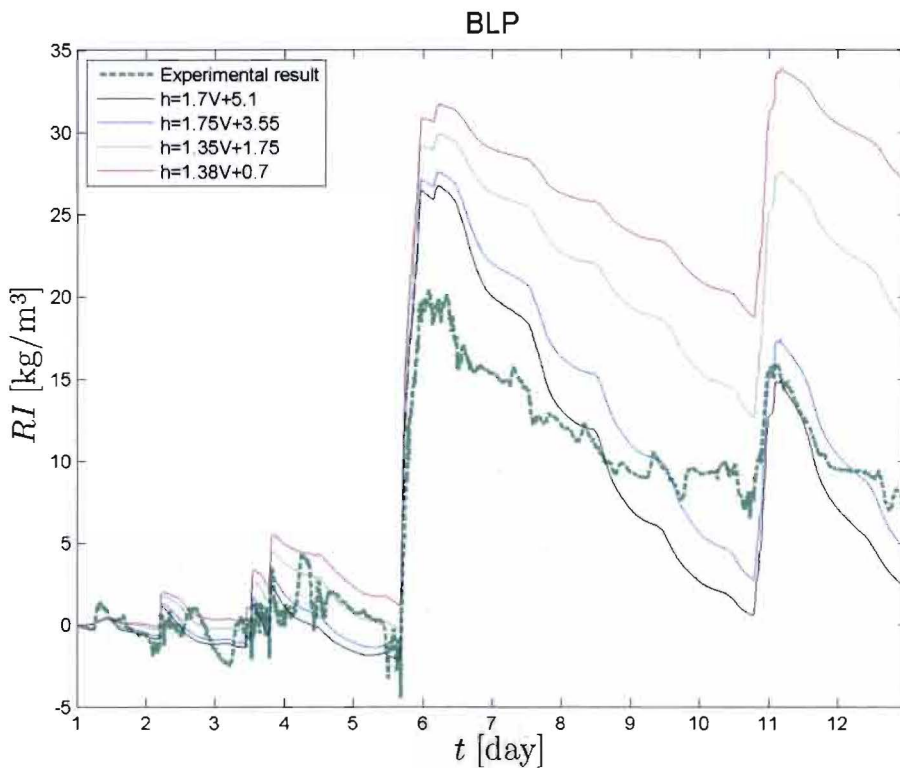


Figure 3.5: Sensitivity of the numerical model for the value of the convective heat transfer coefficient for BLP. The black line represents the original numerical result.

In this figure the numerical results for all four equations found by Sharples (1984) are depicted. The equations are obtained on a building with geometry dissimilar to the Vertigo building used in this study. However, since measurement data are lacking and equation (3.4) is shown to lie centrally amongst all other relations between the heat transfer coefficient and wind speed obtained over the years (Janssen et al., 2007), equation (3.4) is used for the simulations. However, when the value of the heat transfer coefficient is overestimated using this equation, this results in a higher convective heat exchange and again a faster evaporation process.

For the moisture transfer coefficient similar sensitivity is obtained as for the heat transfer coefficient, since this value is derived from the Sharples equation as well (equation (3.5)). Since vapor exchange is the most important moisture removal mechanism for porous building materials (Janssen et al., 2007a), the moisture transfer coefficient has a major influence on the evaporation process. This is demonstrated in previous studies (Janssen et al., 2007b, Abuku et al., 2009) by dividing the moisture transfer coefficient by 2 and multiplying it by 2. In this study the moisture transfer coefficient is therefore changed by a factor two as well. The results are presented in figure 3.6. Similar results are found for the other type of brick.

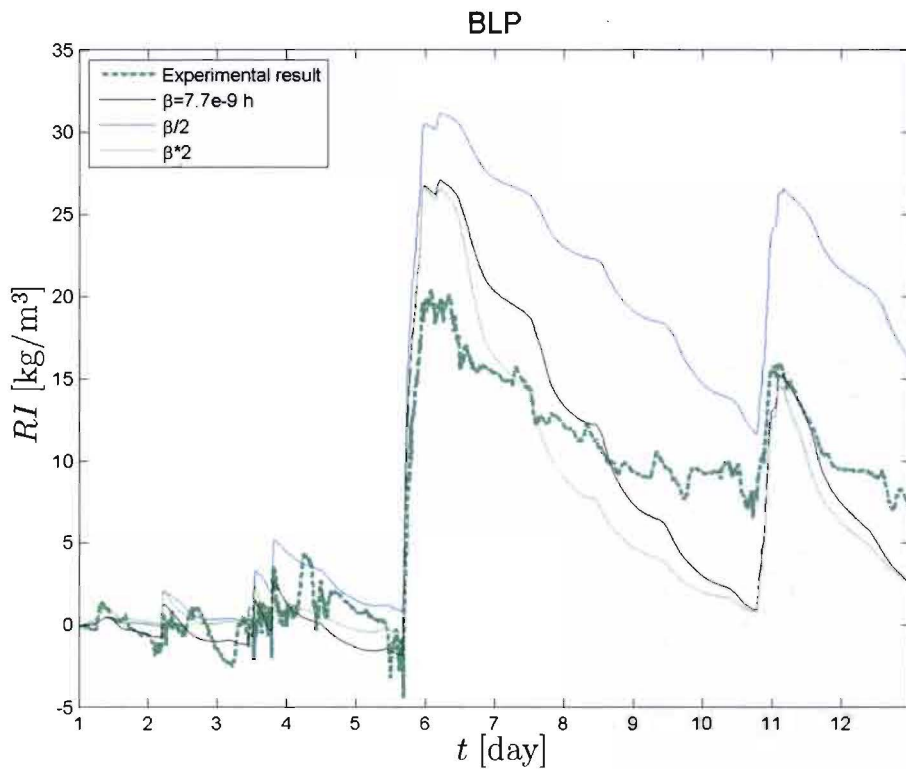


Figure 3.6: Sensitivity of the numerical model for the value of the convective moisture transfer coefficient for BLP. The black line represents the original numerical result.

Furthermore in HAMFEM hysteresis is not accounted for. Wetting and drying of porous materials results in different moisture retention curves (section 2.3.3). In HAMFEM only the wetting curve is implemented. This means that, during the drying process, for a given capillary pressure the moisture content given by the model (a) is lower than in reality (b), as shown in figure 3.7. Therefore the model predicts a faster evaporation process than in reality occurs.

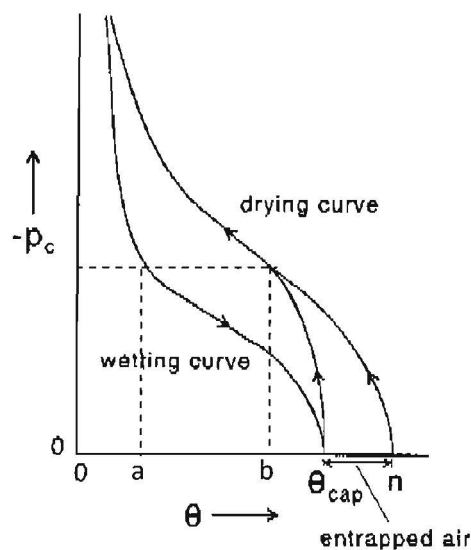


Figure 3.7: Example of wetting and drying curves (Pel., 1995).

3. Numerical research

Finally the numerical results appear to be sensitive for the initial value of the capillary pressure as presented in figure 3.8. Similar results are found for the other type of brick.

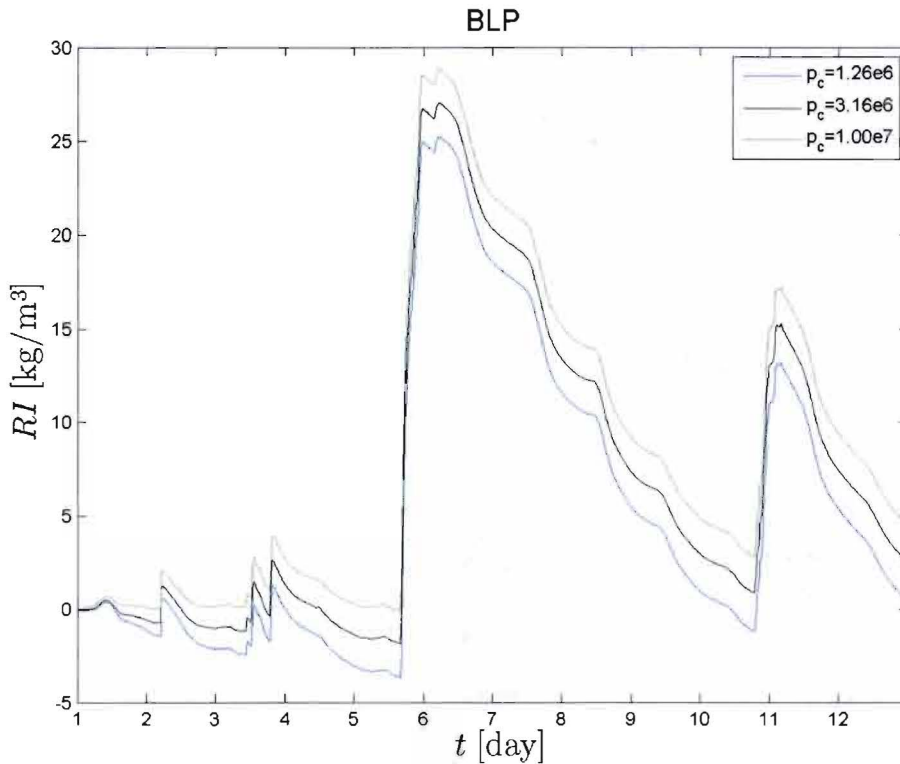


Figure 3.8: Sensitivity of the numerical model for the initial value of the capillary pressure for BLP. The black line represents the original numerical result.

To get better results, simulations should start a certain period of time before the period of interest. This way a better initialization of the model is obtained. Unfortunately for this study measurement data of the period before the test period was lacking due to measurement error which means that the simulation could not be initialized properly. To solve this problem an estimation is made of the moisture content in the material samples at the beginning of the test period, based on the weight difference of the material samples between the value at the beginning of the test period and the dry weight. This is assumed to be a plausible procedure since the material samples were oven-dry at installation. The moisture content is converted to a capillary pressure by means of the moisture retention curve (section 2.3.3). The numerical results are thus sensitive for the initial value of the capillary pressure. However, as shown in figure 3.8 this value is of little influence on the fastness of the drying process.

3.3 Climate parameter analysis

In this section the second type of simulations is described. Meteorological data of several climate groups are used to specify the boundary conditions and study the influence of climate on rainfall interception.

3.3.1 Köppen climate classification

For this analysis different climates are considered. The Köppen climate classification is a widely used climate classification system, first introduced by Wladimir Köppen in 1884. In the following years the classification was updated by Köppen himself and Rudolf Geiger. Therefore the classification is sometimes referred to as the Köppen-Geiger climate classification. According to this classification the climates on earth can be divided in five main climate groups (Strahler et al., 1984):

- A Tropical climates
- B Dry climates
- C Temperate climates
- D Continental climates
- E Polar climates

The main groups are further divided into subgroups that indicate for example whether a dry summer, a dry winter or no dry period at all is present. Figure 3.9 shows the world map of the Köppen-Geiger climate classification.

World map of Köppen-Geiger climate classification

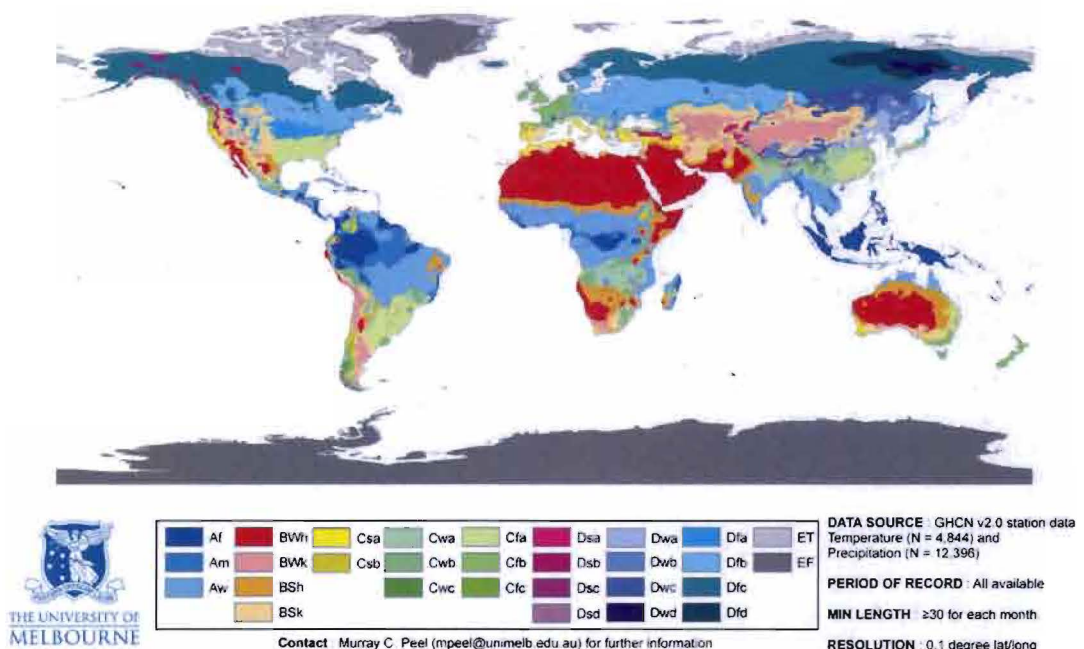


Figure 3.9: World map of the Köppen-Geiger climate classification (Wikipedia.org).

3. Numerical research

From this climate classification 6 different climate groups are used for the analysis: Am, Aw, BSh, BSk, Cfa and Cfb. Table 3.3 presents additional information about these groups.

Table 3.3: Climate type and characteristics regarding precipitation of the considered climate groups (Wikipedia.org and UWSP.edu).

Climate group	Climate type	Precipitation
Am Cairns	Tropical monsoon climate	Seasonality of precipitation, highest concentrations during summer season
Aw Darwin	Tropical savanna climate	Same as tropical monsoon climate, but shorter wet season and less precipitation
BSh Broome	Steppe climate with average temperature coldest month > 0 °C	Semi arid environment. Transition between really wet and really dry climates
BSk Eucla	Steppe climate with average temperature coldest month < 0 °C	Semi arid environment. Transition between really wet and really dry climates
Cfa Brisbane	Humid subtropical climate	Precipitation evenly distributed throughout the year
Cfb Melbourne	Oceanic climate	Same as humid subtropical climate. Annual precipitation can be larger than in the tropics

3.3.2 Numerical results

For this second type of simulations climate files corresponding to the different climate groups are used as a boundary condition. Since it is shown that 10-minute meteorological data are highly preferred over hourly data (Blocken et al., 2007), much effort has been made to obtain high resolution meteorological data for all climate groups considered. Only for the direct and diffuse solar radiation half-hourly data were used instead of 10-minute data. Unfortunately solar radiation data could only be obtained for three of the six climate groups, but for every main group considered (A, B and C) though. Therefore for the remaining three groups solar radiation data were adopted from the cities from the same main group.

Furthermore in this case the WDR intensity is determined by means of the catch ratio instead of directly obtained from the climate file, since horizontal rainfall intensity is specified in the climate file. Besides this the wind speed specified in the climate file is the reference wind speed at 10 meters height now instead of the local wind speed and therefore the local wind speed is obtained by means of the Sharples equation (Sharples, 1984). This serves as input for the calculation of the convective heat transfer coefficient (equation (3.4)) Finally the total amount of solar radiation

3. Numerical research

on the building facade is derived from the direct and diffuse solar radiation specified in the climate file.

Simulations are performed for two months during summer season for the year 2007. For each climate group the results for the brick with high porosity (BHP) and the brick with low porosity (BLP) are compared. Figure 3.10 presents the results for climate group Am. All other results are included in Appendix F.

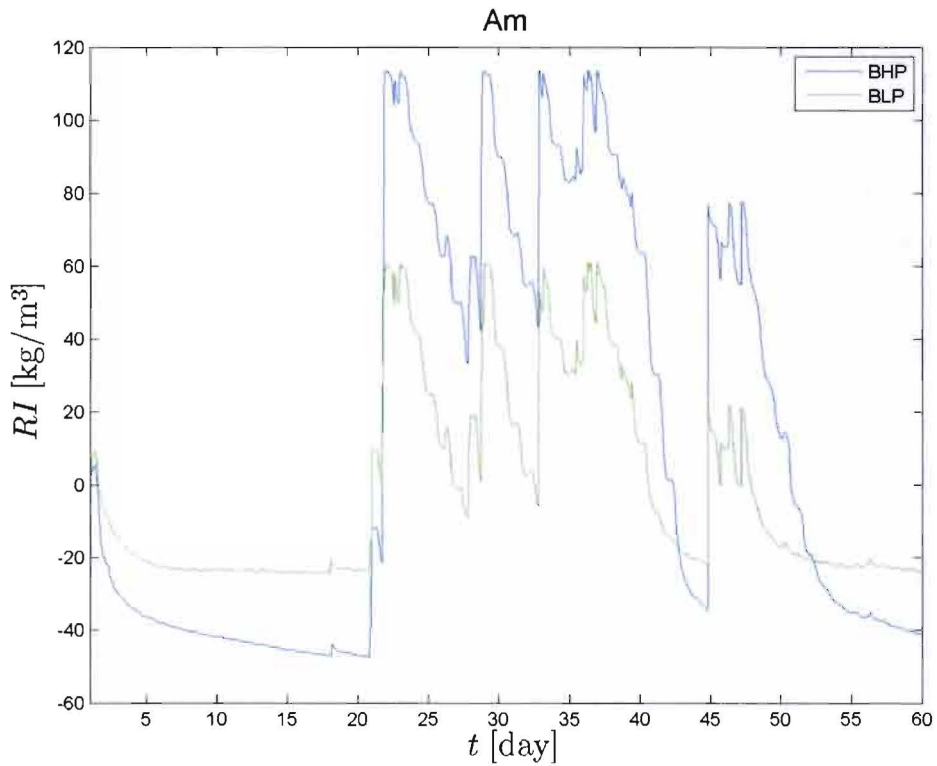


Figure 3.10: Simulation results for climate Group Am.

As can be seen from the figure, a difference in ΔRI by BLP and BHP is observed for several rain events. This implies that runoff occurred for BLP. By checking if the exterior boundary layer of the BHP brick reached the capillary moisture content, it can be verified whether runoff occurred or not for this type of brick. In figure 3.11 the vertical grey lines indicate when runoff occurred for BHP.

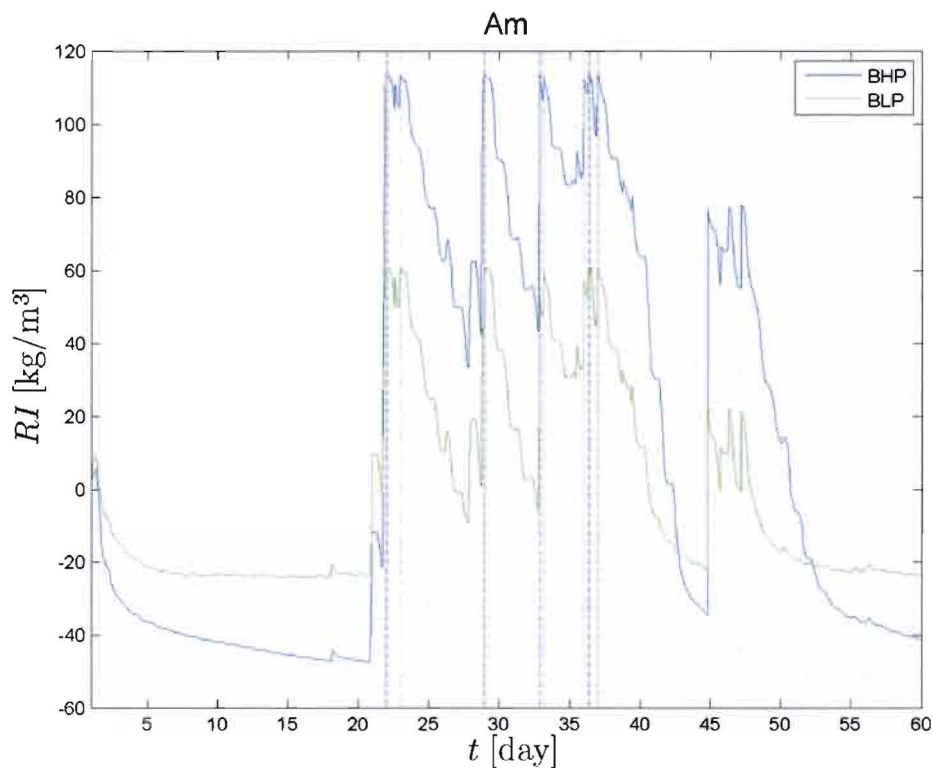


Figure 3.11: Indication of runoff by BHP for climate group Am.

It is verified that the whole brick is capillary saturated at these points in time. Am is the only climate group where this occurs. Furthermore, it is shown that for BHP only runoff occurred for climate group Am and Aw. The fact that runoff occurred for BHP means that RI by this type of brick is then not 100%. The amount of runoff for a certain rain event is obtained by determining the difference between the amount of WDR and RI for that rain event. To gain insight into the different performances regarding RI by both types of brick, the minimum values of RI are determined for all climate groups considered. For climate group BSk no rain events were observed during the considered period. Table 3.4 presents the results.

Table 3.4: Minimum RI by BHP and BLP for all climate groups considered.

	Am	Aw	BSh	Cfa	Cfb
BHP	6.0%	1.9%	100.0%	100.0%	100.0%
BLP	2.4%	0.8%	45.9%	37.4%	95.6%

Table 3.4 shows that for heavy rain events, as were present for all climate groups except for Cfb, the general trend predicted by the simulations is that BLP accommodates for a minimum RI of approximately 40% of RI by BHP. RI for BHP varies between 6% and 100% for climate group Am and between 1.9% and 100% for climate group Aw. The low percentages of RI for climate groups Am and Aw were obtained during periods of severe rain and where the material was not able to dry sufficiently in between rain events to intercept all water of the next rain event.

Note that earlier simulations (section 3.2.2) have shown that in some cases the model fails to accurately predict runoff and the possibility exists that the amount of runoff is underestimated by the model. Therefore no hard conclusions can be drawn on the amount of RI by the two types of brick in other climates.

To gain better insight into the rainfall interception by building materials it is necessary to gain knowledge about all mass flows involved in rainfall interception. It is therefore recommended to obtain simulation results on the amount of WDR and the amount of runoff per time step and from that determine the amount of rainfall interception in time.

3.4 Conclusion

To conclude this chapter some conclusions are drawn. For the high absorptive brick the simulation results have shown the same trend as the experimental results. Especially the increase in RI during the first rain event was predicted accurately. The RI increase during the second rain event was described less precisely however.

For the low absorptive brick the same observations were made as for the high absorptive brick. However in this case the measurements have shown that runoff occurred for this type of brick. Since the maximum value of RI during simulations was almost the same for both types of brick, this means that the model failed to predict runoff.

The mean deviation between the numerical and experimental results was 35% for BHP and 37% for BLP. This is to a large extent due to the substantial deviations in evaporative drying. The numerical results have shown a faster evaporation process than the experimental results. This in turn is mostly due to the uncertainty of the surface transfer coefficients. To obtain more reliable simulation results, further research on this matter is essential. Furthermore hysteresis in the moisture retention curve could be accounted for to obtain better agreement between experimental and numerical results.

The simulation results of the climate parameter analysis have shown that for some rain events in climate groups Am and Aw only small percentages of RI were obtained. This was due to the occurrence of periods of severe rain where there was no opportunity for the materials to dry sufficiently in between rain events. For the other four climate groups RI by BHP was 100%. The comparison of the performance of the two types of brick has shown a minimum RI of approximately 40% by BLP based on RI by BHP.

It is possible that the amount of runoff was underestimated by the model, since it was earlier shown that the model failed to predict runoff by BLP. Therefore no hard conclusions can be drawn on rainfall interception by porous building materials in other climates.

Chapter 4

Conclusions and recommendations

The final chapter of this report presents overall conclusions that can be drawn from this research. In the full-scale measurements of this study four material samples were considered. It was demonstrated that porous-building materials are capable of intercepting more rainwater than non-porous building materials due to their ability to absorb water rather than only store it on their surface, like the non-porous building materials do. Furthermore the amount of rainfall interception by the two porous building materials has been compared. It was shown that during the measurement period the high absorptive brick yielded 100% rainfall interception against a minimum of 76.6% by the other type of brick. Runoff for this type of brick occurred due to local saturation at the exterior boundary.

During the first part of the numerical research a model has been constructed and validated by means of the measurement results of the porous building materials. For this a test case of 12 days was set up in which two major rain events occurred. The simulation results have shown that for the first rain event the rainfall interception was accurately modeled for the high absorptive brick. The measurement results have shown that runoff occurred for the other type of brick. The model has failed to predict this however. For the second rain event differences between measurements and simulations were observed for both types of brick. However, the main deviation between the numerical and experimental results is due to the faster evaporation process predicted by the model. Improvement on this matter could be made by determining more accurate values of the heat transfer and moisture transfer coefficient. In order to do this further research is necessary.

Finally the model has been adapted and meteorological data from several climate groups was used as boundary condition. For four out of the six climate groups considered it was verified that no runoff occurred for the brick with high porosity. Therefore rainfall interception by this brick was 100%. For the other two climate groups this brick accommodated for a minimum of only 1.9% and 6% during periods of severe rain, increasing to 100% for moderate rain events. According to the

4. Conclusions and recommendations

simulations the rainfall interception by the brick with low porosity is at least 40% of the rainfall interception by the other type of brick. Since earlier simulations have shown that sometimes the model fails to predict runoff, no hard conclusions can be drawn on rainfall interception by porous building materials in other climates.

After discussing the achievements of this study a number of recommendations for further research is formulated in this chapter as well. Starting with the experimental part of this study it is desired to perform measurements regarding heat and moisture transfer coefficients. This way, reliable values of these transfer coefficients are obtained and therefore the implementation in the numerical model is more accurate.

Besides this performing full-scale measurements on building roofs as well would provide useful additional knowledge on rainfall interception by buildings. These building surfaces in general receive more rain than building facades and therefore have potential to intercept large quantities of water and significantly contribute to the prevention of flooding.

Concerning the simulations some improvements can be made as well. As mentioned afore more accurate values of the surface transfer coefficients would result in a better agreement between experimental and numerical results. Besides this, hysteresis could be accounted for in order to better predict the drying process of the materials.




Furthermore the moisture retention curve is an important parameter, since it plays a key role in relating several material parameters. For the simulations it is therefore desired to obtain a reliable curve. It is recommended to collect more measurement data in order to more accurately determine this curve.

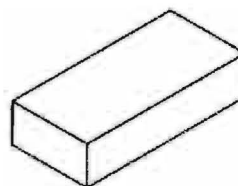
Finally it is recommended that two-dimensional transfer simulations are considered. This way the amount of runoff is predicted and more knowledge is gained on the mass flows involved in rainfall interception. Probably better conclusions on the amount of rainfall interception by porous building materials can then be drawn from the simulation results.

Appendix A

Specifications brick



Brick with High Porosity (BHP)

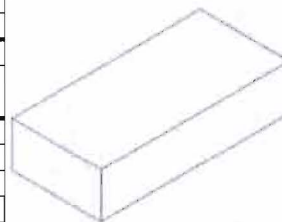
						
Jaar van de markering: 08		Productent: Wienerberger BV				
Certificerende instantie: 0957		Hogeweg 95, NL-5301 LK Zaltbommel				
Certificaat: 0957-CPD-0622		THE NETHERLANDS				
Norm: EN 771-1:2003 + A1:2005		Productie-locatie: Wienerberger Wolfswaard				
		Wolfswaard 2, NL-4043 JE Ophemusden				
		THE NETHERLANDS				
Product: HANDVORM DOMMELROOD WF		Productnummer: 18400				
Groep: HD - Producten		Product-code: 18400A-1125				
Afmetingen en toleranties:		fabrieksmaz	tolerantie	mm	maatspreid	mm
Lengte	mm	209	categorie	± 4	catégorie	9
Breedte	mm	100	T2	± 3	R1	6
Hoogte	mm	50		± 2		4
Volumieke massa:		gemiddelde	categorie		%	
Bruto droge vol. massa	kg/m ³	1800	D1		10	
Netto droge vol. massa	kg/m ³	NPD				
Verschijningsvorm:		Volle asteen				
Metselbaksteengroep	-	1	Volgens EN 1996-1-1 / EN 1996-1-2			
Percentage holle ruimte	%	NPD				
Dikte mantel	mm	NPD				
Dikte ribben	mm	NPD				
Volume grootste van alle perforaties	%	NPD				
Volume van handvaten	%	NPD				
Gecombineerde dikte van ribben en mar	%	NPD				
Gecombineerde dikte van ribben en mar	%	NPD				
Oppervlakte van perforaties op een legv	%	NPD				
Oppervlakte van de handvaten	%	NPD				
Druksterkte:		gemiddelde	genormaliseerd		categorie	
- op het mortelbedvlak	N/mm ²	20	12,5		I	
- op de kop	N/mm ²	NPD	NPD			
Hechtsterkte:		N/mm ²	0,15	Tabelwaarde voor metselsteenmortel volgens EN 998-2, Annex C		
Thermische geleiding:		W/m·K	$\lambda_{eq} = 0,55$	Tabelwaarde volgens EN 1745, Annex A met P=90%		
Dampdoorlatendheid:		-	$\mu = 5/10$	Min- en max. tabelwaarde volgens EN 1745		
Vorst/dooi-weerstand:		categorie	F2	Volgens NEN 2972		
Wateropneming:		%	20			
Initiale wateropzugging		kg/(m ² ·min)	4			
Gehalte actieve oplosbare zouten:		categorie	S2			
Vochtschijf:		mm/m	NPD			
Brandreactie:		klasse	A1	Commissie Besluit 06/603/EC, aangevuld in het Commissie Besluit 2000/605/EC		
Vlakheid:		mm	NPD			
Planparalleliteit:		mm	NPD			
Gevaarlijke stoffen:		-	NLBSB1b			
Aanvullende nationale technische specificaties:						
NLBSB toepassing: landbodem inclusief beschermde gebieden						
						



Druksterkte per perforatieveld kan gering afwijken

Brick with Low porosity (BLP)

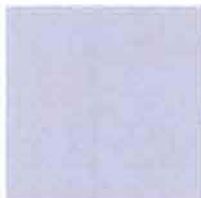
							
Jaar van de markering: 09 Certificerende instantie: 0943 Certificaat: 0943-CPD-1344 Norm: EN 771-1:2003 + A1:2005				Product: RBB-WF voll Groep: HD - Producten			
Productnummer: 34477230 Product-code: 34477230-1344				Product: Wienerberger Ziegelindustrie GmbH D-30659 Hannover, Oldenburger Allee 26 GERMANY Productie-locatie: Werk Knabe Kirchhimmern D-27798 Hude-Kirchlummen, Bremer Straße 9 GERMANY			
Afmetingen en toleranties:		fabrieksmat	tolerantie	mm	maatspreidj	mm	
Lengte	mm	210	categorie	± 6	categorie	9	
Breedte	mm	100	T1	± 4	R1	6	
Hoogte	mm	50		± 3		4	
Volumieke massa:		gemiddelde	categorie		%		
Bruto droge vol. massa		kg/m³	1950	D1	10		
Netto droge vol. massa		kg/m³	NPD				
Verschijningsvorm:		Volle steen					
Metselbaksteengroep	-	2					
Percentage holle ruimte	%	0					
Dikte mantel	mm	NPD					
Dikte ribben	mm	NPD					
Volume grootste van alle perforaties	%	NPD					
Volume van handvaten	%	NPD					
Gecombineerde dikte van ribben en mar	%	NPD					
Gecombineerde dikte van ribben en mar	%	NPD					
Oppervlakte van perforaties op een legv	%	NPD					
Oppervlak van de handvaten	%	NPD					
Druksterkte:		gemiddelde	genormaliseerd	categorie			
- op het mortelbedvlak		N/mm²	25	19	I		
- op de kop		N/mm²	NPD	NPD			
Hechtsterkte:		N/mm²	0,15				
Thermische geleiding:		W/m·K	λ _{eq} = NPD				
Dampdoorlatendheid:		-	s _d = 5/10				
Vorst/dooi-weerstand:		categorie	F2				
Wateropnemng:		%	8				
Initiele wateropzuiging		kg/(m²·min)	1,5				
Gehalte actieve oplosbare zouten:		categorie	S2				
Vochtexpansie:		mm/m	NPD				
Brandreactie:		klasse	A2				
Vlakheid:		mm	NPD				
Planparalleliteit		mm	NPD				
Gevaarlijke stoffen:		-					
Aanvullende nationale technische specificaties:							



Caadestijl: perforatiebeeld van geringe afmeten

Appendix B

Specifications glue



LIJMEN EN AFDICHTINGSMIDDELEN



PU Constructielijm

Product

PU Constructielijm is een gebruiksklare, 1-component constructielijm op basis van polyurethaan. Watervast volgens NEN-EN-204-D4.

Toepassingen

Het watervast verlijmen van alle soorten geschaafd en ongeschaafd hard en zacht hout, houtverbindingen en hout in combinatie met metaal, beton, steen, diverse isolatiematerialen en kunststoffen. Zeer geschikt voor water vaste houtconstructies met ruimere passing.

Eigenschappen

- Vullend (bruist).
- Gebruiksklaar.
- Open tijd 20 minuten.
- Voor binnen en buiten.
- Ook geschikt voor licht vochtig hout.
- KOMO keur 'Lijm voor niet dragende toepassingen'.
- Watervast NEN-EN-204-D4.



Verwerking

Ondergrond: De te verlijmen materialen moeten schoon, droog, stof- en vetvrij zijn. Houtvochtigheid max. 25%.

Voorbehandeling: Vette houtsoorten (teak) vooraf ontvetten en direct verlijmen. Bij erg droge materialen of een geringe luchtvochtigheid de te verlijmen delen licht bevochtigen.

Aanbrengen: De lijm gelijkmatig éénzijdig aanbrengen.

Open tijd: Voeg beide delen binnen 20 minuten samen.

Droogtijd/klemtijd/afbindtijd: Pers (3 kg/cm²) de verbinding gedurende min. 12 uur samen. (perstijd afhankelijk van houtsoort, vochtigheid van het hout en omgevingstemperatuur). Niet verwerken onder +5°C.

Verbruik: 100-200 g/m², afhankelijk van de porositeit van de ondergrond.

Reinigen: reinigen van verse lijm met aceton, opgedroogde lijm enkel mechanisch.



Appendix C

Specifications equipment

Full-scale measurements

Measurement equipment: Horizontal rain gauge

Manufacturer: Young

Type: 52202

ID-number: ID 0479, 0559 and 0560

Collection area: 0.02 m²

Resolution: 0.1 mm per pulse (2 ml)

Measurement equipment: Wind-driven rain gauge

Manufacturer: Laboratory of building physics, Eindhoven University of Technology

ID-number: ID 1363, 1366, 1368 and 1370

Collection area: 0.04 m²

Resolution: 0.015 mm per pulse (0.6 ml)

Measurement equipment: Pyranometer

Manufacturer: Kipp

Type: CM 11

ID-number: ID 0689

Sensitivity: 4.37 $\mu\text{V}/\text{Wm}^2$

Laboratory experiments

Eindhoven:

Measurement equipment: Balance

Manufacturer: Mettler Toledo

Type: PR5002

ID-number: 1808

Serial number: 1113143437

Date of calibration: 18-05-2009

The balance has an automatic calibration system

Measurement equipment: T and RH logger

Manufacturer: Escort

ID-number: 487

Serial number: 0346-010

Escort reader and software

ID-number: 1728

Leuven:

Measurement equipment: Balance

Manufacturer: Mettler Toledo

Type: XS10035

Serial number: 1125481872

Measurement equipment: Mercury porosimeter

Manufacturer: Micromeritics

Type: AutoPore IV

Measurement equipment: Pressure plate extractor

Manufacturer: Soilmoisture

Type: 1500 F1 15 bar pressure plate extractor

Appendix D

Results water absorption experiment

Figure D.1 until D.6 show the water absorption in time for the different test bricks of BHP.

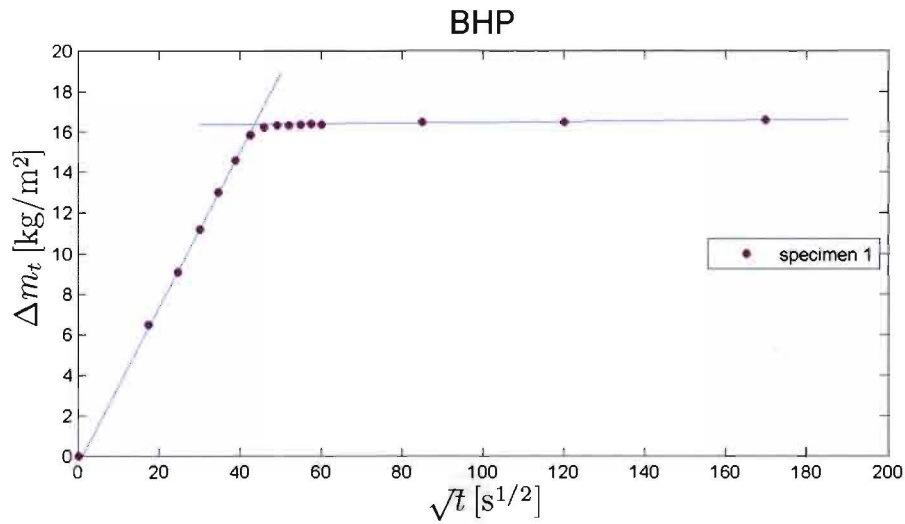


Figure D.1: Water absorption in time for brick 1 of BHP.

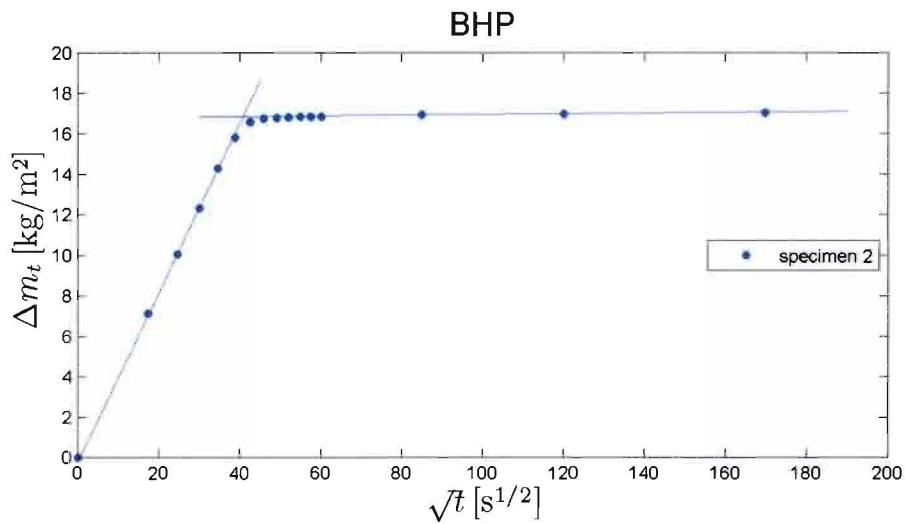


Figure D.2: Water absorption in time for brick 2 of BHP.

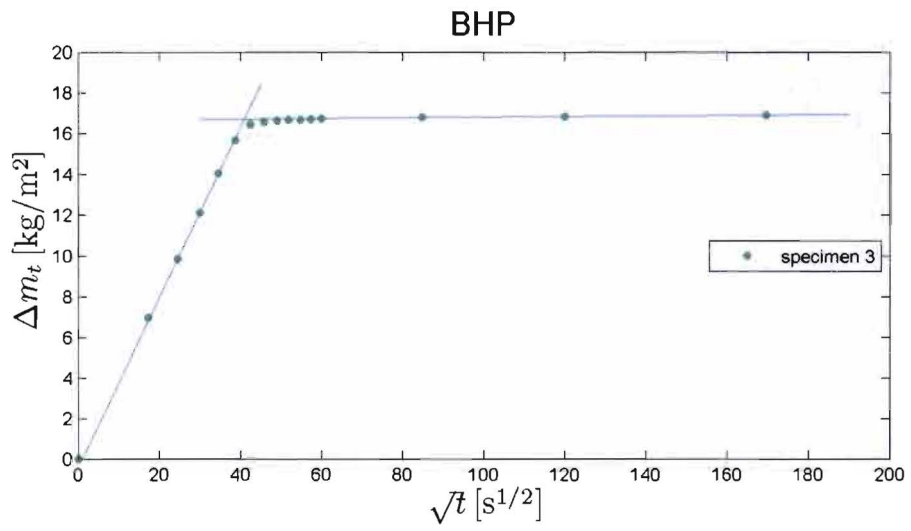


Figure D.3: Water absorption in time for brick 3 of BHP.

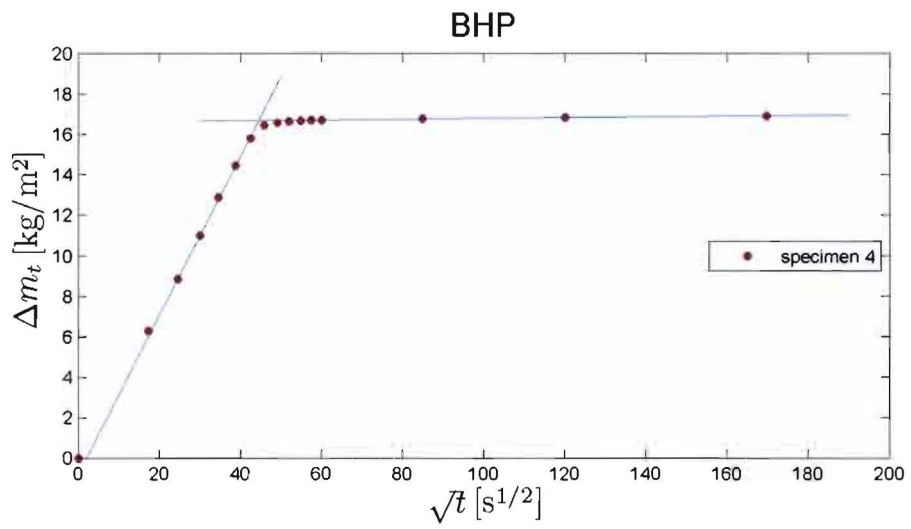


Figure D.4: Water absorption in time for brick 4 of BHP.

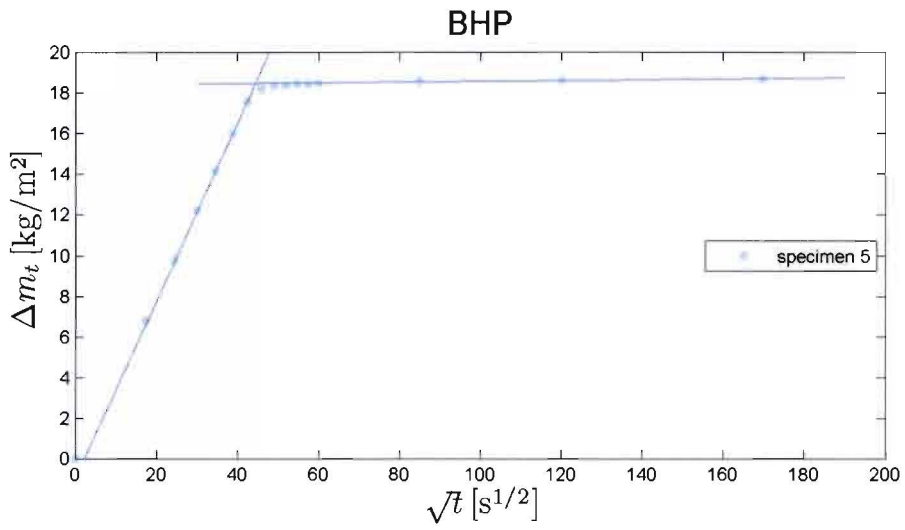


Figure D.5: Water absorption in time for brick 5 of type BHP.

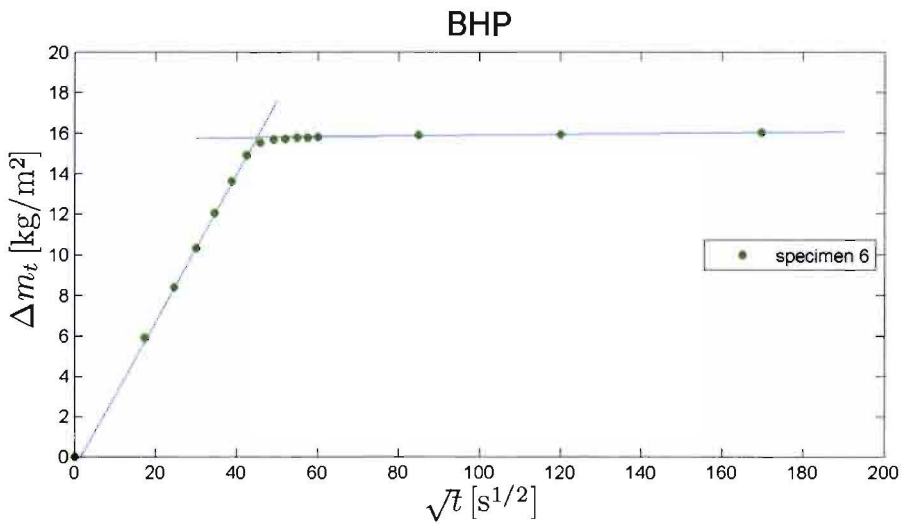


Figure D.6: Water absorption in time for brick 6 of type BHP.

Figure D.7 until D.12 show the water absorption in time for the different test bricks of BLP.

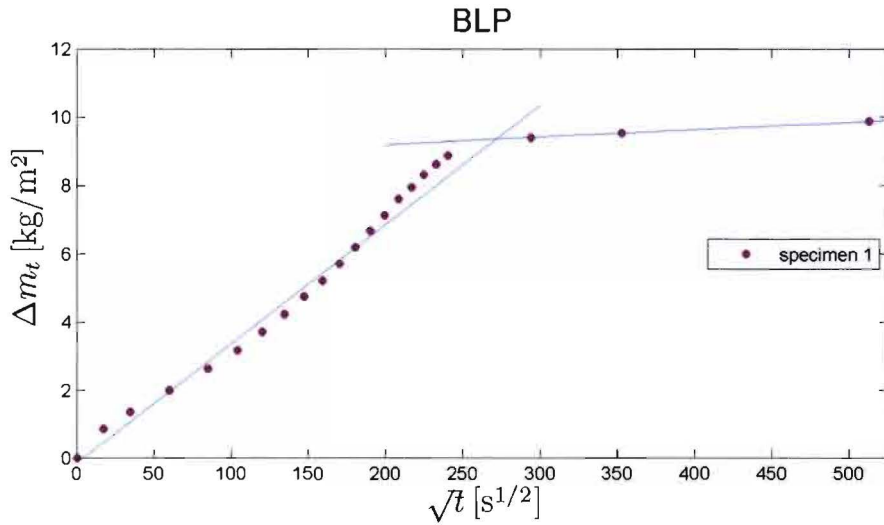


Figure D.7: Water absorption in time for brick 1 of BLP.

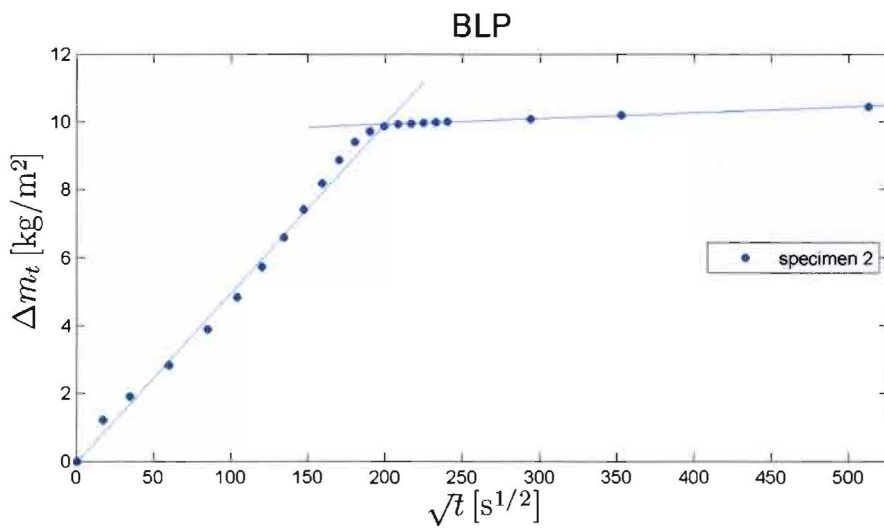


Figure D.8: Water absorption in time for brick 2 of BLP.

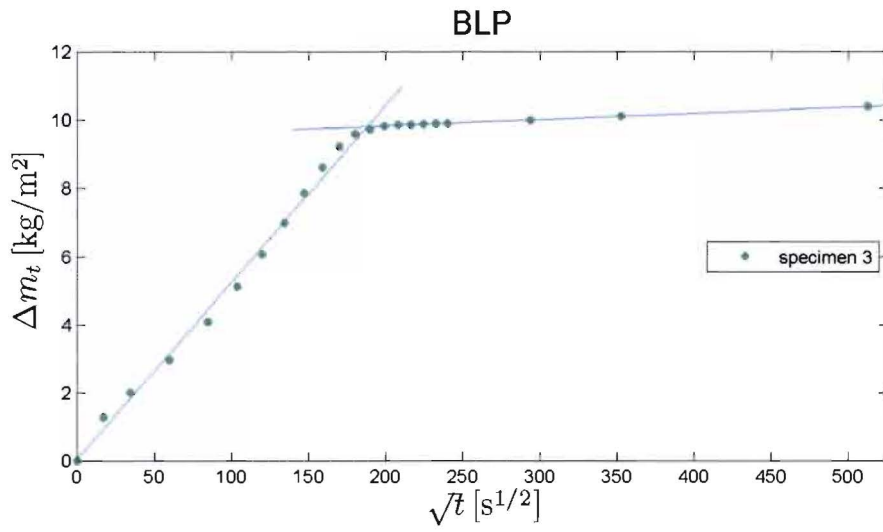


Figure D.9: Water absorption in time for brick 3 of BLP.

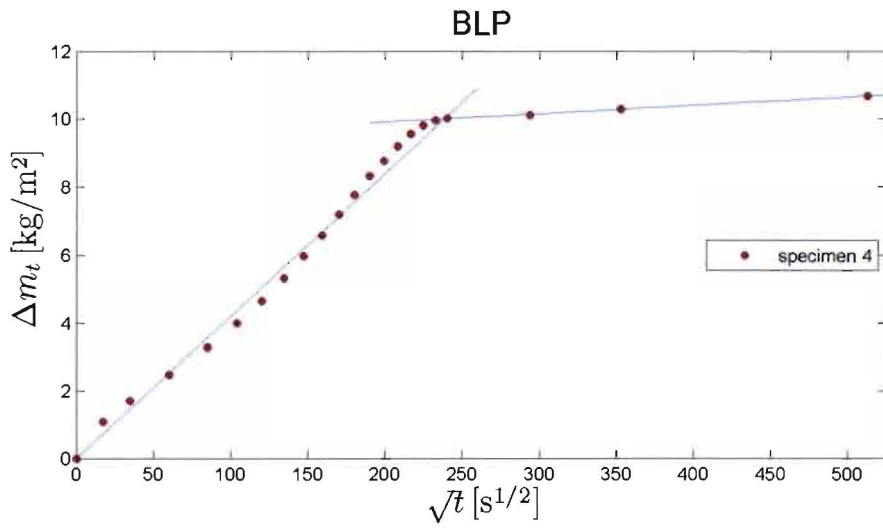


Figure D.10: Water absorption in time for brick 4 of BLP.

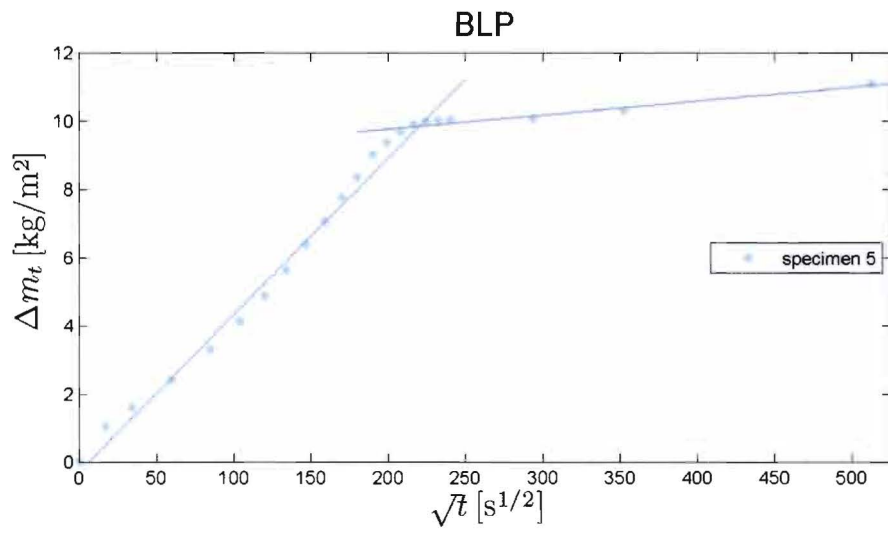


Figure D.11: Water absorption in time for brick 5 of BLP.

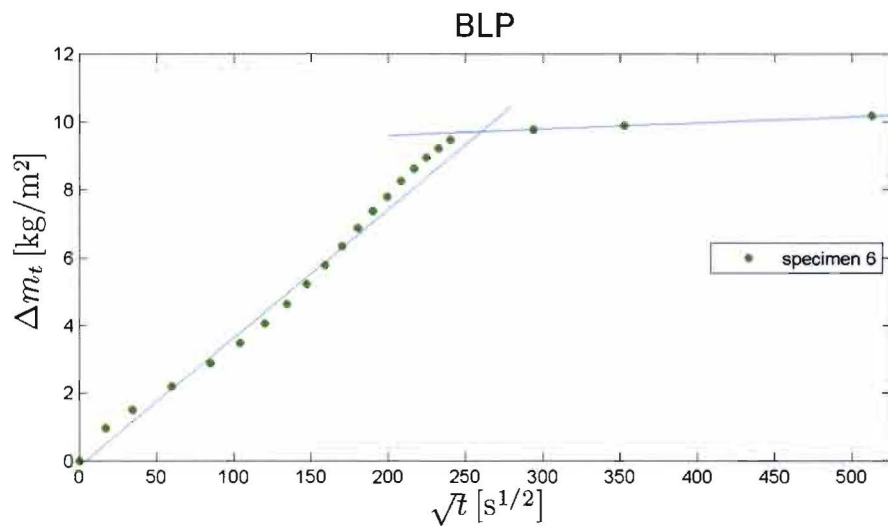


Figure D.12: Water absorption in time for brick 6 of BLP.

Appendix E

Simulation settings

Model validation

General parameters

Orientation: 270°

Initial $p_c = 3.16 \cdot 10^5$ Pa (BHP)

Initial $p_c = 3.16 \cdot 10^6$ Pa (BLP)

Initial T = 274.7 K

51 nodes

Nodal coordinates

0.00E+00

5.00E-04

1.03E-03

1.58E-03

2.16E-03

2.76E-03

3.40E-03

4.07E-03

4.77E-03

5.51E-03

6.29E-03

7.10E-03

7.96E-03

8.86E-03

9.80E-03

1.08E-02

1.18E-02

1.29E-02

1.41E-02

1.53E-02

1.65E-02

1.79E-02

1.93E-02

2.07E-02

2.23E-02

2.39E-02

2.56E-02

2.73E-02

2.92E-02

3.12E-02

3.32E-02

3.54E-02
3.77E-02
4.00E-02
4.25E-02
4.52E-02
4.79E-02
5.08E-02
5.39E-02
5.71E-02
6.04E-02
6.39E-02
6.76E-02
7.15E-02
7.56E-02
7.99E-02
8.43E-02
8.80E-02
9.20E-02
9.60E-02
1.00E-01

Boundary conditions

R_{WDR} obtained from measurements

$$h = 1.7V_{loc} + 5.1$$

V_{loc} directly obtained from measurements

$$\beta = 7.7 \cdot 10^9 \text{ h}$$

Short wave radiation directly obtained from measurements

Climate parameter analysis

General parameters

Initial $p_c = 3.16 \cdot 10^5$ Pa (BHP)

Initial $p_c = 1.36 \cdot 10^5$ Pa (BLP)

Initial $T = 274.7$ K

Boundary conditions

$$R_{WDR} = \frac{\eta}{R_h}$$

$$h = 1.7V_{loc} + 5.1$$

$$V_{loc} = 1.8w_s + 0.2 \text{ (windward surface)}$$

$$V_{loc} = 0.5w_s + 1.7 \text{ (leeward surface)}$$

$$\beta = 7.7 \cdot 10^9 \text{ h}$$

Short wave radiation derived from direct and diffuse solar radiation in climate file.

Appendix F

Simulation results climate groups

Figure F.1 to F.5 present the simulation results for the different climate groups. For climate group BSk no rain events were observed during the considered period.

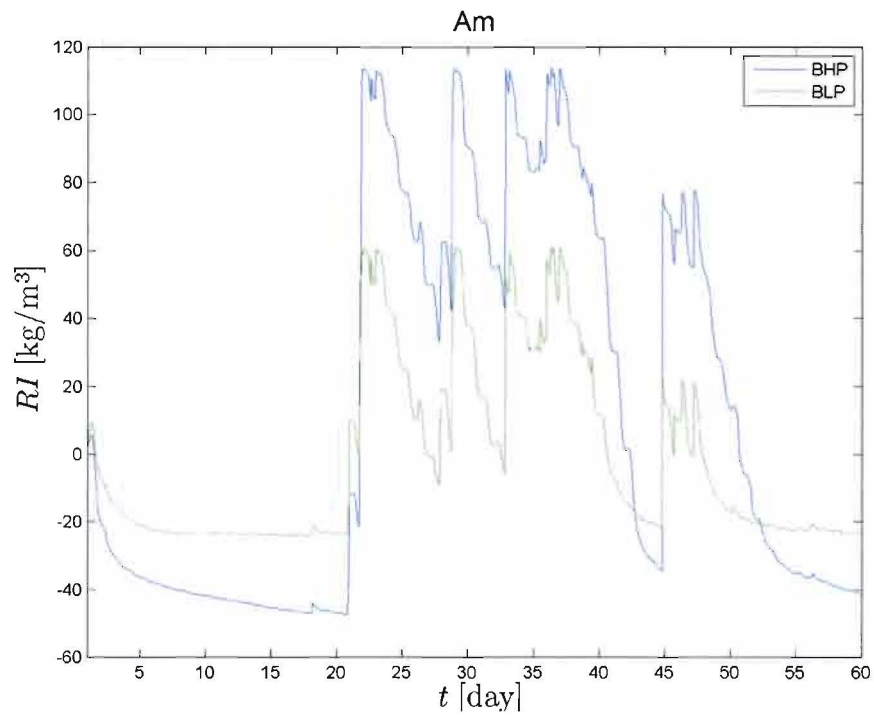


Figure F.1: Simulation results for climate Group Am.

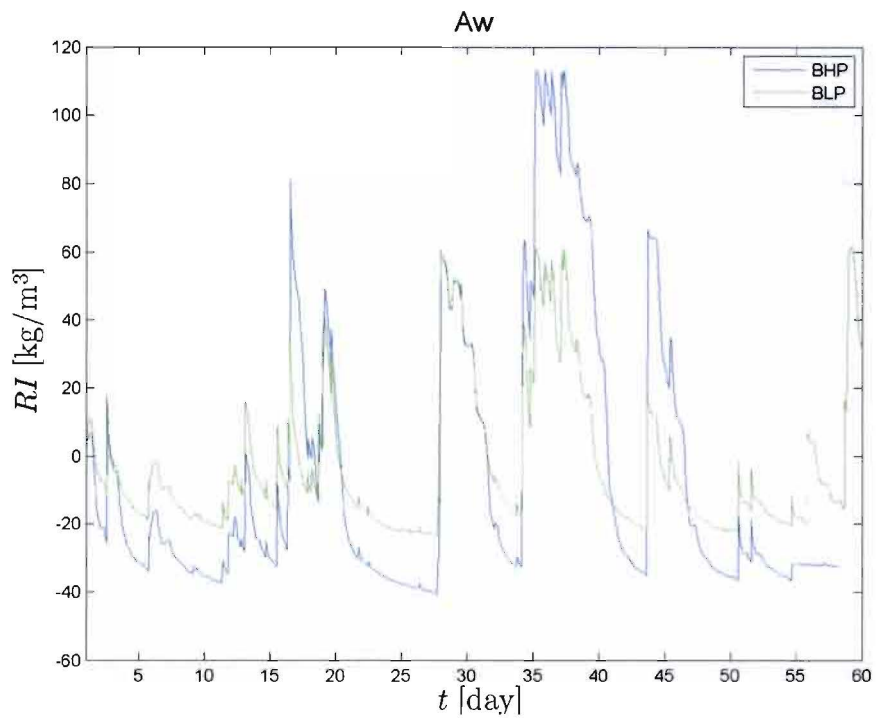


Figure F.2: Simulation results for climate Group Aw.

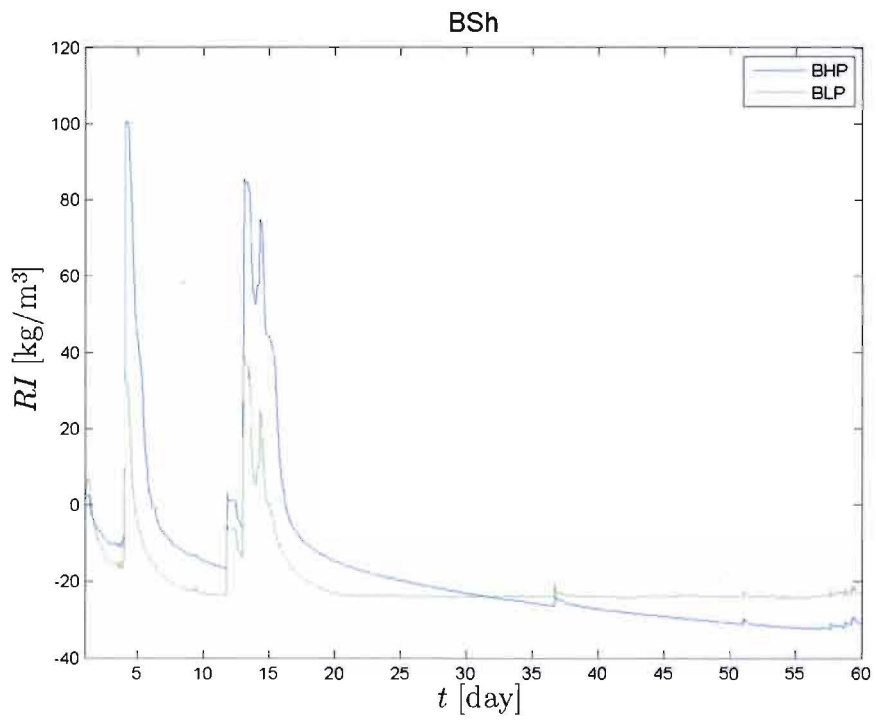


Figure F.3: Simulation results for climate Group BSh.

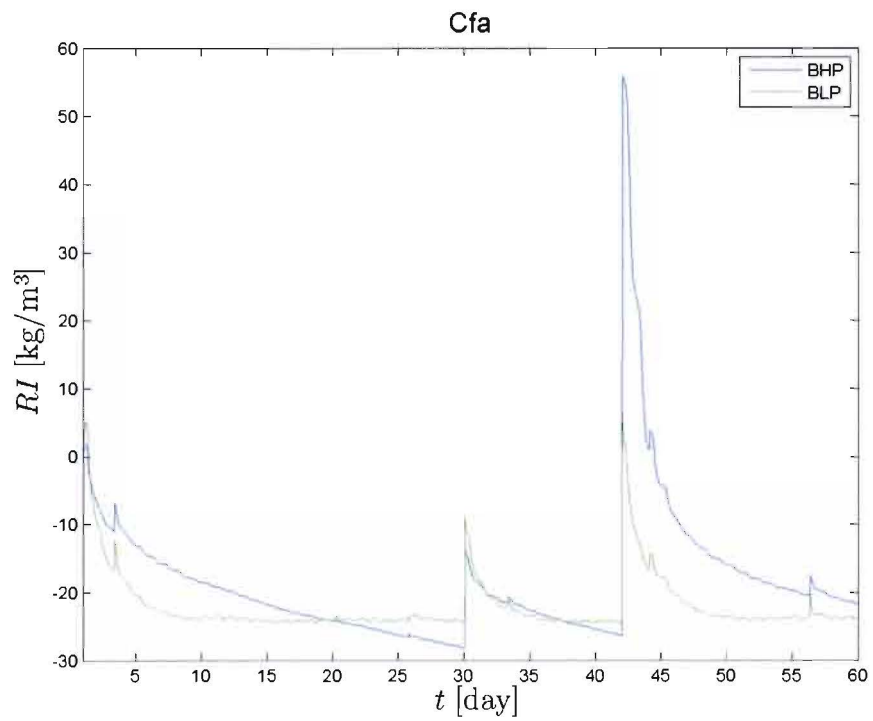


Figure F.4: Simulation results for climate Group Cfa.

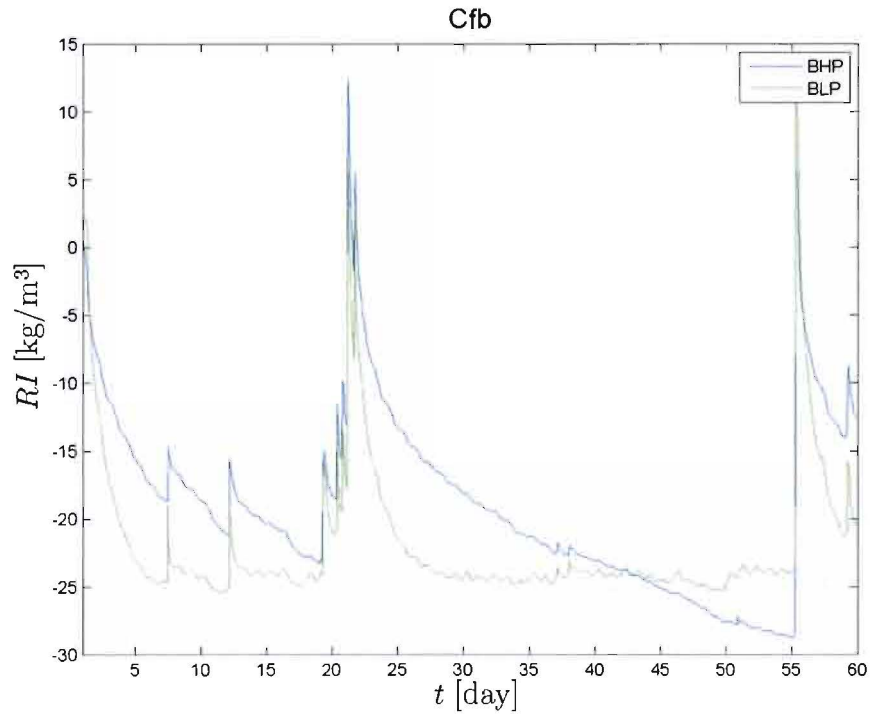


Figure F.5: Simulation results for climate Group Cfb.

References

Abuku, M., Blocken, B. and Roels, S. (2009). Moisture response of building facades to wind-driven rain: Field measurements compared with numerical simulations. *Journal of Wind Engineering and Industrial Aerodynamics*, 97, 197-207.

Bear, J. and Bachmat, Y. (1990). Introduction to modeling of transport phenomena in porous media. *Kluwer Academic Publishers, Dordrecht*.

Blocken, B. and Carmeliet, J. (2002). Spatial and temporal distribution of driving rain on a low-rise building. *Wind and Structures*, 5, 441-462.

Blocken, B. and Carmeliet, J. (2004). A review on wind-driven rain research in building science. *Journal of Wind Engineering and Industrial Aerodynamics*, 92, 1079-1130.

Blocken, B. and Carmeliet, J. (2006). On the accuracy of wind-driven rain measurements on buildings. *Building and Environment*, 41, 1798-1810.

Blocken, B., Roels, S. and Carmeliet, J. (2007). A combined CFD-HAM approach for wind-driven rain on building facades. *Journal of Wind Engineering and Industrial Aerodynamics*, 95, 585-607.

Blocken, B., Derome, D. and Carmeliet, J. (2009). Overview of research on rainwater runoff from building facades. *12th Canadian Conference on Building Science and Technology. Montreal, Quebec*.

Bouten, K. (2010). De slagregenmeter – Het schrijven van een kalibratieprocedure en onderzoek verrichten naar verbeterpunten van de slagregenmeter TUE-III. *Eindhoven University of Technology*.

Briggen, P., Blocken, B. and Schellen, H. (2009). Wind-driven rain on the facade of a monumental tower: Numerical simulation, full-scale validation and sensitivity analysis. *Building and Environment*, 44(8), 1675-1690.

Carmeliet, J., Hens, H. and Roels, S. (2004). Determination of the liquid water diffusivity from transient moisture transfer experiments. *Journal of Thermal Envelope and Building Science*, vol 27, no 4.

Crank, J. (1989). The mathematics of diffusion. *Oxford University Press, Oxford, United Kingdom*.

IPCC fourth assessment report (2007). Climate change 2007.

- Janssen, H., Blocken, B. and Carmeliet, J. (2007a). Conservative modeling of the moisture and heat transfer in building components under atmospheric excitation. *International Journal of Heat and Mass Transfer*, 50, 1128-1140.
- Janssen, H., Blocken, B., Roels, S. and Carmeliet, J. (2007b). Wind-driven rain as a boundary condition for HAM simulations: Analysis of simplified modelling approaches. *Building and Environment*, 42, 1555-1567.
- Hens, H. (2003). Toegepaste Bouwfysica 1, Randvoorwaarden, Prestatie, Materiaal-eigenschappen. *Uitgeverij ACCO*, ISBN
- Van Mook, J.R. (2002). Driving rain on building envelopes. *PhD thesis, Eindhoven University of Technology*.
- Nakayoshi, M., Moriwaki, S., Kawai, T. and Kanda, M. (2009). Experimental study on rainfall interception over an outdoor urban scale model. *Water Resources Research*, 45.
- Pel, L. (1995). Moisture transport in porous building materials. *PhD thesis, Eindhoven University of Technology*.
- Ragab, R., Bromley, J., Rosier, P., Cooper, D. and Gash, J. (2003). Experimental study of water fluxes in a residential area: 1. Rainfall, roof runoff and evaporation: the effect of slope and aspect. *Hydrological Processes*, 17, 2409-2422.
- Roels, S. (2000). Modeling unsaturated moisture transport in heterogeneous limestone. *PhD thesis, Katholic University Leuven*.
- Roels, S., Carmeliet, J. and Hens, H. (2003). HAMSTAD, WP1: Final report moisture transfer properties and materials characterization, HAMSTAD document KUL2003-h18, *K.U. Leuven, Belgium*.
- Roels, S. and Carmeliet, J. (2006). Analysis of moisture flow in porous materials using microfocus X-ray radiography. *International Journal of Heat and Mass Transfer*, vol 49, 4762-4772.
- Sharples, S. (1984). Full-scale measurements of convective energy losses from exterior building surfaces. *Building and Environment*, vol 19, no 1, 31-39.
- Standard NEN-EN-ISO 15148 (2002). Hygrothermal performance of building materials and products – Determination of water absorption coefficient by partial immersion.
- Strahler, N. and Strahler, H. (1984). Physical geography. *John Wiley and sons, New York*.
- Tanford, C. (1979). Interfacial free energy and the hydrophobic effect. *Proceedings of the National Academy of Sciences of the United States of America*, vol 76, 4175-4176.

Van Genuchten, M.T. (1980). A closed-form equation for predicting the hydraulic conductivity of unsaturated soils. *Soil Science Society of America Journal.*, vol 44, 892-898.

Knoll, G.F. (1989). Radiation detection and measurement. *John Wiley and sons, New York.*

Webpages

<http://maps.google.nl/maps>
(October 2009)

www.wikipedia.org
(April 2010)

www.uwsp.edu/geo/faculty/ritter/geog101/textbook/title_page.html
(April 2010)

www.tue.nl
(April 2010)

www.knmi.nl
(May 2010)

www.weathershack.com
(May 2010)

www.ramehart.com
(May 2010)

www.waterkaderhaaglanden.nl
(May 2010)